

1-30-2013

A moment-preserving single-event Monte Carlo model of electron and positron energy-loss straggling

Matthew Gonzales

Follow this and additional works at: https://digitalrepository.unm.edu/ne_etds

Recommended Citation

Gonzales, Matthew. "A moment-preserving single-event Monte Carlo model of electron and positron energy-loss straggling." (2013). https://digitalrepository.unm.edu/ne_etds/26

This Thesis is brought to you for free and open access by the Engineering ETDs at UNM Digital Repository. It has been accepted for inclusion in Nuclear Engineering ETDs by an authorized administrator of UNM Digital Repository. For more information, please contact disc@unm.edu.

Matthew Alejandro Gonzales

Candidate

Chemical & Nuclear Engineering

Department

This thesis is approved, and it is acceptable in quality and form for publication:

Approved by the Thesis Committee:

Dr. Anil K. Prinja

, Chairperson

Dr. Forrest Brown

Dr. Gary Cooper

Dr. Grady Hughes

A Moment-Preserving Single-Event Monte Carlo Model of Electron and Positron Energy-Loss Straggling

by

Matthew Alejandro Gonzales

B.S., Mathematics, Regis University, 2009

THESIS

Submitted in Partial Fulfillment of the
Requirements for the Degree of

Master of Science
Nuclear Engineering

The University of New Mexico

Albuquerque, New Mexico

December, 2012

©2012, Matthew Alejandro Gonzales

Dedication

To my mother and father. If it were not for your support, guidance and example I would not have had the opportunities for success that I have been blessed to achieve.

Acknowledgments

First and foremost, I would like to thank God for the gifts and guidance He has given; all things are possible through Him who strengthens me. I would like to thank Dr. Anil Prinja, my advisor, for his support, patience and guidance through this work as well as Grady Hughes for his insights and suggestions.

A Moment-Preserving Single-Event Monte Carlo Model of Electron and Positron Energy-Loss Straggling

by

Matthew Alejandro Gonzales

B.S., Mathematics, Regis University, 2009

M.S., Nuclear Engineering, University of New Mexico, 2012

Abstract

Analog simulation of energy straggling of electrons and positrons is computationally impractical because of long-range Coulomb forces resulting in highly peaked cross sections about small energy-losses and extremely small collision mean free paths. The resulting transport process is dominated by very frequent small energy transfer collisions but a significant contribution to the overall energy-loss distribution comes from the infrequent high energy-losses. Sufficient resolution in energy-loss spectra and dose profiles using single-event Monte Carlo methods would then require a large number of particle samples. In this thesis, we demonstrate that a pseudo-differential cross section designed to approximately yet accurately preserve energy-loss moments is capable of yielding accurate energy-loss spectra and dose distributions in a single-event Monte Carlo formulation.

A benchmark solution for the analog problem for incident electrons and positrons is developed in order to provide an exact solution in which our approximation is

evaluated against. A “random walk” sequence is used to randomly sample a distance to collision followed by a sampled energy-loss at the distance traveled by the particle. This process was completed until specific boundaries or cutoffs were met. Due to the non-linearity of the probability distribution functions for the electron and positron energy-loss differential cross sections, analog energy-loss sampling is simulated using the rejection method.

The Landau straggling distribution is examined in detail and its accuracy is quantitatively assessed. Under the constraints in the formulation of Landau, we show that the number of energy-loss moments preserved is equal to the number of energy-flux moments preserved. More specifically, when the energy-losses within a given distance are sufficiently small so that the mean free path can be considered constant, the number of energy-loss moments preserved up to order N is equal to the number of energy-flux moments preserved up to order N . Energy-flux moments of Landau and the analog solution are compared. This moment-preserving theory provides the foundation in which a pseudo-transport model based on the Landau energy-loss distribution is then constructed.

Next, the Landau distribution is used in formulating a pseudo-transport model. The energy-dependent mean free paths of this model is exponentially sampled while the energy-loss will be sampled using the Landau energy-loss distribution in terms of the respective mean free path, incident energy and mean energy-loss of the particle. The Landau Pseudo-Transport(LPT) model allows longer mean free paths and smoother distributions increasing the efficiency of electron and positron transport.

Extensive numerical comparisons of the LPT model against the benchmark are conducted for energy-loss spectra and depth-dose profiles. It is shown that while high fidelity dose distributions can be obtained at a fraction of the cost of the analog calculation, energy spectra are difficult to resolve because of the presence of artifacts associated with the Landau distribution itself. Although these artifacts are reduced

in thicker materials, a loss of computational efficiency results in step-sizes that are relatively close to the analog mean free path when attempting to resolve these deficiencies. The step-size of the simulations must be chosen to balance the greatest efficiency with the highest accuracy. In summation, a pseudo-transport model with longer mean free paths and smoother cross sections has been developed to increase computational time producing results comparable to the analog solution.

Contents

List of Figures	xii
List of Tables	xvii
1 Introduction	1
2 Analog Problem	5
2.1 Ionization of Matter by Charged Particles	5
2.2 Energy-Loss Cross Sections	7
2.3 Analog Transport Problem	12
2.4 Energy-Loss and Flux-Energy Moments	14
2.4.1 Energy-Loss Moments of the Differential Cross Section	14
2.4.2 Energy-Flux Moments	18
3 Monte Carlo Solution of the Analog Problem	19
3.1 Random Walk	20

Contents

3.2	Distance to Collision	21
3.3	Energy-Loss	22
3.3.1	Rejection Method Solution	23
3.4	Statistical Evaluation of Monte Carlo	24
3.4.1	Energy-Loss Spectra	25
3.4.2	Energy Deposition	26
3.5	Benchmark Solutions	27
3.5.1	Gold	28
3.5.2	Water	33
4	Landau Theory	37
4.1	Derivation	38
5	Implementation of the Landau Straggling Distribution	46
5.1	Electron Steps and Substeps	47
5.2	Continuous Slowing Down Approximation for Landau	47
5.3	Numerical Evaluation of the Landau Energy-Loss Distribution	49
5.3.1	MCNP5 Computational Sampling of Landau	50
5.4	Benchmark Comparison	52
6	Lewis-type Theory for Moment-Preserving Energy Straggling	67
6.1	Landau Energy-Flux Moments	72

Contents

7	Landau Pseudo-Transport(LPT) Model	80
7.0.1	Distance to Collision	82
7.0.2	Energy-Loss	82
7.1	Energy-Loss Spectra	83
7.2	Energy Deposition	91
8	Results and Comparisons to the Benchmark	97
8.1	Energy-Loss Spectra	98
8.2	Dose	105
9	Conclusion	110
	References	114

List of Figures

2.1	Rutherford Differential Cross Section for Electrons on Gold	9
2.2	Ratio of Möller to Rutherford Differential Cross Sections for Electrons on Gold	10
2.3	Ratio of Bhabha to Rutherford Differential Cross Sections for Electrons on Gold	11
2.4	First 6 Energy-Loss Moments, Electrons on Gold	16
2.5	First 6 Energy-Loss Moments, Positrons on Gold	16
2.6	First 6 Energy-Loss Moments, Electrons on Water	17
2.7	First 6 Energy-Loss Moments, Positrons on Water	17
3.1	Energy-Loss Spectra of 1 <i>MeV</i> Electrons on $8.515 \times 10^{-3}cm$ of Gold	28
3.2	Energy-Loss Spectra of 1 <i>MeV</i> Positrons on $8.515 \times 10^{-3}cm$ of Gold	29
3.3	Energy Deposition of 1 <i>MeV</i> Electrons on $2.0 \times 10^{-1}cm$ of Gold . .	29
3.4	Energy Deposition of 1 <i>MeV</i> Positrons on $2.0 \times 10^{-1}cm$ of Gold . .	30
3.5	Energy-Loss Spectra of 10 <i>MeV</i> Electrons on $7.47 \times 10^{-2}cm$ of Gold	31
3.6	Energy-Loss Spectra of 10 <i>MeV</i> Positrons on $7.47 \times 10^{-2}cm$ of Gold	31

List of Figures

3.7	Energy Deposition of 10 <i>MeV</i> Electrons on 1.7 <i>cm</i> of Gold	32
3.8	Energy Deposition of 10 <i>MeV</i> Positrons on 1.7 <i>cm</i> of Gold	32
3.9	Energy-Loss Spectra of 1 <i>MeV</i> Electrons on 9.633×10^{-2} <i>cm</i> of Water	33
3.10	Energy-Loss Spectra of 1 <i>MeV</i> Positrons on 9.633×10^{-2} <i>cm</i> of Water	33
3.11	Energy Deposition of 1 <i>MeV</i> Electrons on 1.6 <i>cm</i> of Water	34
3.12	Energy Deposition of 1 <i>MeV</i> Poitrons on 1.8 <i>cm</i> of Water	34
3.13	Energy-Loss Spectra of 10 <i>MeV</i> Electrons on 1.131 <i>cm</i> of Water . . .	35
3.14	Energy-Loss Spectra of 10 <i>MeV</i> Poitrons on 1.131 <i>cm</i> of Water . . .	35
3.15	Energy Deposition of 10 <i>MeV</i> Electrons on 18 <i>cm</i> of Water	36
3.16	Energy Deposition of 10 <i>MeV</i> Positrons on 18 <i>cm</i> of Water	36
5.1	Energy-Loss Spectra of 200 <i>keV</i> Electrons on 1.16×10^{-3} <i>cm</i> of Gold	55
5.2	Energy-Loss Spectra of 200 <i>keV</i> Electrons on 1.25×10^{-2} <i>cm</i> of Water	55
5.3	Energy-Loss Spectra of 500 <i>keV</i> Electrons on 3.90×10^{-3} <i>cm</i> of Gold	56
5.4	Energy-Loss Spectra of 500 <i>keV</i> Electrons on 5.07×10^{-2} <i>cm</i> of Water	56
5.5	Energy-Loss Spectra of 1 <i>MeV</i> Electrons on 8.52×10^{-3} <i>cm</i> of Gold	57
5.6	Energy-Loss Spectra of 1 <i>MeV</i> Electrons on 9.63×10^{-2} <i>cm</i> of Water	57
5.7	Energy-Loss Spectra of 5 <i>MeV</i> Electrons on 3.99×10^{-2} <i>cm</i> of Gold	58
5.8	Energy-Loss Spectra of 5 <i>MeV</i> Electrons on 4.47×10^{-1} <i>cm</i> of Water	58
5.9	Energy-Loss Spectra of 10 <i>MeV</i> Electrons on 7.47×10^{-2} <i>cm</i> of Gold	59
5.10	Energy-Loss Spectra of 10 <i>MeV</i> Electrons on 8.84×10^{-1} <i>cm</i> of Water	59

List of Figures

5.11	Energy-Loss Spectra of 20 <i>MeV</i> Electrons on $1.40 \times 10^{-1}cm$ of Gold	60
5.12	Energy-Loss Spectra of 20 <i>MeV</i> Electrons on 1.67 <i>cm</i> of Water . . .	60
5.13	Energy-Loss Spectra of 200 <i>keV</i> Positrons on $1.16 \times 10^{-3}cm$ of Gold	61
5.14	Energy-Loss Spectra of 200 <i>keV</i> Positrons on $1.25 \times 10^{-2}cm$ of Water	61
5.15	Energy-Loss Spectra of 500 <i>keV</i> Positrons on $3.90 \times 10^{-3}cm$ of Gold	62
5.16	Energy-Loss Spectra of 500 <i>keV</i> Positrons on $5.07 \times 10^{-2}cm$ of Water	62
5.17	Energy-Loss Spectra of 1 <i>MeV</i> Positrons on $8.52 \times 10^{-3}cm$ of Gold	63
5.18	Energy-Loss Spectra of 1 <i>MeV</i> Positrons on $9.63 \times 10^{-2}cm$ of Water	63
5.19	Energy-Loss Spectra of 5 <i>MeV</i> Positrons on $3.99 \times 10^{-2}cm$ of Gold	64
5.20	Energy-Loss Spectra of 5 <i>MeV</i> Positrons on $4.47 \times 10^{-1}cm$ of Water	64
5.21	Energy-Loss Spectra of 10 <i>MeV</i> Positrons on $7.47 \times 10^{-2}cm$ of Gold	65
5.22	Energy-Loss Spectra of 10 <i>MeV</i> Positrons on $8.84 \times 10^{-1}cm$ of Water	65
5.23	Energy-Loss Spectra of 20 <i>MeV</i> Positrons on $1.40 \times 10^{-1}cm$ of Gold	66
5.24	Energy-Loss Spectra of 20 <i>MeV</i> Positrons on 1.67 <i>cm</i> of Water . . .	66
7.1	Energy-Loss Spectra of 1 <i>MeV</i> Electrons on $9.6 \times 10^{-2}cm$ of Water	88
7.2	Relative Error of 1 <i>MeV</i> Electrons on $9.6 \times 10^{-2}cm$ of Water	88
7.3	Energy-Loss Spectra of 10 <i>MeV</i> Electrons on 1.31 <i>cm</i> of Water . . .	89
7.4	Energy-Loss Spectra of 10 <i>MeV</i> Electrons on $7.5 \times 10^{-2}cm$ of Gold	89
7.5	Energy-Loss Spectra of 1 <i>MeV</i> Positrons on $9.6 \times 10^{-2}cm$ of Water	90
7.6	Energy-Loss Spectra of 1 <i>MeV</i> Positrons on $8.52 \times 10^{-3}cm$ of Gold	90

List of Figures

7.7	Energy Deposition of 1 <i>MeV</i> Electrons on 2.5 <i>cm</i> of Water	93
7.8	Relative Error of 1 <i>MeV</i> Electrons on 2.5 <i>cm</i> of Water	93
7.9	Energy Deposition of 1 <i>MeV</i> Electrons on 0.2 <i>cm</i> of Gold	94
7.10	Relative Error of 1 <i>MeV</i> Electrons on 0.2 <i>cm</i> of Gold	94
7.11	Energy Deposition of 10 <i>MeV</i> Electrons on 18 <i>cm</i> of Water	95
7.12	Energy Deposition of 10 <i>MeV</i> Electrons through 18 <i>cm</i> of Water . . .	95
7.13	Energy Deposition of 10 <i>MeV</i> Electrons on 1.7 <i>cm</i> of Gold	96
7.14	Energy-loss of 10 <i>MeV</i> Electrons through 1.7 <i>cm</i> of Gold	96
8.1	Energy-loss Spectra of 1 <i>MeV</i> Electrons on 9.6×10^{-2} <i>cm</i> of Water .	101
8.2	Energy-loss Spectra of 1 <i>MeV</i> Positrons on 9.6×10^{-2} <i>cm</i> of Water .	101
8.3	Energy-loss Spectra of 1 <i>MeV</i> Electrons on 8.52×10^{-3} <i>cm</i> of Gold .	102
8.4	Energy-loss Spectra of 1 <i>MeV</i> Positrons on 8.52×10^{-3} <i>cm</i> of Gold .	102
8.5	Energy-loss Spectra of 10 <i>MeV</i> Electrons on 1.31 <i>cm</i> of Water	103
8.6	Energy-loss of 10 <i>MeV</i> Positrons on 1.31 <i>cm</i> of Water	103
8.7	Energy-loss Spectra of 10 <i>MeV</i> Electrons on 7.5×10^{-2} <i>cm</i> of Gold .	104
8.8	Energy-loss Spectra of 10 <i>MeV</i> Positrons on 7.5×10^{-2} <i>cm</i> of Gold .	104
8.9	Energy Deposition of 1 <i>MeV</i> Electrons on 2.5 <i>cm</i> of Water	107
8.10	Energy Deposition of 1 <i>MeV</i> Positrons on 2.5 <i>cm</i> of Water	107
8.11	Energy Deposition of 10^6 10 <i>MeV</i> Electrons on 18 <i>cm</i> of Water	108
8.12	Energy-loss Spectra of 10^6 10 <i>MeV</i> Electrons Through 18 <i>cm</i> of Water	108

List of Figures

8.13	Energy Deposition of 10^6 $10MeV$ Electrons on $1.7cm$ of Gold	109
8.14	Energy-loss Spectra of 10^6 $10MeV$ Electrons Through $1.7cm$ of Gold	109

List of Tables

5.1	Continuous slowing down approximation for electrons in gold as computed by MCNP5	49
6.1	Table of values from simulations running 10^7 particles on Gold . . .	74
6.2	Table of values from simulations running 10^7 particles on Water . . .	74
6.3	Table of values from simulations running 10^7 particles on Gold . . .	74
6.4	Table of values from simulations running 10^7 particles on Water . . .	74
6.5	Table of values from simulations running 5×10^7 particles on Gold .	75
6.6	Table of values from simulations running 5×10^7 particles on Water	75
6.7	Table of values from simulations running 10^8 particles on Gold . . .	75
6.8	Table of values from simulations running 10^8 particles on Water . . .	75
6.9	Table of values from simulations running 5×10^7 particles on Gold .	76
6.10	Table of values from simulations running 10^7 particles on Water . . .	76
6.11	Table of values from simulations running 10^7 particles on Gold . . .	76
6.12	Table of values from simulations running 10^7 particles on Water . . .	76

List of Tables

6.13	Table of values from simulations running 10^7 particles on Gold . . .	77
6.14	Table of values from simulations running 10^7 particles on Water . . .	77
6.15	Table of values from simulations running 10^7 particles on Gold . . .	77
6.16	Table of values from simulations running 10^7 particles on Water . . .	77
6.17	Table of values from simulations running 10^8 particles on Gold . . .	78
6.18	Table of values from simulations running 5×10^7 particles on Water	78
6.19	Table of values from simulations running 10^7 particles on Gold . . .	78
6.20	Table of values from simulations running 10^7 particles on Water . . .	78
6.21	Table of values from simulations running 10^7 particles on Gold . . .	79
6.22	Table of values from simulations running 10^7 particles on Water . . .	79
6.23	Table of values from simulations running 10^7 particles on Gold . . .	79
6.24	Table of values from simulations running 10^7 particles on Water . . .	79
7.1	Table of values from 10^8 samples on $9.6 \times 10^{-2}cm$ of Water.	86
7.2	Table of values from 10^7 samples on $1.13cm$ of Water.	86
7.3	Table of values from 5×10^7 samples on $7.5 \times 10^{-2}cm$ of Gold. . . .	86
7.4	Table of values from 10^8 samples on $9.6 \times 10^{-2}cm$ of Water.	87
7.5	Table of values from 10^8 samples on $1.0 \times 10^{-2}cm$ of Gold.	87
8.1	Runtime Comparisons for Spectra Simulations of the LPT Model Against the Benchmark, for Electrons and Positrons.	99

List of Tables

8.2	Energy-flux Moments Comparisons for Simulations of the LPT Model Against the Benchmark, for Electrons and Positrons on Gold and Water.	100
8.3	Run-time Comparisons of Dose Calculations for LPT and Benchmark	106

Chapter 1

Introduction

Numerical simulation of single-event or analog electron and positron transport can be quite onerous. Unlike neutral particles, whose transport can be regarded as a series of free flights between isolated, localized interactions, charged particles in matter experience very large numbers of small, long-range Coulomb interactions[8]. The inefficiencies of analog transport for electrons and positrons stem from large elastic (angular) and inelastic (energy-loss) scattering cross sections which are highly peaked about forward directions and small energy-losses[25]. The mean free paths corresponding to such events are extremely small and lead to inefficient computations. In deterministic settings, extremely fine spatial and energy grids and unacceptably high-order Legendre cross section moments would be necessary to resolve the solutions[18]. In Monte Carlo simulations, the small mean free paths translate to large numbers of collisions which result primarily in very small energy transfers and very small angular deflections. While the small energy-losses and angular deflections make up for the majority of interactions made by electrons and positrons, catastrophic collisions and large angular deflections may cause the particle to lose a large fraction of energy or abruptly turn through a large angle[8]. These large angle and energy-loss differences within a collision, although rare, contribute to the

Chapter 1. Introduction

long tails of significant magnitude in both the angular distribution and energy-loss distribution (known as energy-loss straggling)[17, 2].

The currently most widely used method of simulating electron and positron transport was introduced by Berger as the condensed history Monte Carlo method[1]. This method approximates the analog process by creating an artificially condensed “random walk” from which angular deflections and energy transfers are sampled at the end of an arbitrarily fixed path-length (step) using several infinite medium multiple-scattering theories, which compound the large number of effects into a single step. The angular distributions are attributed to Goudsmit-Saunderson[10] and Moliere[16] while the energy-loss distribution is formulated by Landau[13]. Despite the efficiency gained in condensed history, the approximations are limited to infinite and uniform mediums causing difficulty when faced with material interfaces. Furthermore, the small-angle approximations inherent in the distributions can not manage the large angular deflections and catastrophic collisions accompanying electron and positron transport.

The complexity and inherent limitations of the condensed history algorithm has motivated the continued pursuit of the more simple single-event Monte Carlo simulations. Due to the physical nature of electrons and positrons, angular scattering and energy-loss scattering can be treated independently. Recent work has been done in constructing effective transport formulations[19, 9] that describe the underlying transport mechanics of both processes by systematically approximating the physical interactions to yield longer mean free paths and smoother angular and energy-loss distributions and hence a computationally more efficient single-event Monte Carlo simulation. Accuracy is controlled by enforcing the preservation of important physical information. This physical information comes from moments of the cross sections used within the transport. Lewis showed that by preservation of low-order moments resulted in satisfactory results and further accuracy could be obtained by includ-

Chapter 1. Introduction

ing higher-order moments[15]. These methods discretized the angle and energy-loss formulations providing accurate results for thick slabs. Unfortunately, energy-loss spectra for thin slabs as well as material interfaces have shown to produce artifacts as a result of the discrete representation.

Recent work done by Harding[12] combines the discrete approach of moment-preservation coupled with a continuous model for electron and positron energy-loss transport. The analog cross section is decomposed into a superposition of smooth and singular components. The more probable energy-losses are modeled by a discrete representation of the analog cross section while the less probable energy-losses are represented by the analog cross section. Any artifacts caused by the discrete representation have been smoothed out by coupling it with the exact distribution by essentially approximating higher order moments with greater accuracy. This hybrid method has been proved to yield highly accurate energy spectra and dose profiles, but there is no unique way in implementing this approach.

Further work done by Tolar and Larsen[24] has used the accurate multiple-scattering approximations for angular scattering into what they call a transport condensed history. Rather than moving a particle an artificial distance, the transport process is treated completely in a stochastic manner by constructing energy-dependent mean free paths while preserving zeroth and first order angular moments of the exact solution. This combination of moment-preserving techniques and energy-dependent step-sizes has produced a true transport process with longer mean free paths resulting in faster and more accurate results while eliminating the interface problems and arbitrary step-sizes used in condensed history.

The discontinuous approach of condensed history energy-loss distributions suffer from arbitrariness in step sizes. Discrete moment-preserving methods, although accurate, produce artifacts from the discretization, while the hybrid discrete-continuous model has not been generalized. The motivation for this work comes from the trans-

Chapter 1. Introduction

port condensed history approach taken by Tolar and Larsen[24]. The question we would like to answer is, does there exist a moment-preserving approximation to the energy-loss side of electron and positron transport and can we formulate a true transport process with this approximation? We introduce a continuous pseudo-transport model that uses a moment-preserving cross section to increase the mean free paths resulting in efficiency and accuracy. Under the premise of the accuracy accompanying moment-preserving methods, and the proven accuracy of the Landau energy-loss distribution used in condensed history, we will formulate a single-event pseudo-transport model. We will first begin by investigating Landau's energy-loss straggling distribution and assess the accuracy this distribution. While the latter is widely used in major codes such as MCNP[23] in condensed history simulation, the Landau distribution is used here as a differential cross section to randomly walk particles through single-event Monte Carlo, ensuring the accurate preservation of energy-loss moments of the analog cross section.

This thesis is organized as follows. In Chapter 2, we present the underlying physics of electron and positron transport and the analog transport model. In Chapter 3, we describe the benchmark Monte Carlo solution to the analog transport problem. Chapter 4 describes the Landau theory followed by Chapter 5 which discusses its current implementation in condensed history models. In Chapter 6, we will quantify the accuracy of the Landau energy-loss distribution and follow with a simplified continuous model in Chapter 7. Chapter 8 will contrast numerical results of the benchmark against this model. We close with concluding comments in Chapter 9.

Chapter 2

Analog Problem

2.1 Ionization of Matter by Charged Particles

Unlike neutral particles, charged particles undergo many different types of interactions resulting in kinematic changes. These “swift” charged particles, referring to those particles whose velocities are much higher than velocities of thermal agitation, not only are affected by collisional and absorption phenomena but must also deal with electric fields created by target medium nuclei and electrons. As a result of these Coulomb forces, charged particles do not follow straight paths nor do they collide primarily with nuclei. The examination of charged particle interactions are classified by “light” and “heavy” particles. “Light” particles are those which have the same mass as an electron (i.e., negatrons and positrons) while “heavy” particles are considered to be mesons, protons, etc. The means by which these “swift” particles lose their kinetic energy or are moved throughout the medium are by four principal types of interaction [8]:

1. *Inelastic collisions with atomic electrons* are the primary mechanism by which charged particles lose energy in a medium. As the incident particle collides

Chapter 2. Analog Problem

with the atomic electrons, one or more of the excited electrons either becomes unbound or transitions to an excited state. The unbound electron continues to interact in the same manner causing further electron transitions until it comes to rest. The incident particle is deflected with a change in kinetic energy corresponding to the target atomic electron.

2. *Inelastic collisions with a nucleus* are close, non capture, deflections of the incident charged particle. In some cases, a quantum of radiation is emitted with a kinetic energy equivalent to the magnitude of energy lost by the incident particle. This radiation is also known as bremsstrahlung.
3. *Elastic collisions with a nucleus* results in a non-radiative deflection of the incident particle without exciting the nucleus. The incident particle only loses kinetic energy in the conservation of momentum process between the two particles. This type of interaction is the primary means by which incident electrons are deflected.
4. *Elastic collisions with atomic electrons* occur when an incident charged particle is deflected by the field of electrons of a struck atom. Energy and momentum is conserved and the energy transfer is less than the lowest excitation potential of the target electrons. This results in an interaction with the atom as a whole making elastic collisions with atomic electrons significant for incident electrons with energies $< 100eV$.

This thesis is focused on the inelastic collisions of electrons and positrons. These types of interactions are categorized into two classes, hard and soft collisions. Hard collisions are those in which the energy transfer is large enough for the struck electron to be regarded as initially free. Conversely, soft collisions are those in which the energy transfer is so small the binding of the struck electron must be considered. While the effects of soft collisions can be accounted for by including quantum-mechanical

effects of the atomic electrons, this research will only be concerned with hard collisions.

2.2 Energy-Loss Cross Sections

Hard collisions of electrons and positrons are governed by Coulomb forces. These forces determine the manner in which these incident particles are deflected and lose energy. This work will use two formulations, the Möller and Bhabha differential cross sections, to describe the energy-loss associated with electrons and positrons incident on varying media. The Möller differential cross section for electron energy-loss is given by [8]:

$$\Sigma(E, Q) = \frac{K}{\beta^2} \left[\frac{1}{Q^2} + \frac{1}{(E - Q)^2} + \frac{1}{(E + m_0c^2)^2} + \frac{m_0c^2 (2E + m_0c^2)}{Q (E - Q) (E + m_0c^2)^2} \right] dQ$$

$$Q_{min} \leq Q \leq Q_{max}$$
(2.1)

The Bhabha differential cross section for positrons is given by [8]:

$$\Sigma(E, Q) = \frac{K}{\beta^2} \frac{1}{Q^2} \left\{ 1 - \beta^2 \left[2 \frac{Q}{E} - 3 \frac{Q^2}{m_0c^2} C_\beta - \left(\frac{QE}{m_0c^2} - \frac{Q^3E}{m_0c^4} \right) C_\beta^2 - \left(\frac{Q^2E^2}{m_0c^4} - \frac{Q^3E^3}{m_0c^6} + \frac{Q^4E^2}{m_0c^6} \right) C_\beta^3 \right] \right\} dQ$$

$$Q_{min} \leq Q \leq Q_{max}$$
(2.2)

In Equations 2.1 and 2.2, E represents the incident energy of the particle, Q the energy-loss of the particle after a collision, with the incident particle emerging with

Chapter 2. Analog Problem

energy $E - Q$ and the secondary particle with energy Q (all energies are in units of MeV). β is the ratio of the velocity of the particle to the speed of light (v/c) and $m_0c^2 = 0.511MeV$ is the rest mass energy of the electron. The bounds set for Q will be defined later. The factor C_β in Equation 2.2 is defined by

$$C_\beta = \frac{(1 - \beta^2)}{\beta^2}, \quad (2.3)$$

while the variable K is a material property constant defined by

$$K = \frac{2\pi\rho Z N_{Avo} r_e^2 m_0 c^2}{A}. \quad (2.4)$$

In Equation 2.4, ρ is the material density [$\frac{g}{cm^3}$], Z is the atomic number of the target, N_{Avo} is Avogadro's number, $r_0 = 2.818 \times 10^{-13} cm$ is the classical electron radius and A is the atomic mass of the target. Both differential equations are generalizations of the classical Rutherford cross section defined by

$$\Sigma_{e^\pm}(E, Q) = \frac{K}{\beta^2} \frac{1}{Q^2} dQ \quad (2.5)$$

Figure 2.1 shows the Rutherford cross section for incident electron energies of $10^{-6}MeV$ to $10MeV$ on gold. The $\frac{1}{Q^2}$ term causes a large increase in the cross section since lower energy-losses drive the cross section to a higher degree. Also, lower incident energies further increase the value of the cross section since it is also weighted by $\frac{1}{\beta^2}$. It is important to note that the maximum Q value for each incident energy is not negligible, therefore there is good probability that high energy-losses will arise. It is also noted that as Q goes to 0, $\Sigma_{e^\pm}(E, Q)$ approaches ∞ and therefore a restriction on the minimum Q value must be imposed. Since we are only concerned with hard collisions, the minimum value of Q , Q_{min} , is simply the mean ionization energy of the target material. Q_{min} can be expressed as a function of atomic number

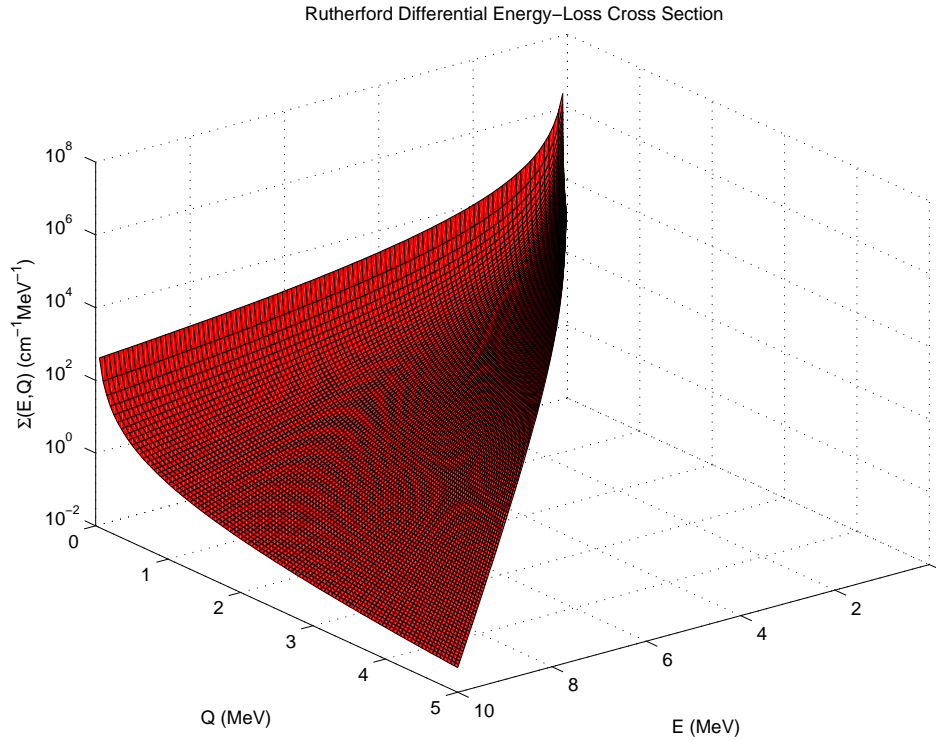


Figure 2.1: Rutherford Differential Cross Section for Electrons on Gold

of the target material by the following equation [25]:

$$Q_{min} = \begin{cases} 19.0 & : Z = 1 \\ 11.2 + 11.7Z & : 2 \leq Z \leq 13 \\ 52.8 + 8.71Z & : Z > 13 \end{cases} \quad (2.6)$$

Based on our definition of inelastic scattering of electrons it is possible that one of them may lose all of its energy in a collision due to the incidence of identical particles, the Möller cross section accounts for this. When electrons collide distinguishability issues arise, the electron is unidentifiable after the collision. Therefore, a limit on the maximum energy-loss Q_{max} , must also be imposed. One will only keep track of the higher energy particle and consider it the primary so that $Q_{max} = E/2$. Figure 2.2 shows the ratio of Möller to Rutherford. As Q gets very small, the ratio

Chapter 2. Analog Problem

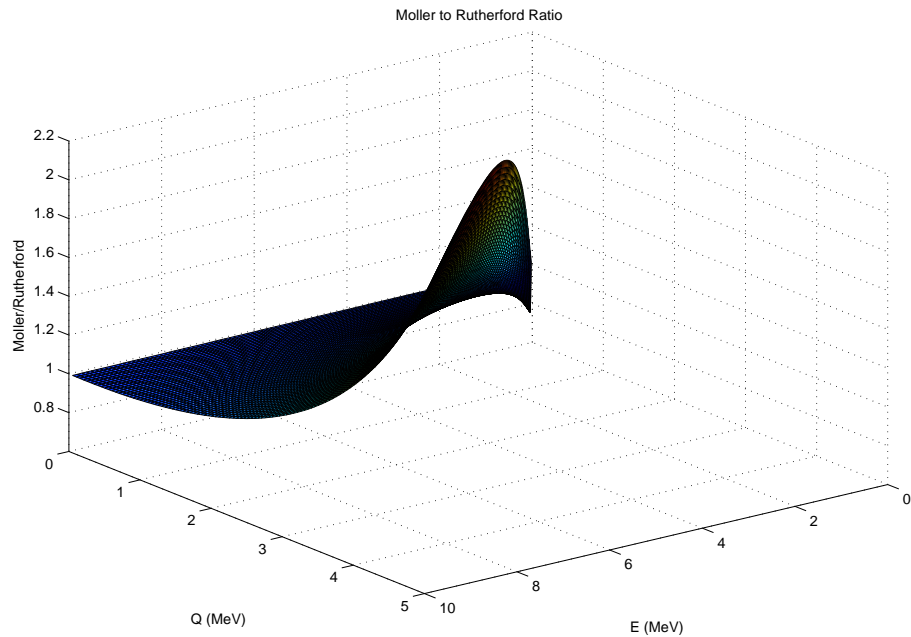


Figure 2.2: Ratio of Möller to Rutherford Differential Cross Sections for Electrons on Gold

approaches unity, i.e., the Möller cross section goes to the Rutherford cross section for low energy-loss transfers. It is also clear that for all values of E , the maximum value of ratio occurs at Q_{max} .

The Bhabha cross section is also distinct from the Rutherford in that it accounts for relativistic and quantum mechanical effects. Unlike the Möller, it takes into account that the positron can be distinguished after the collision, so that $Q_{max} = E$. Figure 2.3 shows the ratio of Bhabha to Rutherford. For this plot, both the Rutherford and Bhabha cross sections were evaluated from Q_{min} to E , to encompass the entire range of energy transfers from 0.001MeV to 10MeV , for positrons. Clearly, as Q goes to Q_{min} the ratio approaches unity like the Möller cross section, yet a major difference arises. Unlike Möller, the ratio of Bhabha to Rutherford does not have a maximum value at Q_{max} . Rather, the maximum is always at Q_{min} .

Chapter 2. Analog Problem

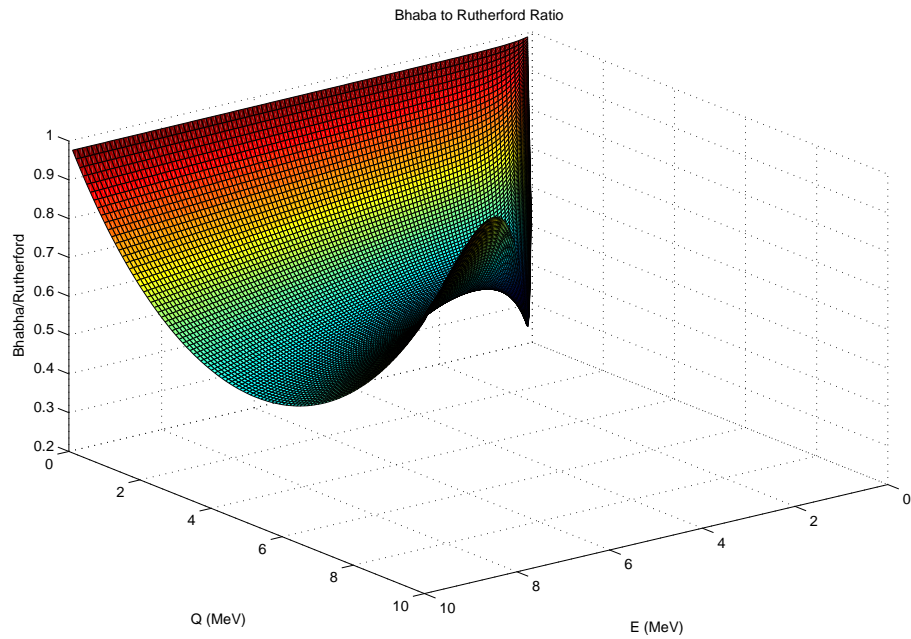


Figure 2.3: Ratio of Bhabha to Rutherford Differential Cross Sections for Electrons on Gold

The importance of maximum values for the ratios of electron and positron cross sections to the Rutherford cross section will be further discussed in Chapter 3. It is important to note that we have only shown the cross sections for particles incident on gold. The cross sections will scale in terms of the variable constant K , yet the distributions will be identical. In terms of the ratio of cross sections, these plots are universal and material independent since the material property variable K cancels out.

2.3 Analog Transport Problem

For purposes of this investigation of electrons and positrons, the linear form of the Boltzmann transport equation with no internal source will be used:

$$\vec{\Omega} \cdot \nabla \psi(\vec{r}, \vec{\Omega}, E) = \int_0^\infty \int_{4\pi} \Sigma_{e^\pm}(\vec{r}, \vec{\Omega} \cdot \vec{\Omega}', E' \rightarrow E) \psi(\vec{r}', \vec{\Omega}', E') d\vec{\Omega}' dE' - \Sigma(\vec{r}, E) \psi(\vec{r}, \vec{\Omega}, E), \quad (2.7)$$

where $\Omega(\mu, \phi)$ is the unit vector describing the direction of the particle in terms of the polar (μ) and azimuthal (ϕ) angles, \vec{r} is the particle's position in Cartesian space, E is the kinetic energy, ψ is the angular flux at \vec{r} with energy E in the direction of $\vec{\Omega}$, Σ_{e^\pm} is the differential cross section for both elastic and inelastic scattering, and $\Sigma(\vec{r}, E)$ is the total cross section at \vec{r} with and energy E . The boundary condition corresponds to a mono-energetic beam incident on the left side of the material under investigation and a vacuum boundary on the opposite side:

$$\psi(0, y, z, \mu, \phi, E) = \frac{1}{2\pi} \delta(\mu - 1) \delta(y) \delta(z), \delta(E_0 - E), \mu > 0 \quad (2.8)$$

$$\psi(X, y, z, \mu, \phi, E) = 0, \mu < 0 \quad (2.9)$$

Decoupling the inelastic and elastic scattering components of the differential scattering cross section are imperative for the work concerned in this thesis. It has been shown that elastic scattering without an associated energy-loss and an inelastic scattering without an associated angular deflection is an accurate description of the slowing down process[22]. The transport equation then becomes:

$$\begin{aligned} \vec{\Omega} \cdot \nabla \psi(\vec{r}, \vec{\Omega}, E) &= \int_{4\pi} \Sigma_{e^\pm}(\vec{r}, \vec{\Omega} \cdot \vec{\Omega}', E) \psi(\vec{r}', \vec{\Omega}', E) d\vec{\Omega}' \\ &+ \int_0^\infty \Sigma_{e^\pm}(\vec{r}, \vec{\Omega}, E' \rightarrow E) \psi(\vec{r}, \vec{\Omega}, E') dE' \\ &- \Sigma(\vec{r}, E) \psi(\vec{r}, \vec{\Omega}, E), \end{aligned} \quad (2.10)$$

Chapter 2. Analog Problem

where the integral containing $\Sigma_{e\pm}(\vec{r}, \vec{\Omega} \cdot \vec{\Omega}', E)$ represents the sum of only elastic interactions and the integral containing $\Sigma_{e\pm}(\vec{r}, \vec{\Omega} \cdot \vec{\Omega}', E' \rightarrow E)$ only describes all inelastic interactions for particles moving from energies E' to E . The total cross section, $\Sigma(\vec{r}, E)$, is still both in terms of elastic and inelastic scattering but can be split in terms of the sum of the two. We can now ignore the elastic scattering terms in Equation 2.10 as well as any angular dependence. We will further simplify this equation by imposing the inelastic scattering conditions described in Section 2.2 for electrons and positrons yielding the one dimensional straight ahead transport equation:

$$\frac{\partial \psi(s, E)}{\partial s} = \int_{E_{min}}^{E_{max}} dE' \Sigma_{e\pm}(E' \rightarrow E) \psi(s, E') - \Sigma(E) \psi(s, E) \quad (2.11)$$

$$\psi(0, E) = \delta(E - E_0). \quad (2.12)$$

In Equation 2.11, E_{min} and E_{max} represent range of energies in question, s is the path length of the particle, E is the emerging energy of the particle, $\psi(s, E)$ is the energy distribution at s . Equation 2.11 can be expressed alternatively in terms of the energy-loss variable $Q = E' - E$, defining $\Sigma_{e\pm}(E, Q)dQ$ such that

$$\Sigma_{e\pm}(E' \rightarrow E)dE = \Sigma_{e\pm}(E + Q, Q)dQ, \quad (2.13)$$

giving

$$\frac{\partial \psi(s, E)}{\partial s} = \int_{Q_{min}}^{Q_{max}} \Sigma_{e\pm}(E + Q, Q) \psi(s, E + Q) dQ - \Sigma(E) \psi(s, E) \quad (2.14)$$

$$\psi(0, E) = \delta(E - E_0). \quad (2.15)$$

The result from Equation 2.14 allows us to use this total cross section with an incident energy E of the particle in question without any angular dependence. Using the definitions of the differential cross sections for electrons and positrons by Möller (Eq. 2.1) and Bhabha (Eq. 2.2), the total cross section is found by:

$$\Sigma_{e\pm} = \int_{Q_{min}}^{Q_{max}} \Sigma_{e\pm}(E, Q) dQ. \quad (2.16)$$

2.4 Energy-Loss and Flux-Energy Moments

Statistical moments of any given distribution describe specific aspects of the distribution itself. These moments help to characterize the physics of the cross section in an alternative manner as well as the energy distribution in the flux. Recent work has been done in moment-preserving approximations for energy straggling in an attempt to explicitly construct approximate transport models to preserve a finite number of moments of the analog differential cross section yielding more accurate energy spectra and dose distributions[24, 12, 15]. The ability to capture specific moments of the differential cross sections has been proven to increase the computational efficiency and accuracy of condensed history methods allowing longer “mean free paths” and thus reducing the computational time of the transport model. More specifically, Lewis[15] has shown, with the assumption of single energy particles in an infinite medium, two transport models with dissimilar scattering cross sections but with identical Legendre moments through order N will have the same space-angle moments of the angular flux also through order N . This has led to the development of pseudo-transport models that can be efficiently simulated by single-event Monte Carlo and have become a worthwhile alternative to condensed history.

2.4.1 Energy-Loss Moments of the Differential Cross Section

The moments of the energy-loss cross section for electrons and positrons are defined as:

$$Q_{e^\pm, n} = \int_{Q_{min}}^{Q_{max}} Q^n \Sigma_{e^\pm}(E, Q) dQ, \quad (2.17)$$

where $n = 1, 2, \dots, N$, Q_n is the n th moment of the energy-loss cross section. As stated above, these moments characterize the physics in the energy-loss cross sections. For example, the first moment Q_1 , is the average energy-loss of the particle per unit

Chapter 2. Analog Problem

length in the medium, the second moment is the mean-squared energy-loss per unit length. The average energy-loss is also known as the stopping power of the particle which describes the mean energy lost in the medium per distance traveled [MeV/cm]. The mean-squared [MeV^2/cm] energy-loss describes a straggling about the mean or the deviation from the average energy-loss. Comparisons of the first six energy-loss moments are plotted in Figures 2.4-2.7 for electrons/positrons of $10^{-3}MeV$ to $20MeV$ incident on gold and water.

With the exception of the Q_1 moment, as the energy increases the dominance of the higher moments becomes evident. The steep decline of Q_2 and sharp peak of Q_1 are due to the logarithmic terms within both the electron and positron moments. After the second moment these logarithmic terms drop out and the moments increase monotonically. Based on Figures 2.4-2.7 the same trend holds true for different materials, only the magnitude of the distributions are different due to the material constant K .

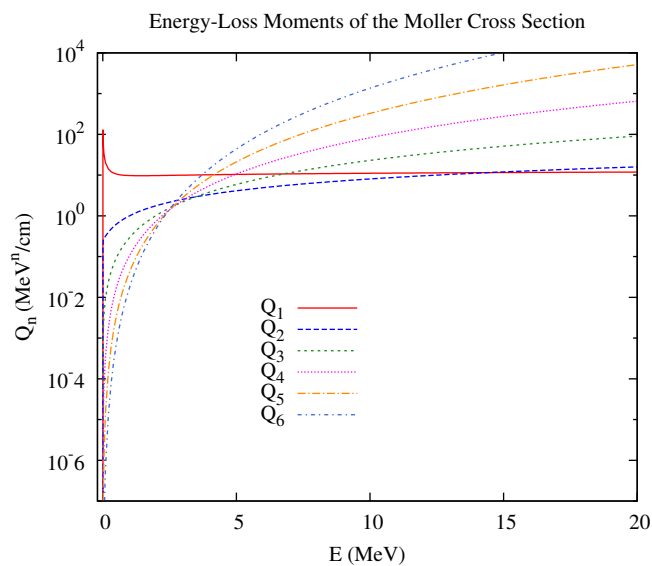


Figure 2.4: First 6 Energy-Loss Moments, Electrons on Gold

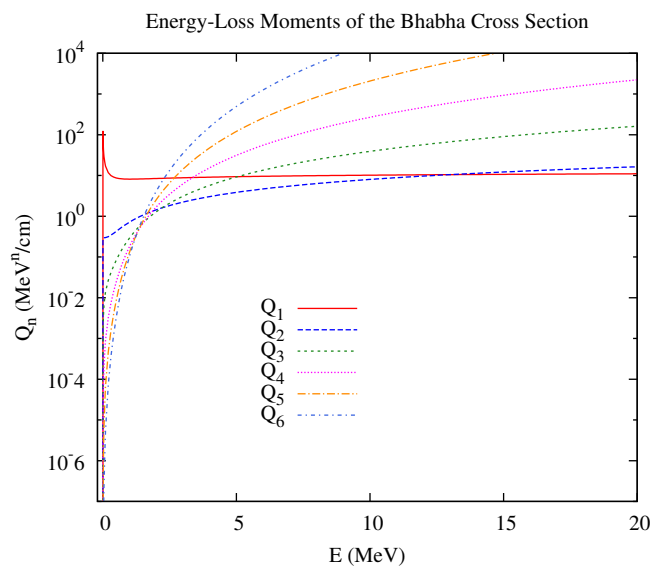


Figure 2.5: First 6 Energy-Loss Moments, Positrons on Gold

Chapter 2. Analog Problem

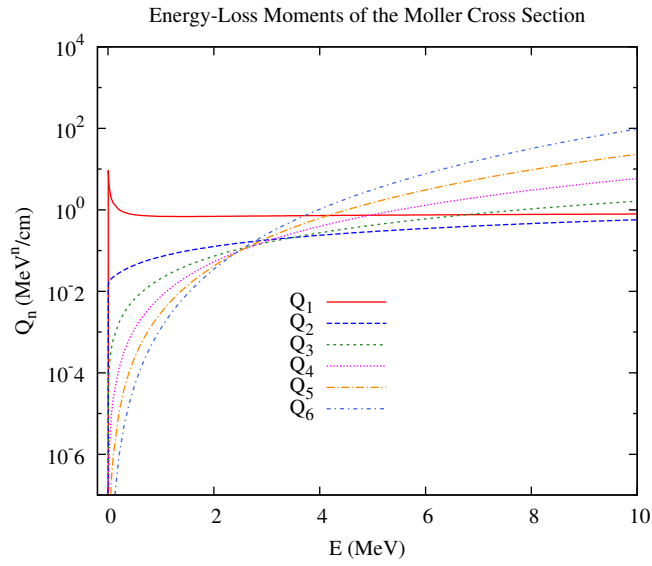


Figure 2.6: First 6 Energy-Loss Moments, Electrons on Water

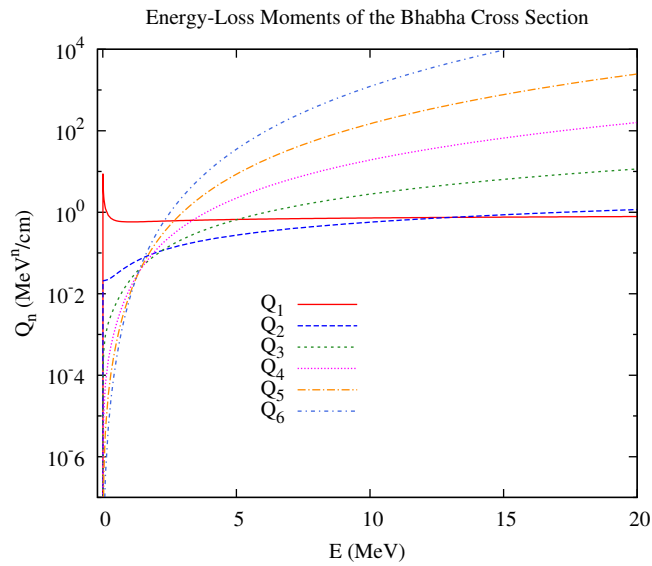


Figure 2.7: First 6 Energy-Loss Moments, Positrons on Water

2.4.2 Energy-Flux Moments

It has been shown [12] that for thin targets where condensed history straggling models [13] hold, and for thin enough targets where the energy within the mean free path is considered constant, that the accuracy of energy straggling models are directly related to the number of energy-loss moments preserved. This leads to the suggestive conclusion that if moments of the energy-loss differential cross section are preserved than the preservation of energy moments of the flux must also provide an indication of accuracy as well. We will examine this relationship in detail later in the thesis. Here we introduce the energy moments of the flux:

$$I_{e^\pm, n}(s) = \int_{E_{min}}^{E_{max}} E^n \psi_{e^\pm}(s, E) dE. \quad (2.18)$$

$I_0(s) = 1$ which is simply the percentage of particles that traveled a path length s , $I_1(s)$ defines the mean energy of particles that traveled a distance s , $I_2(s)$ the mean squared energy and so on.

Chapter 3

Monte Carlo Solution of the Analog Problem

Monte Carlo techniques are a valid and accurate means of simulating charged particle transport, although at the cost of computational complexity due to a high magnitude of collisions. Monte Carlo does not attempt to solve the transport equation, rather it uses stochastic techniques of random sampling in order to find a solution. Analog simulation, although highly inefficient, provides an accurate model for electron/positron transport where the uncertainty is statistical and therefore a valid means of producing a benchmark that will be compared to in further chapters.

In the following sections a detailed description of an analog Monte Carlo simulation of electron and positron energy-loss, using the physics described in Chapter 2, is presented.

3.1 Random Walk

Equation 3.1 is the benchmark problem that we are going to solve. Again, it is the one-dimensional, angle-independent, straight-ahead transport equation for electrons and positrons.

$$\frac{\partial \psi(s, E)}{\partial s} = \int_{Q_{min}}^{Q_{max}} \Sigma_{e^{\pm}}(E + Q, Q) \psi(s, E + Q) dQ - \Sigma(E) \psi(s, E) \quad (3.1)$$

$$\psi(0, E) = \delta(E - E_0).$$

Each one of the terms in Equation 3.1 describes different aspects of the particle's movement and interaction through the medium, and will allow us to randomly sample interactions and create a "random walk" through the material in question. The interactions are described by the following terms:

1. $\Sigma(E)ds$ is the probability that a particle with an energy E will experience a collision in a distance ds .
2. $\Sigma(E, Q)dQ$ is the probability that a particle with an energy of E will experience a collision resulting in an energy-loss equal to Q .

Based on the formulation of these terms, it is clear that the distance s the particle travels is independent of the energy-loss Q that it experiences in a collision. As a result, it is possible to describe both equations by a probability density function (PDF) and sample randomly from each of these PDF's to obtain the random walk of the particle by the following sequence:

1. Define the source of the particle and boundary conditions of the medium.
2. Track the distance of the particle by randomly selecting a distance to collision from the relative PDF.

3. Formulate the interaction (in our case energy-loss) of the particle at this collision site by randomly sampling from an energy-loss PDF.
4. Repeat steps 2 and 3 until the particle has either lost all energy, or has traversed the slab in question.

As each of these particles are sampled, energy, energy-flux moments, and other important data will be stored.

3.2 Distance to Collision

In order to properly sample a distance to collision, it is required that through the flight of the particles' path the energy must remain constant. With this restriction, we know that [14] the distribution of particles traveling a distance s with a given energy E is exponential. By multiplying the probability of a particle traveling a distance s by the probability of it suffering a collision in a distance s and $s + ds$ we get the following PDF describing the probability of a particle traveling s will have a collision:

$$P_{coll}(s)ds = e^{-\Sigma(E)s}\Sigma(E)ds. \quad (3.2)$$

It can easily be shown [5] that the respective cumulative distribution function (CDF) of the PDF is equal to:

$$C_{coll} = \int_0^s P_{coll}(s')ds' = 1 - e^{-\Sigma(E)s} \quad (3.3)$$

The benefit of the CDF comes from its distribution being uniform over (0,1). By sampling a uniformly distributed random number ξ from (0,1) allows us to randomly choose a corresponding value for the distance to collision. Once ξ is chosen, set it

Chapter 3. Monte Carlo Solution of the Analog Problem

equal to the integral in Equation 3.3, and solve for a distance s traveled:

$$\begin{aligned}\xi &= 1 - e^{-\Sigma(E)s} \\ s &= -\frac{1}{\Sigma(E)} \log \xi, \quad \xi = 1 - \xi\end{aligned}\tag{3.4}$$

Equation 3.4 will now directly sample a distance to collision s for a particle at a given energy E with a total cross section $\Sigma(E)$.

3.3 Energy-Loss

Chapter 2 has defined for us the type of particle interactions that we are interested in and their corresponding differential cross sections (i.e. Möller for electrons, Bhabha for positrons). We will use the definition of $\Sigma(E, Q)dQ$ and $\Sigma(E)$ to formulate a PDF:

$$P(Q) = \frac{\Sigma(E, Q)dQ}{\Sigma(E)},\tag{3.5}$$

yielding the following CDF:

$$C(Q) = \frac{\int_{Q_{min}}^Q \Sigma(E, Q')dQ'}{\Sigma(E)}.\tag{3.6}$$

Equating Equation 3.6 to a randomly distributed variable ξ on (0,1) and solving for Q will give a direct way of sampling an energy-loss. Using the Rutherford cross section given by Equation 2.5, for which the integration can be carried out, provides this simple result for an energy-loss Q :

$$Q = \left(\frac{1}{Q_{min}} - \frac{\xi \Sigma(E)}{K/\beta^2} \right)^{-1}\tag{3.7}$$

Unlike the Rutherford cross section, Möller and Bhabha contain terms that are more complicated. Taking the integral of the differential cross sections over the interval

Q_{min} to Q for Möller and Bhabha respectively gives:

$$\int_{Q_{min}}^Q \Sigma_{e^\pm}(E, Q') dQ' \implies$$

$$\Sigma_{e^-}(E) \Big|_{Q_{min}}^Q = \frac{K}{\beta^2} \left[\left(\frac{1}{Q_{min}} - \frac{1}{Q} \right) + \left(\frac{1}{(E-Q)} - \frac{1}{(E-Q_{min})} \right) \right. \\ \left. + \frac{Q-Q_{min}}{(E+m_0c)^2} + \frac{m_0c(2E+m_0c)}{(E+m_0c)^2} \log \left(\frac{Q(E-Q_{min})}{Q_{min}(E-Q)} \right) \right] \quad (3.8)$$

$$\Sigma_{e^+}(E) \Big|_{Q_{min}}^Q = \frac{K}{\beta^2} \left\{ \left(\frac{1}{Q_{min}} - \frac{1}{Q} \right) - \beta^2 \left[(a_1) \log \left(\frac{Q}{Q_{min}} \right) \right. \right. \\ \left. \left. - a_2(Q-Q_{min}) + \frac{a_3}{2}(Q^2-Q_{min}^2) - \frac{a_4}{3}(Q^3-Q_{min}^3) \right] \right\}, \quad (3.9)$$

$$a_1 = \frac{2}{E} - \frac{E}{[m_0c^2]^2} C_\beta^2$$

$$a_2 = \left(\frac{3}{[m_0c^2]^2} + \frac{E^2}{[m_0c^2]^4} C_\beta^2 \right) C_\beta$$

$$a_3 = \left(\frac{1}{[m_0c^2]^4} + \frac{E^2}{[m_0c^2]^6} C_\beta \right) EC_\beta^2$$

$$a_4 = \frac{E^2 C_\beta^3}{[m_0c^2]^6}.$$

Equation 3.8 and 3.9 contain terms that can not be inverted exactly and therefore the CDF can not be directly sampled. It is necessary to use an indirect method of sampling an energy-loss Q .

3.3.1 Rejection Method Solution

It has already been shown [12] that the most efficient manner in which to sample from our given energy-loss differential cross sections is by means of a rejection method. By redefining our PDF in terms of a different cross section only dependent on Q for electrons and positrons:

$$P(Q) = \frac{K F(Q)}{\beta^2 \Sigma(E)} \quad (3.10)$$

Chapter 3. Monte Carlo Solution of the Analog Problem

where $F(Q)$ is defined as:

$$F(Q) = \frac{1}{Q^2}g(Q), \quad (3.11)$$

and $g(Q)$ is given by:

$$g(Q) = Q^2\Sigma_{e^\pm}(E, Q). \quad (3.12)$$

By removing the factor of $1/Q^2$ allows us to sample directly from $\frac{K}{\beta^2} \frac{1}{Q^2}$ and reject this value of Q if it does not belong in the distribution of $g(Q)$. The rejection is done by sampling a random number uniformly distributed over (0,1) and setting it equal to the ratio of $g(Q)$ and its maximum value $g_{max}(Q)$. It is important to notice that $\frac{K}{\beta^2} \frac{1}{Q^2}$ is simply the Rutherford cross section. It has been shown in Chapter 2 that for electrons $g_{max} = g(Q_{max})$ and for positrons $g_{max} = g(Q_{min})$. The following scheme is used to sample an energy-loss for electrons and positrons:

First sample a potential energy-loss directly from Rutherford(Eq 3.3)

$$Q = \left(\frac{1}{Q_{min}} - \frac{\xi_1 \Sigma_{e^{-,+}}(E)}{K/\beta^2} \right)^{-1}$$

Next sample another random variable and verify the ratio $\frac{g}{g_{max}}$

if $\xi_2 \leq \frac{g}{g_{max}}$ accept,

else sample a new ξ_1

where ξ_1 and ξ_2 are randomly distributed variables between 0 and 1, and g_{max} is equal to its respective distribution. This sampling is looped until a value of Q is accepted and the “random walk” of the particle continues.

3.4 Statistical Evaluation of Monte Carlo

Due to the stochastic nature of the Monte Carlo method, it is necessary to use a reliable and well tested pseudo-random number generator (PRNG) and define a

measurement of accuracy for our results. The PRNG used comes from MCNP5 [6]. This 64-bit PRNG will allow us to reproduce any simulations providing experimental consistency and simplification of necessary debugging.

This thesis will be concerned with quantities such as energy-loss spectra, energy deposition, and moments of energy-flux. These values will be tallied or stored to provide information concerning distributions of energy-loss straggling and dose.

3.4.1 Energy-Loss Spectra

Energy-loss spectra tallies consist of tallying particle energy-losses after traversing a medium and placing them into appropriate energy bins. For our purposes, these bins will be equally distributed about the range Q_{min} to E and once the simulation is finished, normalized by the total number of particles and the width of the energy bin to provided units of flux [$\#/MeV^{-1}$]. The energy-loss of each particle is determined by the difference of the initial energy and the outgoing energy of the particle.

The accuracy of Monte Carlo method is completely dependent on the number of N particles used in the simulation. More specifically, the value of the 1σ relative error will be used which decreases by \sqrt{N} . In order to produce the 1σ relative error, it is necessary to run simulations in cycles of particles (nc). The number of particles in a cycle (npc) is simply determined by:

$$npc = \frac{N}{nc} \quad (3.13)$$

where N is the total number of particles in the simulation and nc will always be chosen to be 50. Next we must define the number of particles tallied in the i th bin for cycle j as nb_{ij} , the energy value contained in each bin is:

$$E_{ij} = \frac{nb_{ij}}{npc\Delta E} \quad (3.14)$$

where ΔE is the energy bin width. The mean value for each bin is then defined as:

$$\bar{E}_i = \frac{1}{nc} \sum_{j=1}^{nc} E_{ij}. \quad (3.15)$$

The variance for each bin is then calculated by:

$$\begin{aligned} \sigma_i^2 &= \frac{1}{nc-1} \sum_{j=1}^{nc} (E_{ij} - \bar{E}_i)^2 \\ &= \frac{1}{nc-1} \sum_{j=1}^{nc} (E_{ij}^2 - 2E_{ij}\bar{E}_i + \bar{E}_i^2) \\ &= \frac{1}{nc-1} \left[\sum_{j=1}^{nc} E_{ij}^2 - 2\bar{E}_i \sum_{j=1}^{nc} E_{ij} + \sum_{j=1}^{nc} \bar{E}_i^2 \right] \\ &= \frac{1}{nc-1} \left[\sum_{j=1}^{nc} E_{ij}^2 - 2nc\bar{E}_i \frac{1}{nc} \sum_{j=1}^{nc} E_{ij} + nc\bar{E}_i^2 \right] \\ &= \frac{1}{nc-1} \left[\sum_{j=1}^{nc} E_{ij}^2 - 2nc\bar{E}_i^2 + nc\bar{E}_i^2 \right] \\ &= \frac{1}{nc-1} \left[\sum_{j=1}^{nc} E_{ij}^2 - nc\bar{E}_i^2 \right] \\ &= \frac{nc}{(nc-1)} \left[\frac{1}{nc} \left(\sum_{j=1}^{nc} E_{ij}^2 \right) - \bar{E}_i^2 \right]. \end{aligned} \quad (3.16)$$

From the variance we can now calculate the standard deviation and finally the 1σ relative error by:

$$\sigma_i = \sqrt{\sigma_i^2} \quad (3.17)$$

$$RE_{1\sigma} = \frac{\sigma_i}{\bar{E}_i} \quad (3.18)$$

3.4.2 Energy Deposition

Energy deposition, or dose, of individual particles are tallied over the range of a thick slab in question. For our purposes we will use equidistant layers or bins. After

each particle collision, an energy-loss is calculated, that energy-loss is then placed in the respective bin based on the penetration of the particle within the slab. Once a specified number of particles i have been tallied, the sum of energy-losses Q_i in the j th bin is then normalized by the total number of particles sampled N , the bin width Δx , and the density of the material ρ to give the energy deposited D_j in bin j in units of $[MeV cm^2/g]$:

$$D_j = \frac{1}{N\Delta x\rho} \sum_i^N Q_i. \quad (3.19)$$

As seen in energy-loss, we must split our statistics in terms of particle cycles in order to obtain 1σ relative error yielding the following equation for the mean dose in bin j for cycle k :

$$\overline{D}_j = \frac{1}{nc} \sum_{k=1}^{nc} D_{jk} \quad (3.20)$$

and the variance becomes

$$\begin{aligned} \sigma_j^2 &= \frac{1}{nc-1} \sum_{k=1}^{nc} (D_{jk} - \overline{D}_j)^2 \\ &= \frac{nc}{(nc-1)} \left[\frac{1}{nc} \left(\sum_{k=1}^{nc} D_{jk}^2 \right) - \overline{D}_j^2 \right]. \end{aligned} \quad (3.21)$$

Now we may obtain the standard deviation and 1σ relative error by

$$\sigma_i = \sqrt{\sigma_i^2} \quad (3.22)$$

$$RE_{1\sigma} = \frac{\sigma_i}{D_j} \quad (3.23)$$

3.5 Benchmark Solutions

Now that the analog transport model has been defined and the method of statistical measurement has been shown, we define the simulations that will become the benchmark solutions for electron and positron transport. Examination of the energy-loss

and energy-flux moments will be done as well as CPU runtime, number of collisions, etc. The materials that will be examined are gold and water. The purpose of these materials is to provide an examination of low and high Z materials as well as a difference in material type. Both energy-loss and energy deposition of energies at 1MeV and 10MeV have been plotted with respective 1σ relative errors. The slab lengths are relative to electron steps (Estep) which will be thoroughly discussed in Chapter 5. For purposes of organization, energy-loss spectra will be presented followed by energy deposition. These solutions will be shown in sections of material and sub-sectioned by increasing energy.

3.5.1 Gold

1 MeV

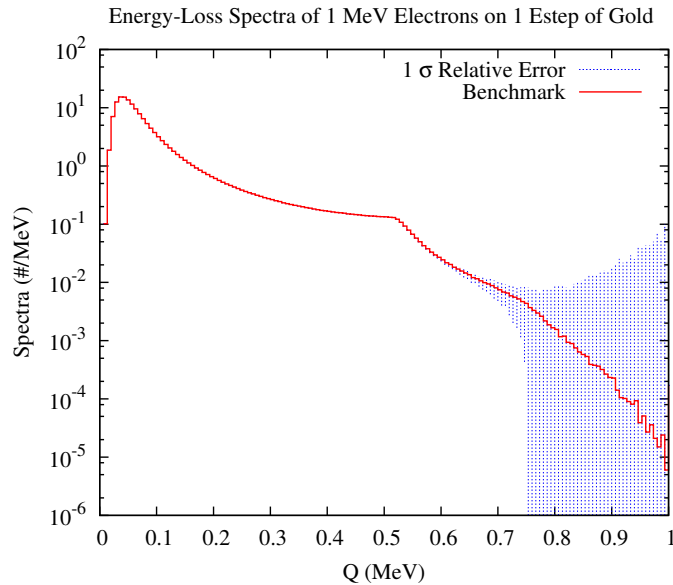


Figure 3.1: Energy-Loss Spectra of 1 MeV Electrons on $8.515 \times 10^{-3}\text{cm}$ of Gold

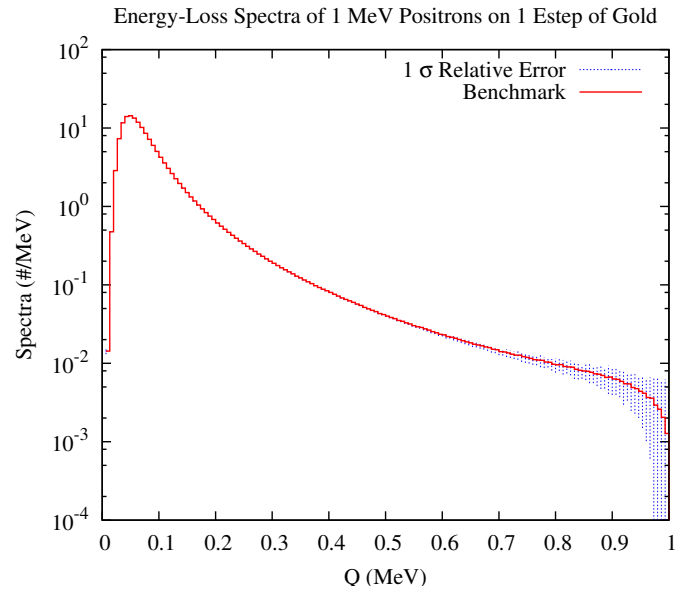


Figure 3.2: Energy-Loss Spectra of 1 MeV Positrons on $8.515 \times 10^{-3} \text{cm}$ of Gold

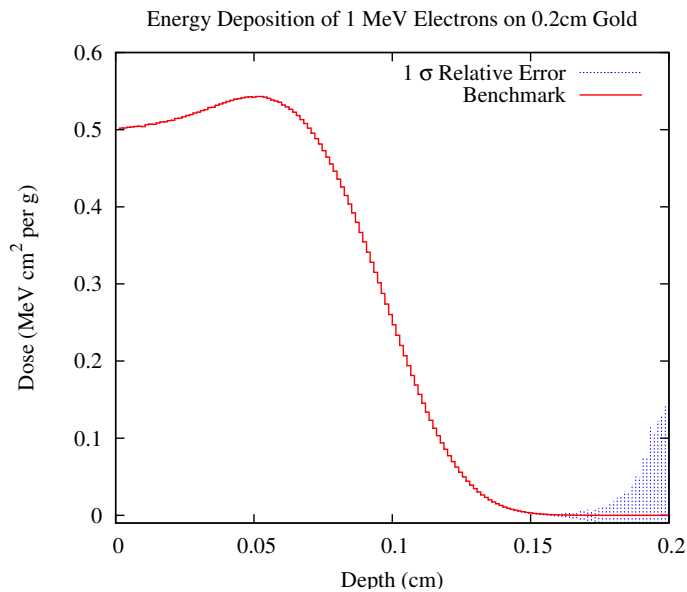


Figure 3.3: Energy Deposition of 1 MeV Electrons on $2.0 \times 10^{-1} \text{cm}$ of Gold

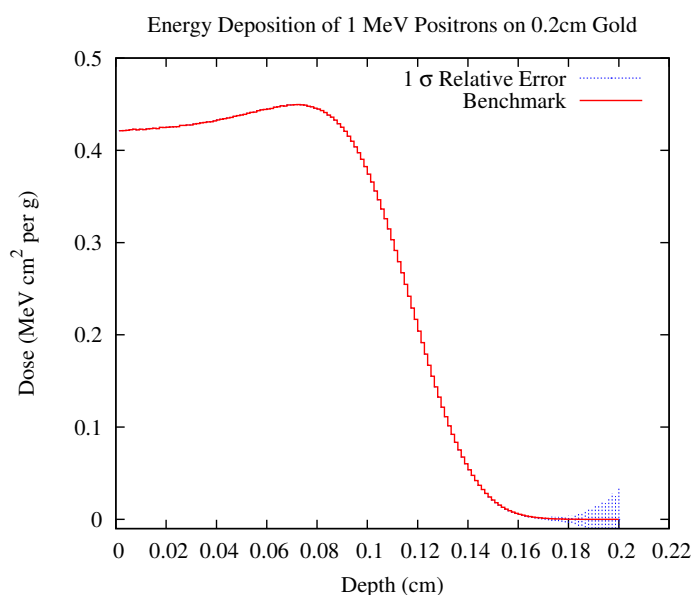


Figure 3.4: Energy Deposition of 1 *MeV* Positrons on $2.0 \times 10^{-1}cm$ of Gold

10 MeV

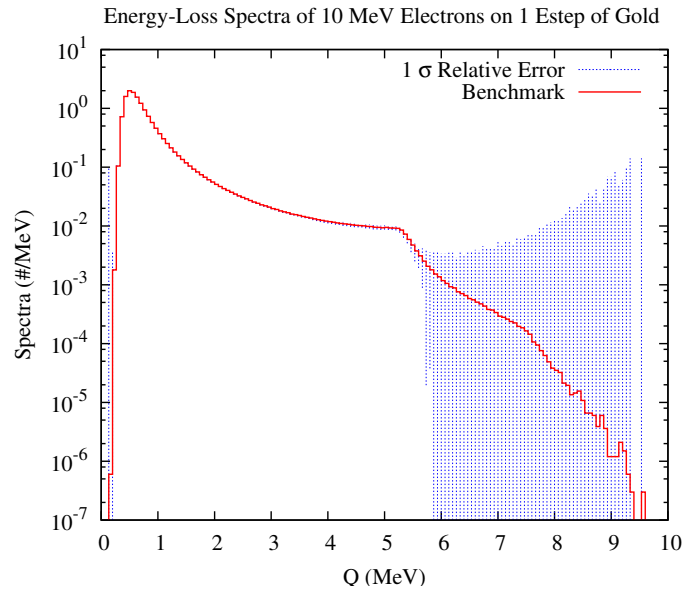


Figure 3.5: Energy-Loss Spectra of 10 *MeV* Electrons on $7.47 \times 10^{-2}cm$ of Gold

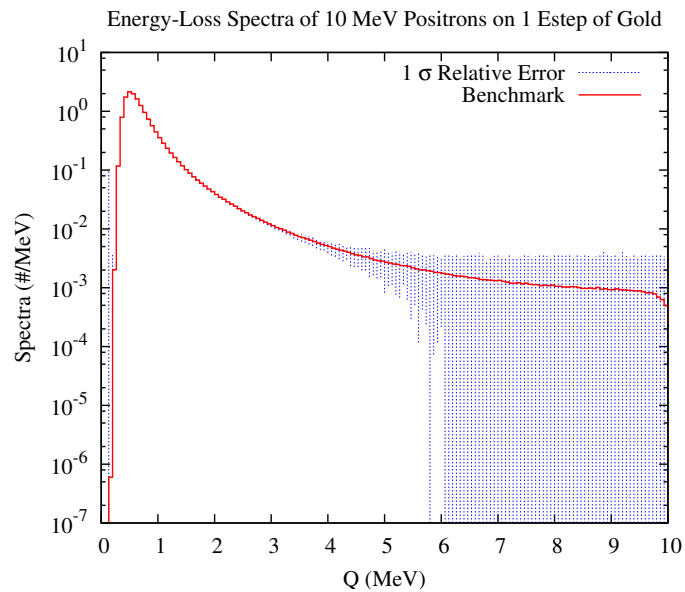


Figure 3.6: Energy-Loss Spectra of 10 *MeV* Positrons on $7.47 \times 10^{-2}cm$ of Gold

Chapter 3. Monte Carlo Solution of the Analog Problem

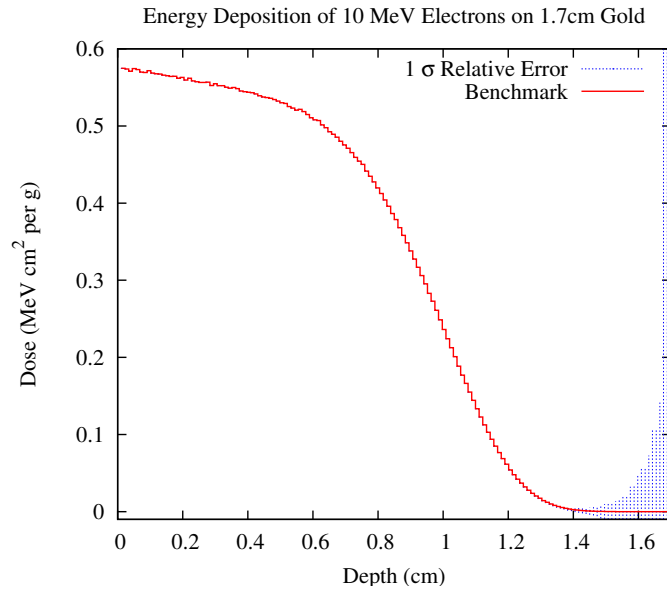


Figure 3.7: Energy Deposition of 10 *MeV* Electrons on 1.7*cm* of Gold

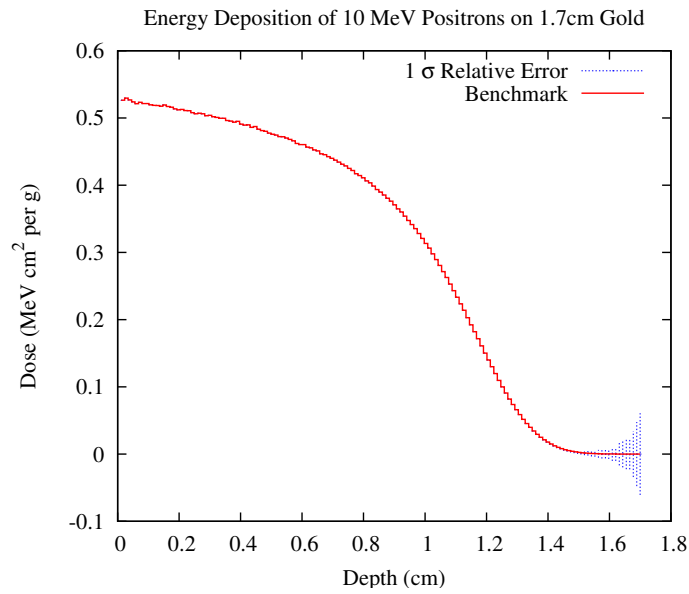


Figure 3.8: Energy Deposition of 10 *MeV* Positrons on 1.7*cm* of Gold

3.5.2 Water

1 MeV

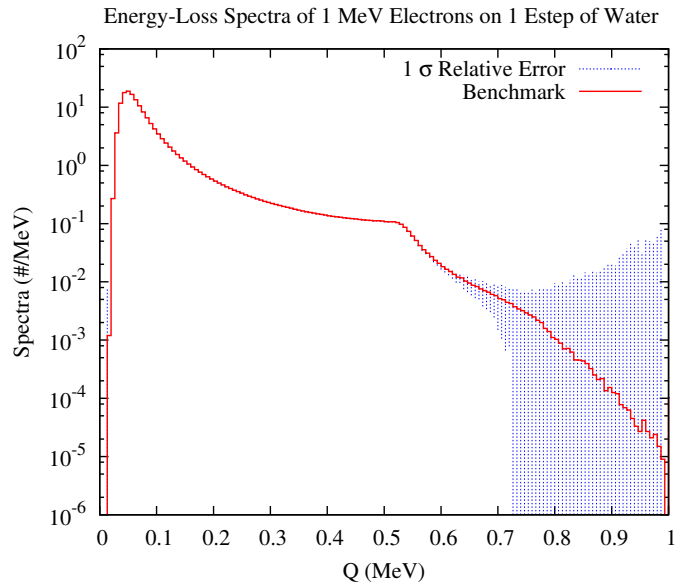


Figure 3.9: Energy-Loss Spectra of 1 MeV Electrons on $9.633 \times 10^{-2} cm$ of Water

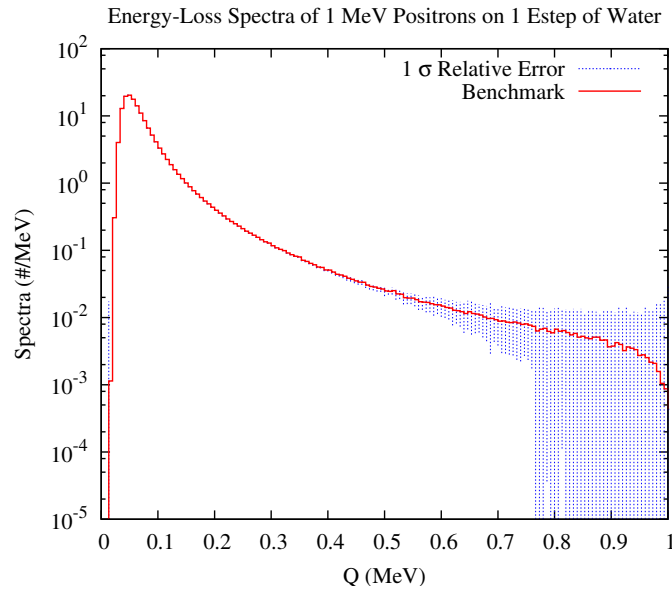


Figure 3.10: Energy-Loss Spectra of 1 MeV Positrons on $9.633 \times 10^{-2} cm$ of Water

Chapter 3. Monte Carlo Solution of the Analog Problem

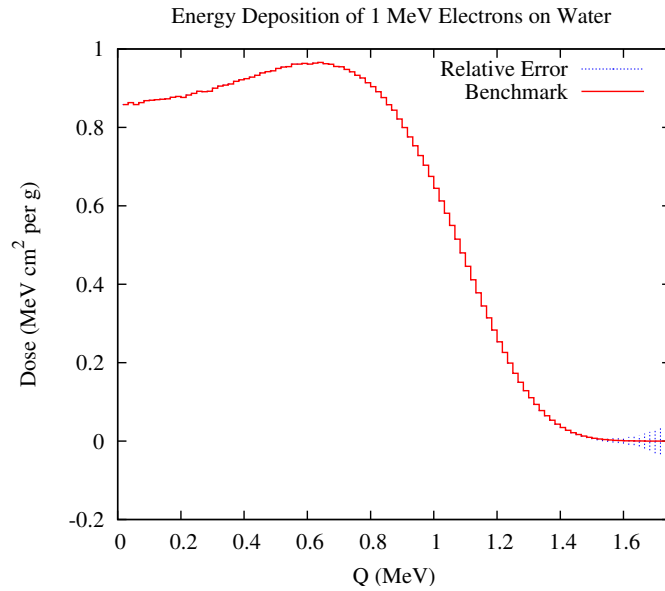


Figure 3.11: Energy Deposition of 1 MeV Electrons on 1.6cm of Water

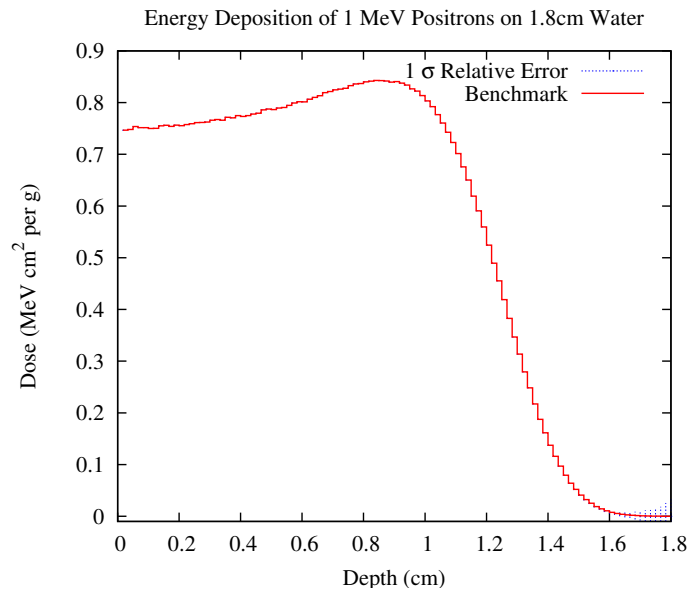


Figure 3.12: Energy Deposition of 1 MeV Positrons on 1.8cm of Water

10 MeV

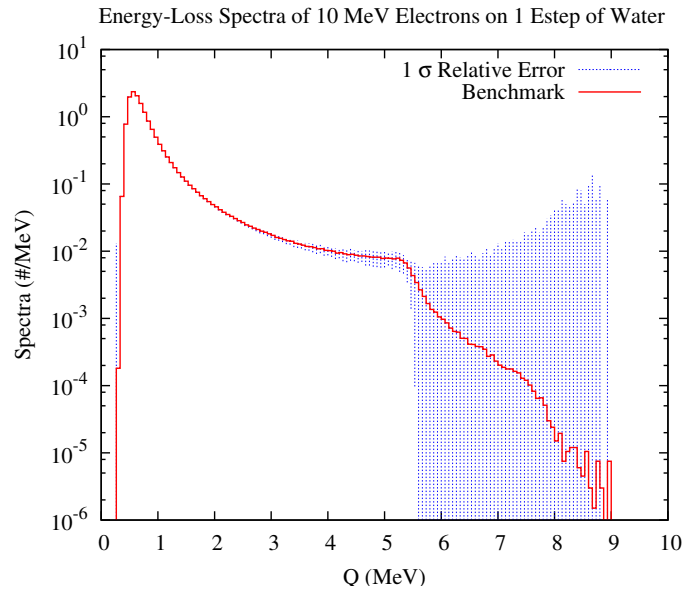


Figure 3.13: Energy-Loss Spectra of 10 MeV Electrons on 1.131cm of Water

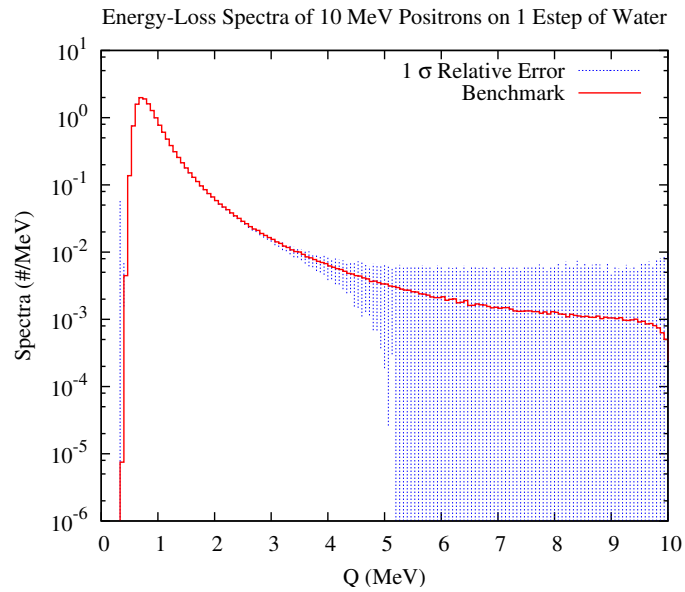


Figure 3.14: Energy-Loss Spectra of 10 MeV Positrons on 1.131cm of Water

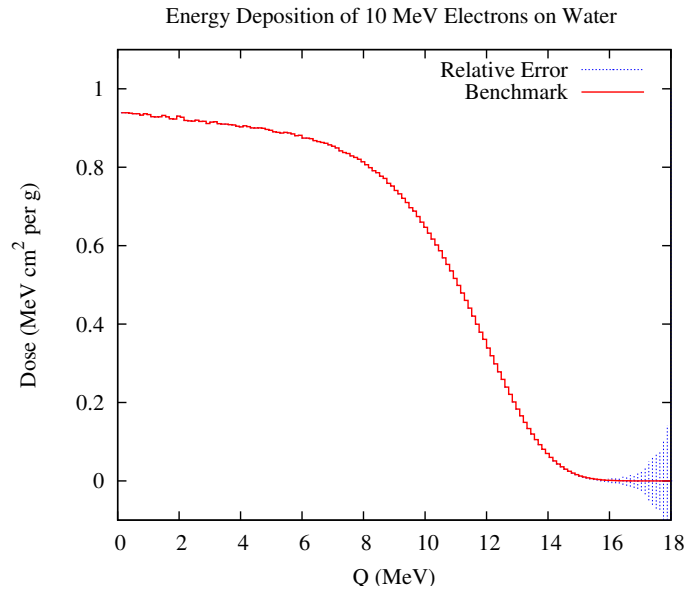


Figure 3.15: Energy Deposition of 10 MeV Electrons on 18cm of Water

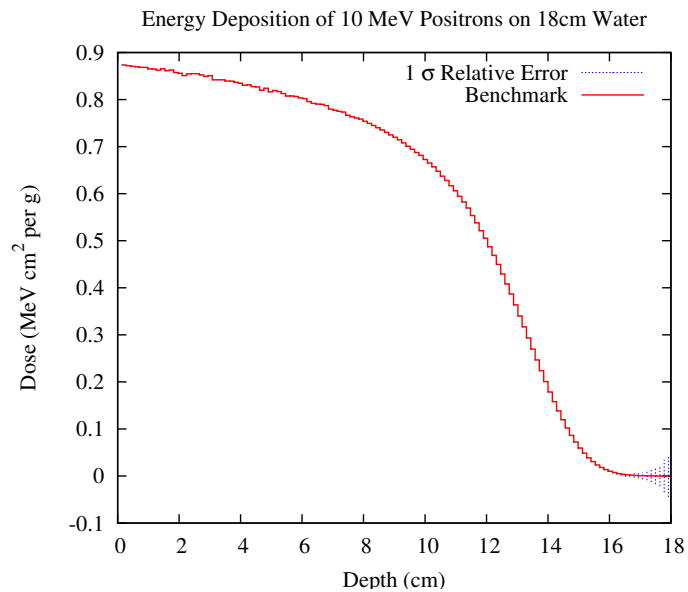


Figure 3.16: Energy Deposition of 10 MeV Positrons on 18cm of Water

Chapter 4

Landau Theory

As seen in Chapter 3, analog transport of electrons and positrons is very inefficient due to the large number of collisions suffered by the particle. In an attempt to mitigate the number of interactions and computational complexity, Berger[1] introduced the condensed history method which “condenses” multiple-scattering events into one single event. In contrast to the “random walk”, the particle is moved a fixed path-length (or step), and the angle and energy distribution is determined using several infinite medium multiple-scattering theories, which combine the effects of the large number of interactions that occur within the step. These multiple-scattering theories include the Goudsmit-Saunderson [10] and Moliere [10] distributions for angular scattering, and the Landau[13] distribution for energy-loss straggling. While this method has been studied and utilized, it suffers from systematic errors from the limitations of multiple-scattering theories and arbitrariness of the step sizes.

The following sections describe the derivation of the Landau energy straggling distribution, the manner in which it is being implemented in current condensed history codes, and how it compares to the benchmark solution defined in Chapter 3.

4.1 Derivation

The Landau energy-loss distribution is based on the assumption that *fast particles* traversing a *thin layer* of material will experience a form of straggling about the mean energy-loss for a given energy over a specific step size. These implications are defined such that:

- *fast particles* are those in which the energy is sufficiently large that ionization theory may be applied, yet
- the *thin layer* of material in which it is traversing is thin enough that the mean total energy-loss is small compared with the initial energy of the particle.

Landau defines a distribution function $f(x, \Delta)$ (where the integral is normalized to 1) as the probability that a particle with an energy E_0 upon traversing a layer x will lose an amount of energy $\Delta = E_0 - E$. Next, a balance kinetic equation is constructed, defined by the change of the distribution function $\frac{df}{dx}dx$ over a short distance dx and the “collision integral” which expresses the difference in the number of particles that acquire, due to ionization losses along dx , an energy E , and the number of particles which leave the given energy interval. Defining:

$\omega(E, \epsilon) \equiv$ probability per unit path length of an energy-loss ϵ
for a particle of energy E

$\omega(\epsilon) = \omega(E_0, \epsilon)$, where E_0 is the initial energy of the
particle on the boundary

$f(x, \Delta - \epsilon) \equiv$ number of particles which acquire a given energy E
along dx with an energy-loss ϵ

$f(x, \Delta) \equiv$ number of particles that do not suffer an energy-loss ϵ

Chapter 4. Landau Theory

the balance equation is given by:

$$\frac{\partial f(x, \Delta)}{\partial x} = \int_0^\infty \omega(\epsilon) [f(x, \Delta - \epsilon) - f(x, \Delta)] d\epsilon, \quad f(0, \Delta) = \delta(\Delta) \quad (4.1)$$

Equation 4.1 is analogous to the one-dimensional straight ahead transport discussed in Chapter 2, namely:

$$\begin{aligned} \frac{\partial \psi(s, E)}{\partial s} &= \int \Sigma(E' \rightarrow E) dE' \psi(s, E') - \Sigma(E) \psi(s, E) \\ \Sigma(E' \rightarrow E) dE' &= \Sigma(E', Q) dQ \end{aligned} \quad (4.2)$$

Based on the assumptions made by Landau, the energy-loss within the step-size is small enough that the energy over the step is considered to be held constant:

$$\Sigma(E', Q) dQ \approx \Sigma(E_0, Q) dQ$$

which means that,

$$\Sigma(E') \approx \Sigma(E_0)$$

Equation 4.2 becomes,

$$\frac{\partial \psi(s, E)}{\partial s} = \int \Sigma(E_0, Q) [\psi(s, E') - \psi(s, E)] dE'. \quad (4.3)$$

Now in order to connect Landau with the straight ahead transport, we note that $\epsilon = Q$, $\Delta = E_0 - E$, and $E' = E + Q$. Substituting these variables into Equation 4.3 and inputting the bounds of the integral defined in Chapter 2 gives the following:

$$\int_{Q_{min}}^{E_0/2} \Sigma(E_0, Q) [\psi(s, E_0 - \Delta + \epsilon) - \psi(s, E_0 - \Delta)] dQ. \quad (4.4)$$

The final step will be to redefine the ψ 's as:

$$\psi(s, E') = \psi(s, E_0 - \Delta + \epsilon) = \psi(s, -(\Delta - \epsilon - E_0)) \equiv f(x, \Delta - \epsilon) \quad (4.5)$$

$$\psi(s, E) = \psi(s, E_0 - \Delta) = \psi(s, -(\Delta - E_0)) \equiv f(x, \Delta). \quad (4.6)$$

Chapter 4. Landau Theory

Finally substituting $\omega(\epsilon)d\epsilon$ for $\Sigma(E_0, Q)dQ$ we obtain Landau's straggling equation:

$$\frac{\partial f}{\partial x} = \int_0^\infty \omega(\epsilon) [f(x, \Delta - \epsilon) - f(x, \Delta)] d\epsilon \quad (4.7)$$

Clearly, the basis of Landau's distribution comes exactly from the transport equation in which this thesis is attempting to solve. The significance of this relationship shows the subsequent derivation is to the exact transport problem in question.

Carrying on, it is important to note that Landau further allowed the mean energy transfer to be unbounded to facilitate a solution by Laplace transforms. We define the Laplace transform:

$$\varphi(p, x) = \int_0^\infty f(\Delta)e^{-p\Delta}d\Delta, \quad (4.8)$$

and the inverse Laplace transform:

$$f(x, \Delta) = \frac{1}{2\pi i} \int_{-i\infty+\sigma}^{+i\infty+\sigma} e^{p\Delta}\varphi(p, x)dp. \quad (4.9)$$

where the integration path is the Bromwich Contour, with the real part σ is chosen so that all singularities of φ are to the right of it. Going back to Equation 4.1 and multiplying both sides by $e^{-p\Delta}$ and integrating with respect to $d\Delta$ gives:

$$\begin{aligned} \frac{\partial \varphi}{\partial x} &= \int_0^\infty e^{-p\Delta}d\Delta \int_0^\infty \omega(\epsilon)f(x, \Delta - \epsilon)d\epsilon - \int_0^\infty e^{-p\Delta}d\Delta \int_0^\infty \omega(\epsilon)f(x, \Delta)d\epsilon \\ &= \int_0^\infty \omega(\epsilon)d\epsilon \int_0^\infty e^{-p\Delta}f(x, \Delta - \epsilon)d\Delta - \int_0^\infty \omega(\epsilon)d\epsilon \int_0^\infty e^{-p\Delta}f(x, \Delta)d\Delta \\ &= \int_0^\infty \omega(\epsilon)d\epsilon \int_0^\infty e^{-p\Delta}f(x, \Delta - \epsilon)d\Delta - \int_0^\infty \omega(\epsilon)d\epsilon\varphi(p, x) \end{aligned} \quad (4.10)$$

In order to carry out the integration in the first term on the right side of Equation 4.10, a change of variable is made such that $y = \Delta - \epsilon$ yielding:

$$\int_0^\infty \omega(\epsilon)d\epsilon \int_0^\infty e^{-p\Delta}f(x, \Delta - \epsilon)d\Delta = \int_0^\infty \omega(\epsilon)d\epsilon \int_{-\epsilon}^\infty e^{-p(y+\epsilon)}f(x, y)dy. \quad (4.11)$$

Chapter 4. Landau Theory

Landau uses the fact that it is physically impossible for a particle to experience a negative energy-loss nor for the particle to gain energy in a collision. This allows the lower bound to be made such that $f(y) = 0, y < 0$:

$$\int_0^{\infty} \omega(\epsilon) d\epsilon \int_0^{\infty} e^{-p(y+\epsilon)} f(x, y) dy = \varphi(p, x) \int_0^{\infty} \omega(\epsilon) e^{-p\epsilon}. \quad (4.12)$$

Substituting Equation 4.12 into Equation 4.10 and rearranging:

$$\frac{\partial \varphi}{\partial x} = -\varphi(p, x) \int_0^{\infty} \omega(\epsilon) (1 - e^{-p\epsilon}) d\epsilon, \quad (4.13)$$

with boundary condition $\varphi(p, x) = 1$. Equation 4.13 can be readily solved to get:

$$\varphi(p, x) = e^{-x \int_0^{\infty} \omega(\epsilon) (1 - e^{-p\epsilon}) d\epsilon}, \quad (4.14)$$

and substituted into Equation 4.9 to get the spectrum:

$$f(x, \Delta) = \frac{1}{2\pi i} \int_{-i\infty+\sigma}^{+i\infty+\sigma} e^{p\Delta-x \int_0^{\infty} \omega(\epsilon) (1 - e^{-p\epsilon}) d\epsilon} dp. \quad (4.15)$$

Equation 4.15 is the general solution to the energy-loss straggling distribution f in terms of the differential cross section $\omega(\epsilon) \equiv \Sigma(E_0, Q)$. In order to apply this formula the function $\omega(\epsilon)$ must be defined, yet Landau shows that full knowledge of this function is not necessary. He begins by evaluating the term within the exponential of Equation 4.15 making the following assumptions:

- let ϵ_0 be the ionization energy of electron
- let ϵ_{max} be the maximum energy transferred
- only allow values of p such that

$$p\epsilon_{max} \gg 1, \quad p\epsilon_0 \ll 1. \quad (4.16)$$

Chapter 4. Landau Theory

Next, the integral term in the exponential part of Equation 4.15 is split by a value of ϵ_1 where $\epsilon_1 \gg \epsilon_0$ and $p\epsilon_1 \ll 1$. Since the $p\epsilon_1 \ll 1$ the approximation $e^{-p\epsilon} \cong 1 - p\epsilon$ can be made in the integral from 0 to ϵ_1 to get:

$$\begin{aligned} \int_0^{\infty} \omega(\epsilon)(1 - e^{-p\epsilon})d\epsilon &= \int_0^{\epsilon_1} \omega(\epsilon)(1 - (1 - p\epsilon))d\epsilon + \int_{\epsilon_1}^{\infty} \omega(\epsilon)(1 - e^{-p\epsilon})d\epsilon \\ &= p \int_0^{\epsilon_1} \epsilon\omega(\epsilon)d\epsilon + \int_{\epsilon_1}^{\infty} \omega(\epsilon)(1 - e^{-p\epsilon})d\epsilon \end{aligned} \quad (4.17)$$

For the conditions $\epsilon_1 \ll \epsilon$ the Rutherford differential cross section (Eq. 2.5) can be used. Substituting $\frac{K}{\beta^2} \frac{1}{\epsilon^2}$ for $\omega(\epsilon)$ and evaluating the first integral term in Equation 4.17 results in the stopping power (recalling the 1st energy-loss moment defined in Section 2.4.1)[8]:

$$\int_{\epsilon'}^{\epsilon_1} \epsilon\omega(\epsilon)d\epsilon = \frac{K}{\beta^2} \ln \frac{\epsilon_1}{\epsilon'}, \quad \ln \epsilon' = \ln \frac{\left(1 - \frac{v^2}{c^2}\right) I^2}{2mv^2} + \frac{v^2}{c^2} \quad (4.18)$$

Substituting the Rutherford differential cross section for $\omega(\epsilon)$ in the second integral of Equation 4.17 gives:

$$\int_{\epsilon_1}^{\infty} \frac{(1 - e^{-p\epsilon})}{\epsilon^2} d\epsilon = \int_{\epsilon_1}^{\infty} (1 - e^{-p\epsilon}) d\left(\frac{-1}{\epsilon}\right), \quad \frac{d\epsilon}{\epsilon^2} = d\left(\frac{-1}{\epsilon}\right) \quad (4.19)$$

$$\begin{aligned} &= \left[-\frac{1}{\epsilon} (1 - e^{-p\epsilon}) \right] \Big|_{\epsilon_1}^{\infty} + p \int_{\epsilon_1}^{\infty} \frac{e^{-p\epsilon}}{\epsilon} d\epsilon \\ &= \frac{1}{\epsilon_1} (1 - e^{-p\epsilon_1}) + p \int_{\epsilon_1}^{\infty} \frac{e^{-p\epsilon}}{\epsilon} d\epsilon \end{aligned} \quad (4.20)$$

$$= p + p \int_{\epsilon_1}^{\infty} \frac{e^{-p\epsilon}}{\epsilon} d\epsilon \quad , \quad \frac{1}{\epsilon_1} (1 - 1 + p\epsilon_1) + \mathcal{O}(p\epsilon_1)^2 \approx p \quad (4.21)$$

and now,

$$\frac{1}{p} \int_{\epsilon_1}^{\infty} \frac{(1 - e^{-p\epsilon})}{\epsilon^2} d\epsilon = 1 + \int_{\epsilon_1 p}^{\infty} \frac{e^{-z}}{z} dz \quad , \quad z = p\epsilon \quad (4.22)$$

Chapter 4. Landau Theory

Another assumption made by Landau allows for a clever change of bounds. From Equation 4.22 Landau splits the integration at 1, adds and subtracts a definite integral $\int \frac{dz}{z}$ from ϵ_1 to 1 and combines the negative value of the added term to the respective integral in Equation 4.22. Once these two terms are combined he makes the assumption that $\epsilon_1 p$ does not significantly contribute to the integral and replaces the lower bound with 0 yielding:

$$\begin{aligned}
 & 1 + \int_{\epsilon_1 p}^{\infty} \frac{e^{-z}}{z} dz \\
 &= 1 + \int_{\epsilon_1 p}^1 \frac{dz}{z} - \int_{\epsilon_1 p}^1 \frac{dz}{z} + \int_{\epsilon_1 p}^1 \frac{e^{-z}}{z} dz + \int_1^{\infty} \frac{e^{-z}}{z} dz
 \end{aligned} \tag{4.23}$$

$$= 1 + \int_{\epsilon_1 p}^1 \frac{dz}{z} + \int_{\epsilon_1 p}^1 \frac{e^{-z} - 1}{z} dz + \int_1^{\infty} \frac{e^{-z}}{z} dz \tag{4.24}$$

$$= 1 + \int_{\epsilon_1 p}^1 \frac{dz}{z} + \int_0^1 \frac{e^{-z} - 1}{z} dz + \int_1^{\infty} \frac{e^{-z}}{z} dz \tag{4.25}$$

The sum of the two latter integrals is equal to $-C$ where C is equal to Euler's constant, finally Equation 4.21 becomes:

$$\int_{\epsilon_1}^{\infty} \frac{(1 - e^{-p\epsilon})}{\epsilon^2} d\epsilon = p(1 - C - \ln p\epsilon_1). \tag{4.26}$$

Now we can combine Equations 4.18 and 4.26 to obtain for the exponent in Equation 4.15:

$$x \int_0^{\infty} \omega(\epsilon)(1 - e^{-p\epsilon}) d\epsilon = \xi p(1 - C - \ln p\epsilon'), \quad \xi = x \frac{K}{\beta^2}. \tag{4.27}$$

and hence:

$$f(x, \Delta) = \frac{1}{2\pi i} \int_{\Gamma} e^{p\Delta - \xi p(1 - C - \ln p\epsilon')} dp. \tag{4.28}$$

Chapter 4. Landau Theory

Now substituting $u = \xi p$, $dp = \frac{du}{\xi}$ gives:

$$f(x, \Delta) = \frac{1}{2\pi i} \int_{\Gamma'} e^{u\frac{\Delta}{\xi} - u(1-C - \ln(\frac{u\epsilon'}{\xi}))} \frac{1}{\xi} du. \quad (4.29)$$

The exponent in Equation 4.29 can be further simplified:

$$\begin{aligned} & u\frac{\Delta}{\xi} - u \left(1 - C - \ln \left(\frac{u\epsilon'}{\xi} \right) \right) \\ &= u\frac{\Delta}{\xi} - u \left(1 - C - \left(\ln u + \ln \frac{\epsilon'}{\xi} \right) \right) \\ &= u\frac{\Delta}{\xi} - u(1 - C) + u \ln u - u \ln \frac{\epsilon'}{\xi} \\ &= u \ln u + u \left[\frac{\Delta}{\xi} - (1 - C) + \ln \frac{\xi}{\epsilon'} \right]. \end{aligned} \quad (4.30)$$

The term in brackets found in Equation 4.30 will now be redefined to a single variable λ :

$$\lambda = \frac{\Delta - \xi \left(\ln \frac{\xi}{\epsilon'} + 1 - C \right)}{\xi}, \quad (4.31)$$

and the function $f(x, \Delta)$ can be rewritten as:

$$f(x, \Delta) = \frac{1}{\xi} \varphi(\lambda), \quad (4.32)$$

where $\varphi(\lambda)$ is defined by:

$$\varphi(\lambda) = \frac{1}{2\pi i} \int_{-i\infty+\sigma}^{+i\infty+\sigma} e^{u \ln u + \lambda u} du. \quad (4.33)$$

Equation 4.32 now becomes a non-dimensional, single variable equation. It was found[13] that the maximum value of this function is at $\lambda = -0.05$ and therefore the most probable energy-loss is given by the expression:

$$\Delta_0 = \xi \left(\ln \frac{\xi}{\epsilon'} + 0.37 \right). \quad (4.34)$$

Using this value, the definition of the probability of an energy-loss lying between Δ and $\Delta + d\Delta$ is:

$$f(x, \Delta)d\Delta = \varphi \left(\frac{\Delta - \Delta_0}{\xi} \right) d \left(\frac{\Delta - \Delta_0}{\xi} \right) \quad (4.35)$$

Chapter 4. Landau Theory

The validity of this result comes straight from Equation 4.16 and the integral variable $u = \xi p$ for:

$$\xi \gg \epsilon \quad , \quad \xi \ll \epsilon_{max} \quad (4.36)$$

The first condition in Equations 4.36 requires that energy-losses must be sufficiently large in comparison with the atomic energies of the particle, while the second condition requires that the energy-loss must be sufficiently smaller than $\epsilon_{max} = E_0$.

Following Equations 4.35, Landau evaluates the integral in order to obtain an asymptotic formula for the function $\varphi(\lambda)$ at large values of λ . A more concise evaluation of $\varphi(\lambda)$ is done by Börsch-Supan[4] providing limits on the numerical evaluation of λ .

In order to obtain the approximation for large values of λ , Landau had to transform the path of integration as to avoid singularities around the origin[13]. The asymptotic evaluation for large negative λ is shown[4] to have a negligible value for $\lambda < -4$, while the asymptotic evaluation of large positive $\lambda > 100$ tend to the following equation:

$$\varphi(\lambda) \approx \frac{1}{w^2 + \pi^2}, \quad \text{where } \lambda = w + \ln w + B, \quad (4.37)$$

where w is an integral approximation made by Börsch-Supan [4] and $B = \gamma - \frac{1}{2}$. Tabulation of the function $\varphi(\lambda)$ was done[4] for $-4 \leq \lambda \leq 100$. Further work by Blunck & Westphal[3] and Chechin & Ermilova[7] provide a correction to increase the accuracy of straggling within Landau's energy-loss routine.

Chapter 5

Implementation of the Landau Straggling Distribution

Implementation of the Landau energy-loss distribution has been applied most prominently in the ETRAN code[21]. ETRAN is the basis for modern codes, such as MCNP[23] and ITS[11], that model electron and positron transport. These codes begin the transport of charged particles by first declaring a step-size to arbitrarily move the particle, then sample an energy-loss from the Landau distribution. This process is repeated after each step until the particle has lost all energy or reached a boundary.

The following subsections map the variables from Landau's[13] derivation to those used in MCNP[23] as well as describe the programming logic involved in sampling the energy-loss of a particle.

5.1 Electron Steps and Substeps

The condensed random walk of electrons and positrons depends on the energy and the material in which it is moving. The step size s_n is computed by the stopping power $-dE/ds$ of the medium and taken as the average energy-loss over that step where:

$$E_{n-1} - E_n = - \int_{s_{n-1}}^{s_n} \frac{dE}{ds} ds \quad (5.1)$$

and the difference in energy is chosen such that:

$$\frac{E_n}{E_{n-1}} = 2^{-\frac{1}{k}}. \quad (5.2)$$

The most accepted value of k is 8 [21], which results in an average energy-loss of 8.3% and an average energy-loss of half the initial energy after 8 steps. The distance $s = s_n - s_{n-1}$ is defined as an *electron energy step*(Estep) or major step. However, representing the particle's trajectory over smaller steps results in a more accurate model and therefore minor steps or substeps m are introduced resulting in a path length of s/m .

5.2 Continuous Slowing Down Approximation for Landau

The stopping power used in the Landau energy-loss function is given by Berger[1] and is based on the Bethe theory or the continuous slowing down approximation (CSDA) and is computed analytically. This stopping power does not make use of the restricted stopping powers, only the total energy-loss to collisions. Only the range of half the incident energy down to zero is considered (due to indistinguishability of incident

Chapter 5. Implementation of the Landau Straggling Distribution

and recoiling electrons) and the following supplementary constants are defined:

$$\begin{aligned}C2 &= \ln(2I^2) \\C3 &= 1 - \ln(2) \\C4 &= \frac{1}{8} + \ln(2) \\C5 &= \frac{10^{24}\alpha^2 h^2 c^2}{2\pi m c^2 \beta^2}\end{aligned}$$

so that the stopping power becomes:

$$-\left(\frac{dE}{ds}\right) = Z C5 \left\{ \ln [\tau^2(\tau + 2)] - C2 + C3 - \beta^2 + C4 \left(\frac{\tau}{\tau + 1}\right)^2 - \delta \right\} \quad (5.3)$$

This is the collisional energy-loss rate in $[MeV * barns]$. The value I and τ are the ionization potential and incident energy in rest mass units, δ is the density correction term and $\beta = v/c$. The term α represents the fine structure constant defined as:

$$\alpha = \frac{2\pi e^2}{hc} \quad (5.4)$$

where h is Plank's constant, c is the speed of light and e is the electron charge.

Table 5.1 provides the values for the CSDA values for specific energies for electrons in gold.

Continuous Slowing Down Approximation	
Energy (MeV)	CSDA ($\frac{MeV}{cm}$)
20	27.466149
15	26.454245
10	25.044129
5	22.730187
2	20.214680
1	19.407789
0.75	19.605981
0.50	20.715516
0.10	53.299391

Table 5.1: Continuous slowing down approximation for electrons in gold as computed by MCNP5

5.3 Numerical Evaluation of the Landau Energy-Loss Distribution

Most of the numerical work has been done by Börsch-Supan[4], and relevant tables have been made[11] in order to make the sampling and computational evaluation of the distribution efficient. Recall, the probability integral is evaluated such that the maximum individual energy transfer is allowed to extend to ∞ , therefore an upper bound must be imposed in order to preserve the mean energy-loss $\bar{\Delta} = -\frac{dE}{ds}s$. Instead of using Equations 4.34 and 4.32 the Landau variable is re-written[21]:

$$\lambda = \frac{\Delta - \bar{\Delta}}{\xi} + \nu^{\pm} \quad (5.5)$$

where for electrons:

$$\nu^{-} = \ln \frac{T}{\xi} - 0.80907 + \frac{\tau^2 - (2\tau + 1) \ln 2}{(\tau + 1)^2}, \quad (5.6)$$

and for positrons:

$$\nu^{+} = \ln \frac{T}{\xi} - 0.422784 - \frac{\beta^2}{12} \left[11 + \frac{14}{\tau + 2} + \frac{10}{(\tau + 2)^2} + \frac{4}{(\tau + 2)^3} \right], \quad (5.7)$$

Chapter 5. Implementation of the Landau Straggling Distribution

where T is the energy of the particle. The upper bound, λ_{cut} , is chosen such that the mean lambda $\bar{\lambda} = \nu^{\pm}$.

Finally, an extension to Landau's result by Blunck-Leisgang[3](σ_{BL}) and a further correction by Chechin and Emilova[7](σ_{CE}) to the variance of the distribution computed by Blunck-Westphal[3], has increased the accuracy of the variance about the mean by convoluting Landau's distribution with a Gaussian distribution. The following equation is added to the Landau result:

$$\sigma = \frac{\sigma_{BW}}{1 + 3\epsilon_{CE}} \quad (5.8)$$

$$\sigma_{BW} = \sqrt{10eV \cdot Z^{\frac{4}{3}} \Delta} \quad (5.9)$$

$$\epsilon_{CE} \approx \left[\frac{10\xi}{I} \left(1 + \frac{\xi}{10I} \right)^3 \right]^{-\frac{1}{2}} \quad (5.10)$$

5.3.1 MCNP5 Computational Sampling of Landau

Now that the step-size, stopping power, and relevant equations have been defined, the manner in which the code samples an energy-loss is discussed. Preset arrays[11] within the code have been computed such that the expected mean $\bar{\lambda}$ calculated by Equations 5.6 or 5.7 corresponds to the exact value of λ_{cut} needed to preserve the mean energy-loss. Another array (`eq1m`) of 5000 equiprobable λ bins have also been precomputed[11], allowing a direct sampling of λ between $[-4, 100]$. The function `strag_landau` from the MCNP source code[23] computes the energy transfer, the following equations employed in the code are mapped to the relevant equations presented in previous sections:

`step`: Equation 5.1

`b_west`: Equation 5.8

`qs_csda`: Equation 5.3

Chapter 5. Implementation of the Landau Straggling Distribution

`typical_max_xfer`: Equation 4.27

`expected_mean_lambda`: Equation 5.6 or 5.7

`blunck_et_al_width`: Equation 5.8

The sequence for sampling an energy-loss is described by the following:

1. Determine(sample) if $\lambda > 100$.
 - If $\lambda > 100$ compute λ analytically (Eq. 4.37), else continue.
2. Sample a random value between $[1, 5000]$ choosing a value of λ from the array `eq1m` based on the sampled value.
 - If $\lambda > \lambda_{cut}$ repeat sampling, else continue.
3. Sample from the Gaussian distribution (Eq 5.8).
4. Convert λ to proper units for the resulting energy-loss.

The following equations map the Landau energy-loss variable(`sp`) (Eq. 4.32) to the sampled deviation from the mean:

$$\Delta = \xi(\lambda - \bar{\lambda}) + \bar{\Delta} \tag{5.11}$$

$$\text{sp} = \text{typical_max_xfer}(\lambda - \text{expected_mean_lambda}) + \text{blunck_et_al_width} \tag{5.12}$$

Once `sp` has been sampled and accepted, it is converted to units of *MeV* and the final energy-loss $Q = (\text{qs_csda} + \text{sp}) \cdot \text{step}$.

5.4 Benchmark Comparison

For purposes of this thesis, the Landau energy-loss routine `strag_landau` is taken from MCNP and employed into a research code. This function is easily implemented as long as the conditions of Equations 4.36 are met for $\epsilon_{min} = I$ and $\epsilon_{max} = Q_{max}$. It is important to note that in the derivation of the integral in Equation 4.18, Landau made an assumption on the cross section $\omega(\epsilon)$. Before this approximation, by definition, this integral was the first moment, i.e. stopping power, of $\omega(\epsilon)$. Therefore, it is possible to input any stopping power value into the function. In order to maintain consistency with the analog benchmark, the stopping power will be changed from Bethe's theory (Section 4.2.2) to the first energy-loss moment of the analog cross section used here (Section 2.4.1), while all other inputs and variables are computed in the same manner and held constant. An equivalent number of particle samples from the analog benchmark solutions are used in the `strag_landau` routine. The same PRNG, computer processor, statistics, and tallies will be used and computed in the research code. Comparisons for both electrons and positrons are presented for all benchmark cases over a single major step-size defined in Chapter 3.

In all the figures presented, it is clear that there is a severe cutoff in the energy-loss spectra for Landau. In the case of the electron benchmarks, there exists a dip in the spectra near half the initial energy. This drop in the spectra accounts for the energy cutoff of all electrons that have collided once due to the $Q_{max} = E_0/2$ limit in a single collision. For example, Figure 5.5 shows a dip around $0.5MeV$ for $E_0 = 1MeV$ then again at $0.75MeV$. This second dip is due to the same reasons above except for the maximum value for a twice collided electron is $Q_{max} = (E_0/2)/2$. In subsequent figures, this characteristic continues for all electron benchmarks. The Landau distribution does not match the dip in the energy-loss spectra for all figures. In Figure 5.5 there is a close match to the Landau cutoff and the analog drop-off for $1MeV$ electrons, yet with increasing energy, a larger difference between this

Chapter 5. Implementation of the Landau Straggling Distribution

characteristic emerges, while for decreasing energies this difference decreases. The same cutoff arises for positrons using Landau, while the positron benchmark does not contain the drop-off seen for electrons. The Bhabha cross section does not suffer indistinguishability issues and $Q_{max} = E_0$. Like the electron spectra, the cutoff for positrons has the same trend with respect to incident energy.

The cutoff seen in Landau is an artifact from the value λ_{cut} chosen by the code in order to preserve the mean energy-loss over the step. In the condensed history “random walk”, the particle is forced to move the major step while maintaining a fixed energy. As a result of these conditions and this abrupt cutoff in the spectra, the possibility of high energy-losses (i.e. energy-losses corresponding to $\lambda > \lambda_{cut}$) are impossible.

Although the tail of our spectra does not agree with the analog benchmarks, the area where more probable energy-losses occur is closely matched. For both electrons and positrons, there is a direct relationship between incident energy and accuracy. With higher energies, there is a higher convergence to the benchmark distribution around the most probable energy-loss. For energies at or below $1MeV$, there is a distinct difference in the Landau spectra produced by gold and water. Gold breaks down at $1MeV$. The peak around the most probable energy-loss is no longer close to the magnitude of the benchmark, nor do the peaks match for the most probable energy-loss. As the incident energy decreases from $1MeV$ for electrons and positrons on gold, the distribution around the peak continues to get worse. Water however, does not have this problem. Although there is slight difference in the most probable energy-loss, the magnitude of particles is nearly exact.

In all figures there is an increase in the $RE_{1\sigma}$ for increasing energy-losses. Although these $RE_{1\sigma}$'s are lower than 5%, it is possible to decrease these errors with more particle samples, yet due to computational time and comparison with Landau, it is sufficient to maintain a $RE_{1\sigma}$ less than 1% in only the areas of comparison. It

Chapter 5. Implementation of the Landau Straggling Distribution

is also important to note that these high $RE_{1\sigma}$ are also caused by an insignificant amount of particles losing high amounts of energy in the system.

Other than spectra, it is difficult to explain the reasoning behind the accuracy of this distribution. The Landau distribution has been proven to match experimental results for high energies[21], yet there does not exist a quantifiable measurement to evaluate the accuracy in the distribution. The next chapter will, by examination of the energy-flux moments, assess the accuracy of Landau's distribution.

Chapter 5. Implementation of the Landau Straggling Distribution

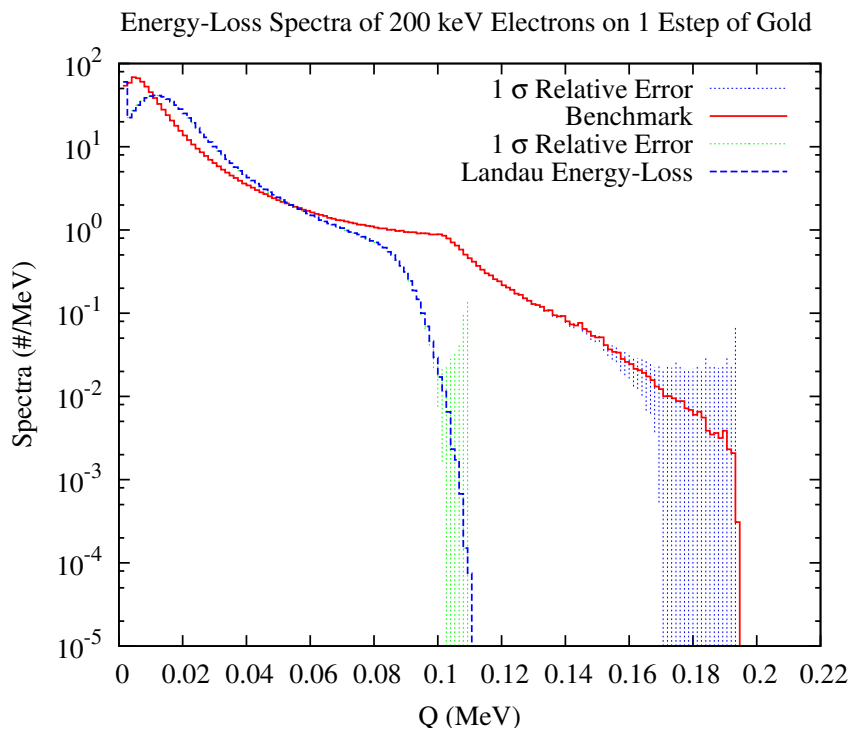


Figure 5.1: Energy-Loss Spectra of 200 *keV* Electrons on $1.16 \times 10^{-3}cm$ of Gold

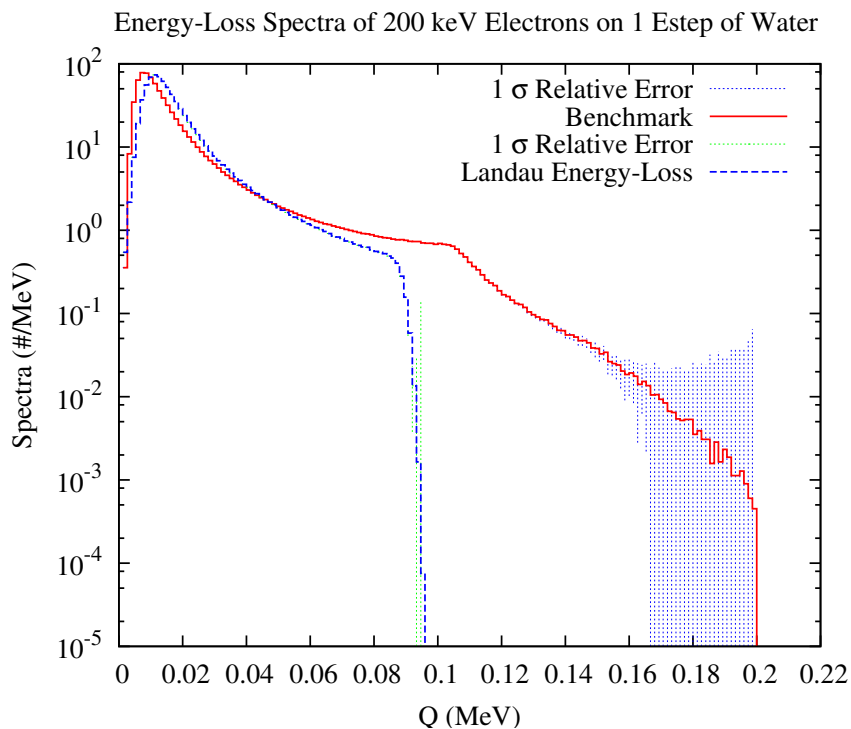


Figure 5.2: Energy-Loss Spectra of 200 *keV* Electrons on $1.25 \times 10^{-2}cm$ of Water

Chapter 5. Implementation of the Landau Straggling Distribution

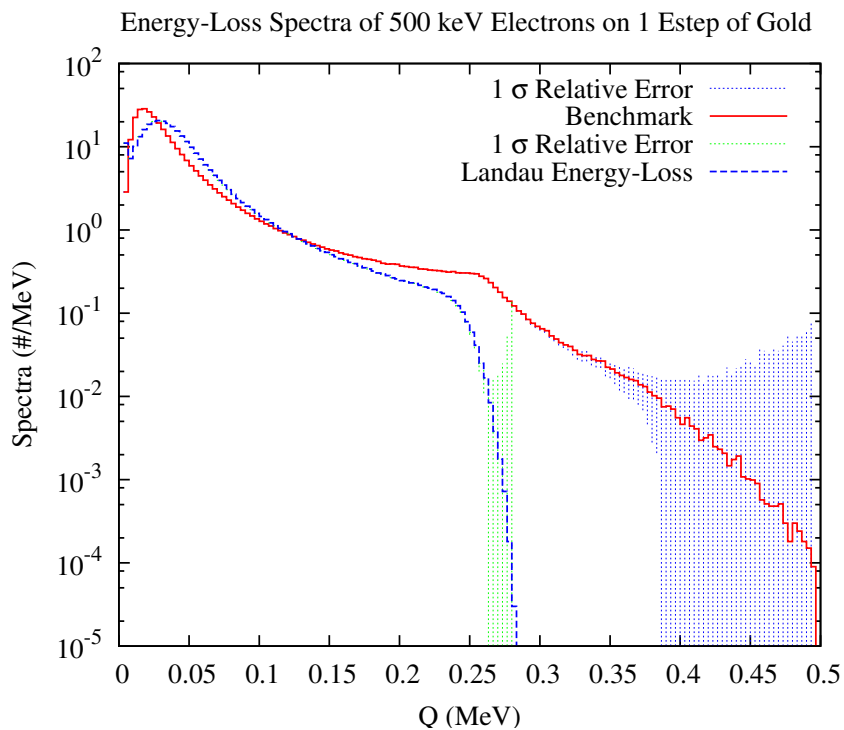


Figure 5.3: Energy-Loss Spectra of 500 keV Electrons on $3.90 \times 10^{-3}cm$ of Gold

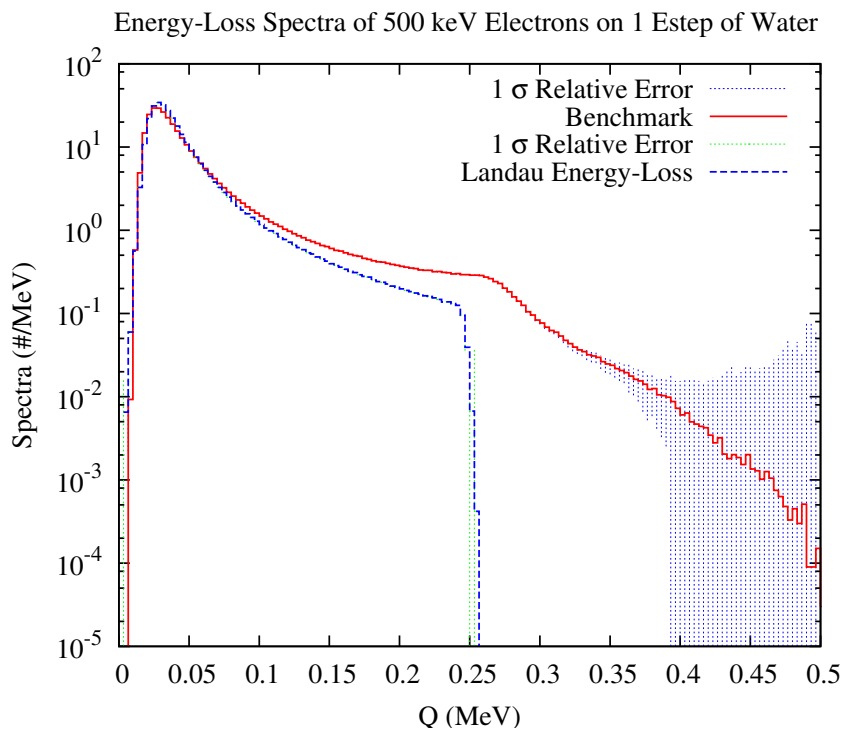


Figure 5.4: Energy-Loss Spectra of 500 keV Electrons on $5.07 \times 10^{-2}cm$ of Water

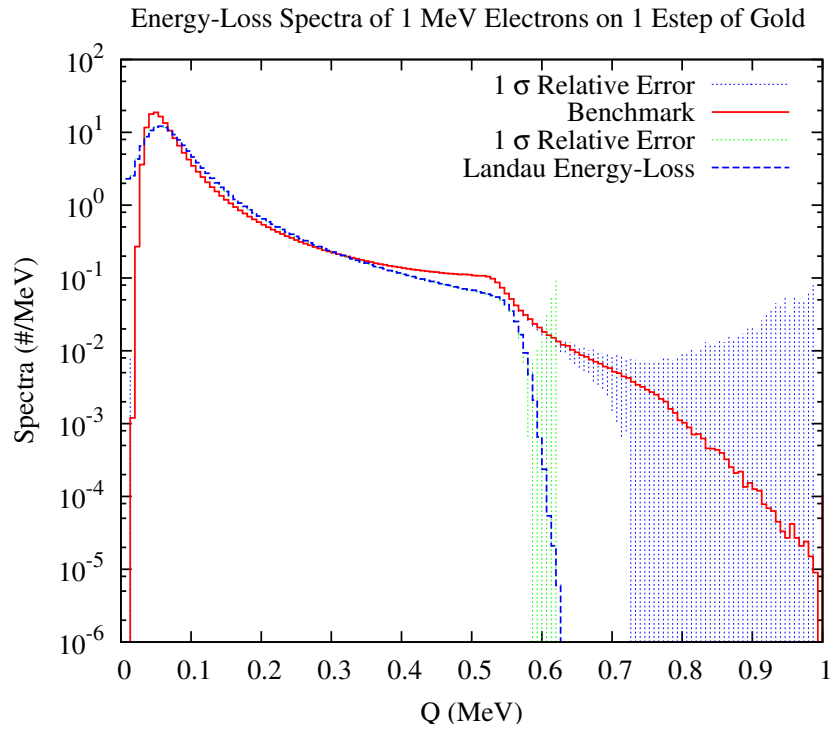


Figure 5.5: Energy-Loss Spectra of 1 MeV Electrons on $8.52 \times 10^{-3} cm$ of Gold

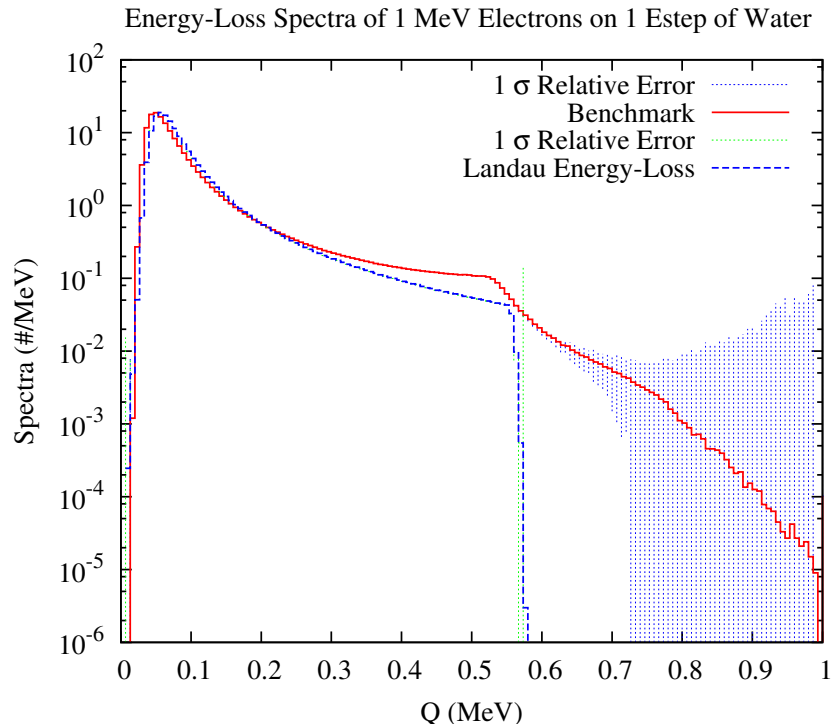


Figure 5.6: Energy-Loss Spectra of 1 MeV Electrons on $9.63 \times 10^{-2} cm$ of Water

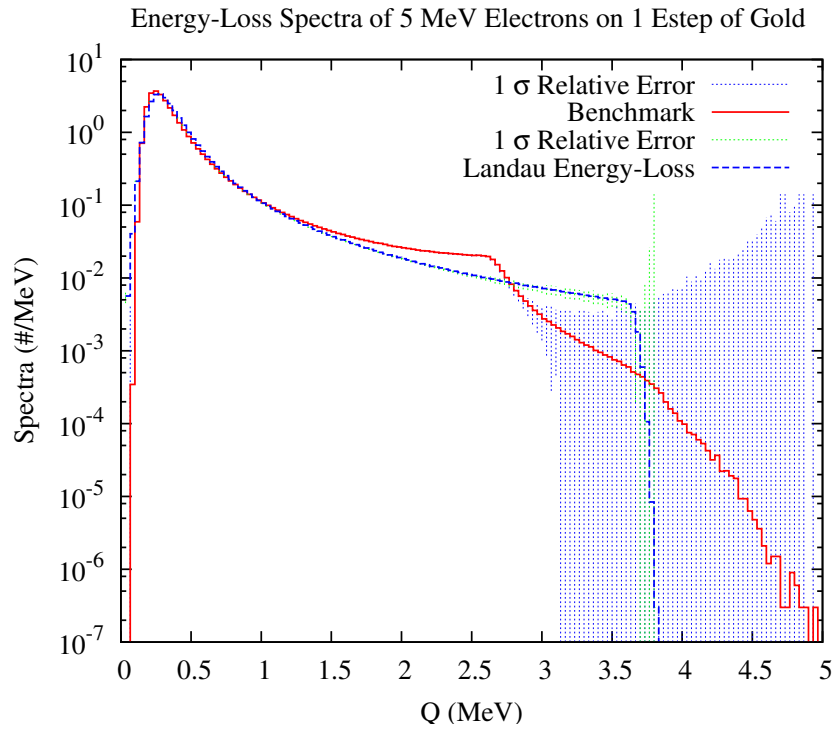


Figure 5.7: Energy-Loss Spectra of 5 MeV Electrons on $3.99 \times 10^{-2} cm$ of Gold

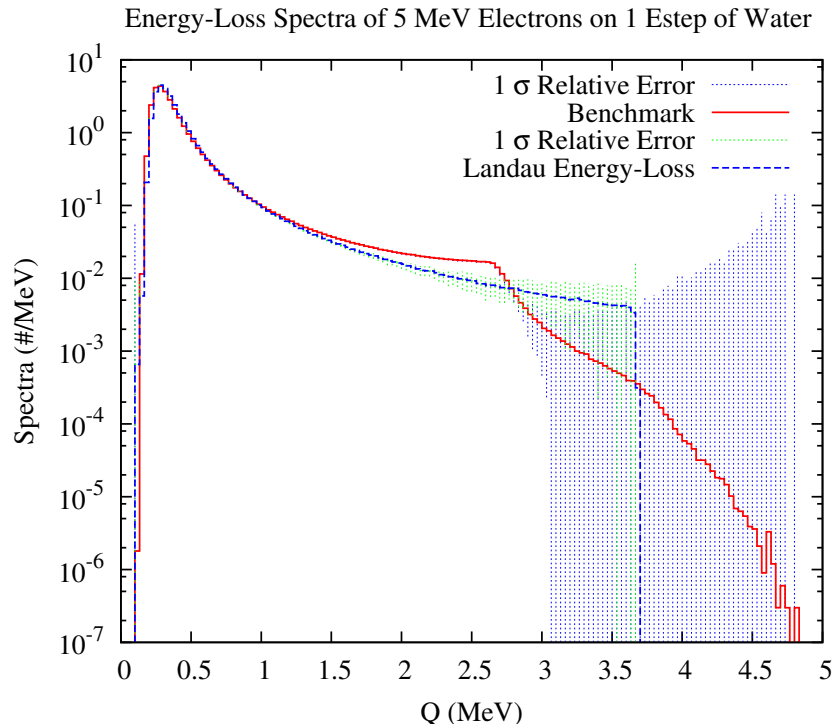


Figure 5.8: Energy-Loss Spectra of 5 MeV Electrons on $4.47 \times 10^{-1} cm$ of Water

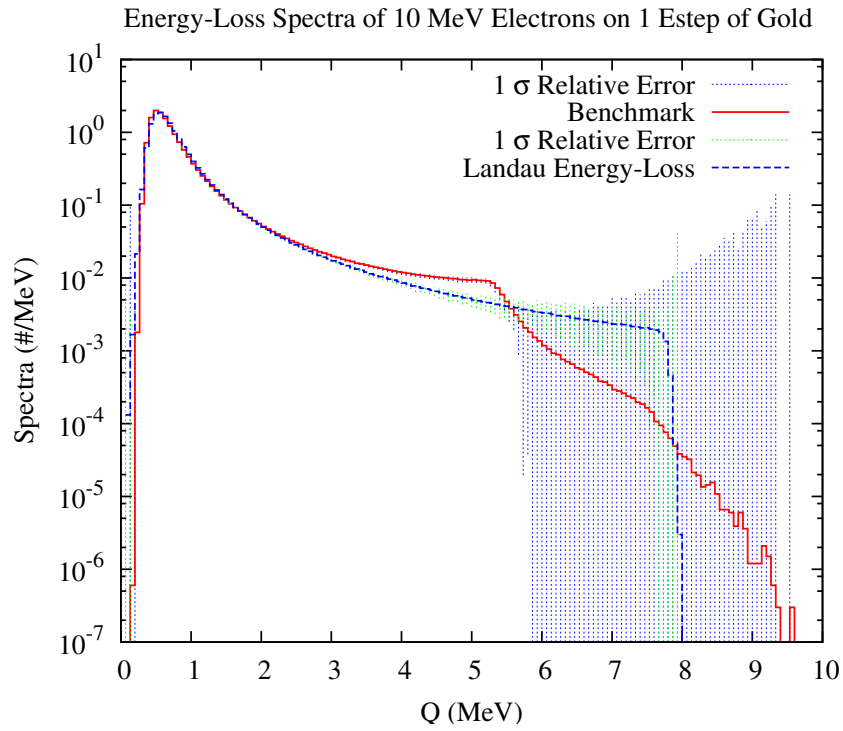


Figure 5.9: Energy-Loss Spectra of 10 *MeV* Electrons on $7.47 \times 10^{-2}cm$ of Gold

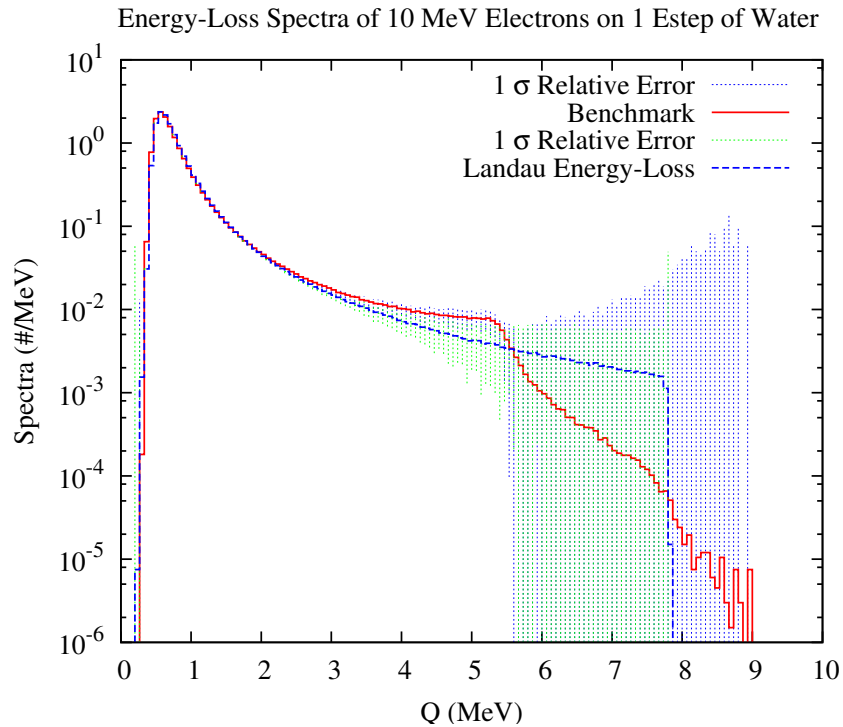


Figure 5.10: Energy-Loss Spectra of 10 *MeV* Electrons on $8.84 \times 10^{-1}cm$ of Water

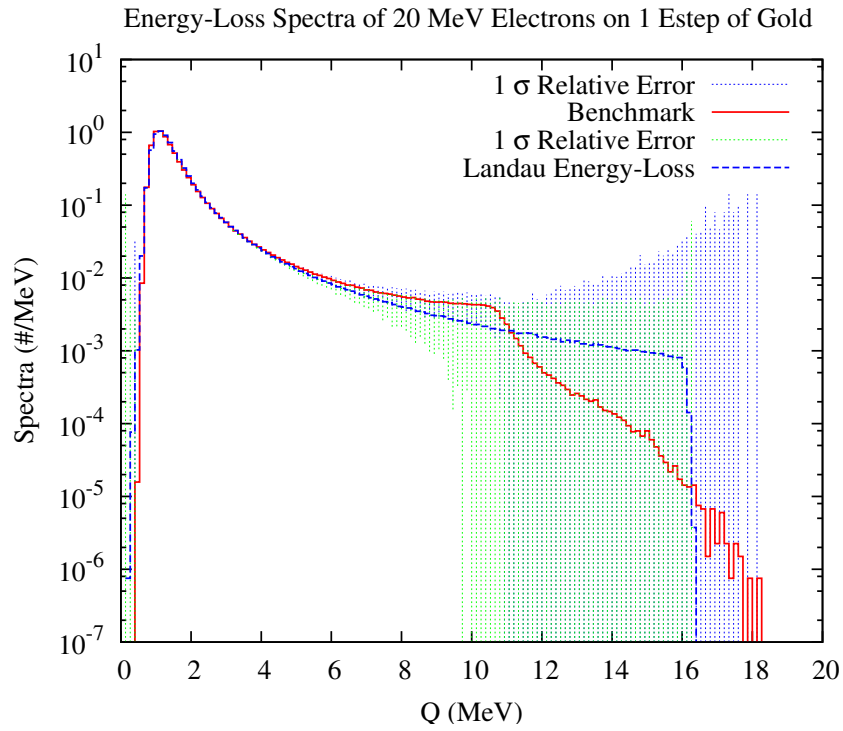


Figure 5.11: Energy-Loss Spectra of 20 MeV Electrons on $1.40 \times 10^{-1} cm$ of Gold

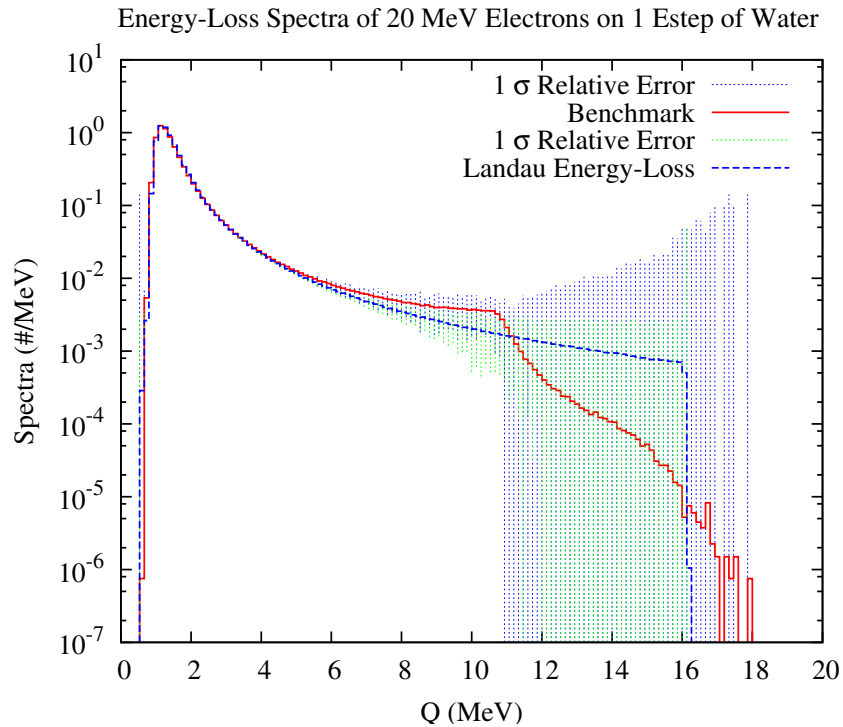


Figure 5.12: Energy-Loss Spectra of 20 MeV Electrons on 1.67cm of Water

Chapter 5. Implementation of the Landau Straggling Distribution

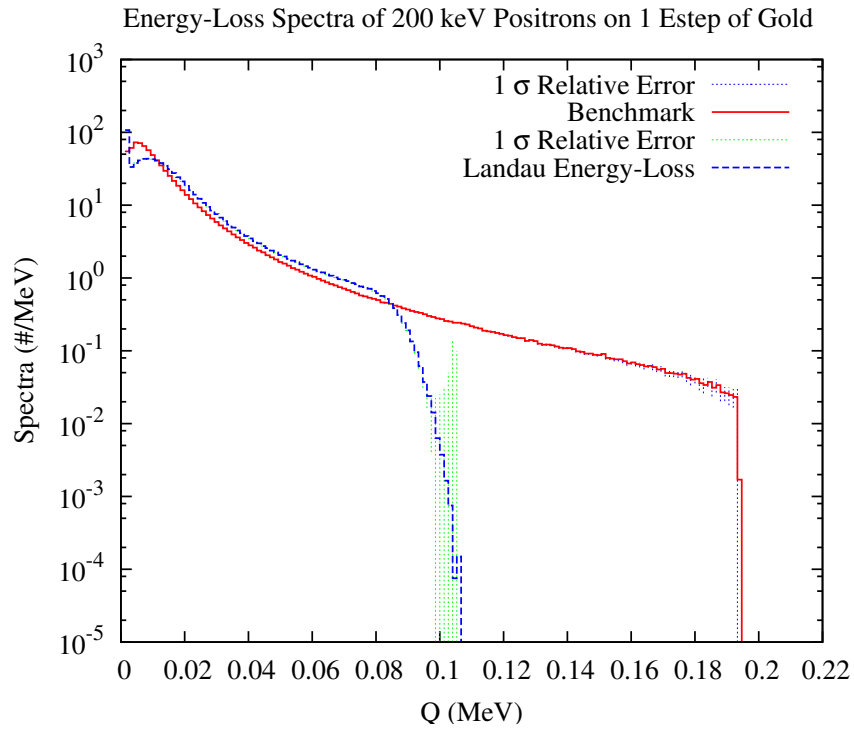


Figure 5.13: Energy-Loss Spectra of 200 keV Positrons on $1.16 \times 10^{-3} \text{ cm}$ of Gold

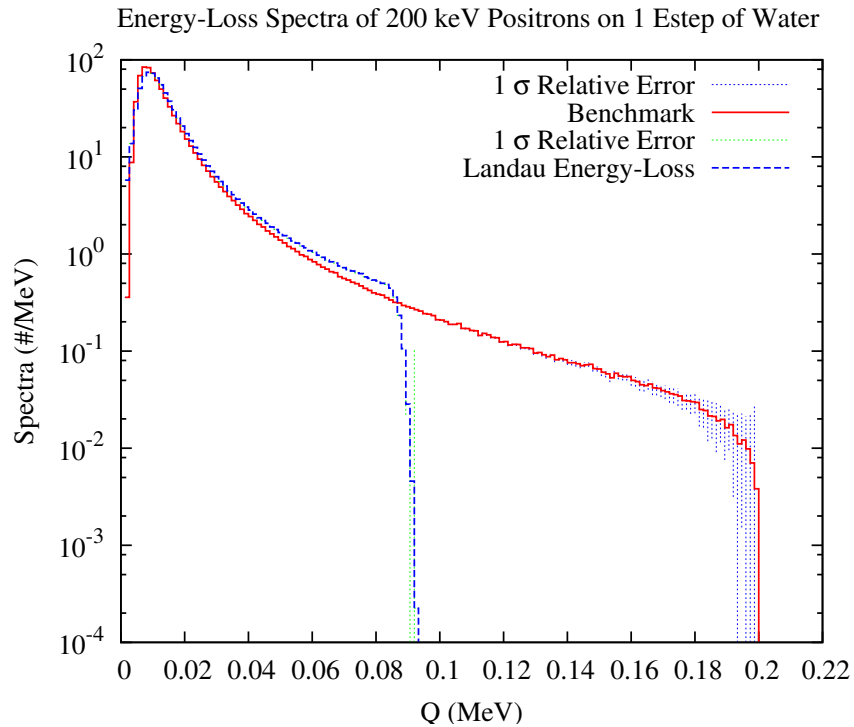


Figure 5.14: Energy-Loss Spectra of 200 keV Positrons on $1.25 \times 10^{-2} \text{ cm}$ of Water

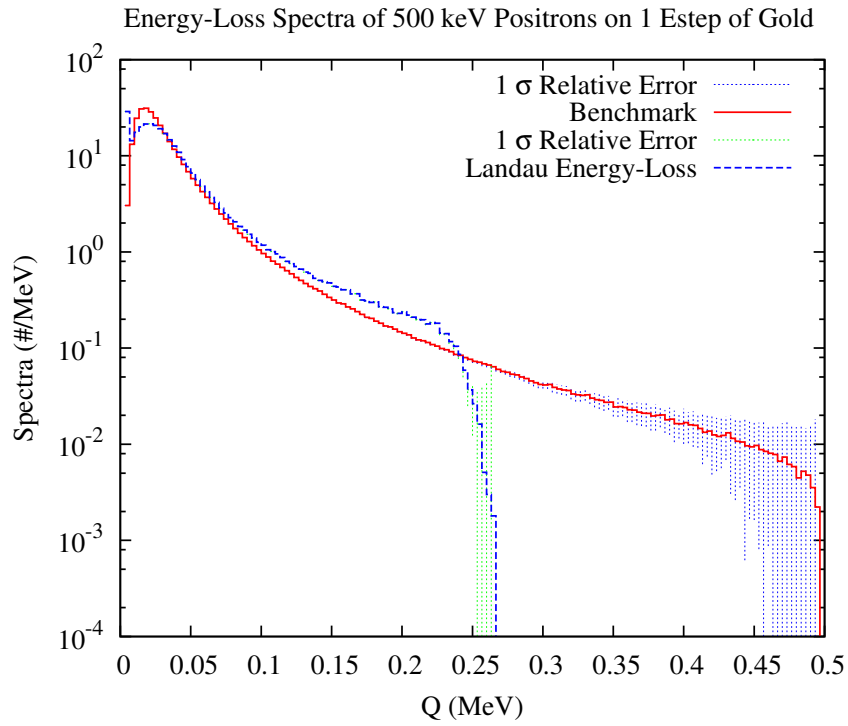


Figure 5.15: Energy-Loss Spectra of 500 keV Positrons on $3.90 \times 10^{-3} \text{ cm}$ of Gold

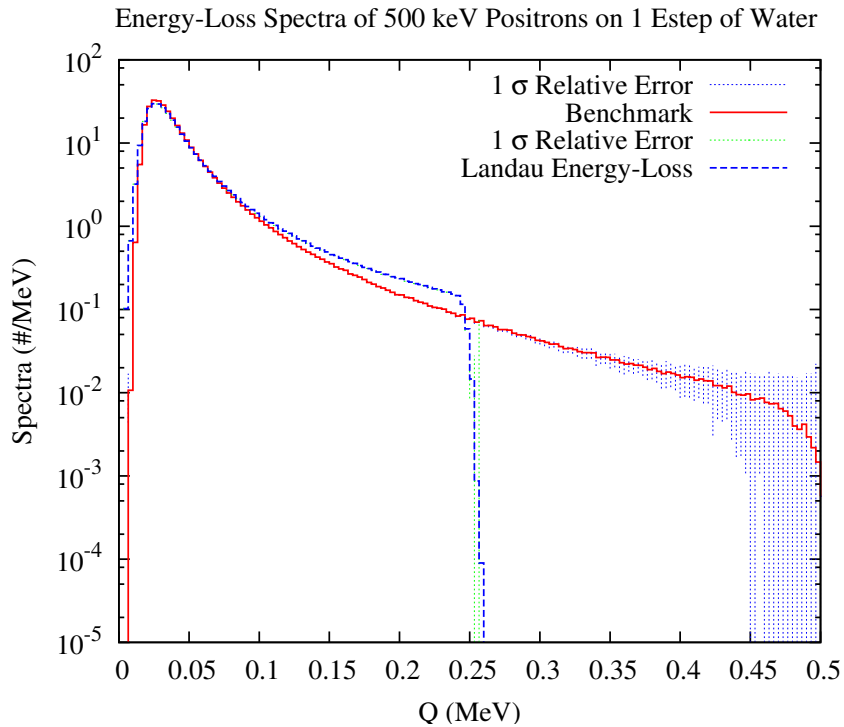


Figure 5.16: Energy-Loss Spectra of 500 keV Positrons on $5.07 \times 10^{-2} \text{ cm}$ of Water

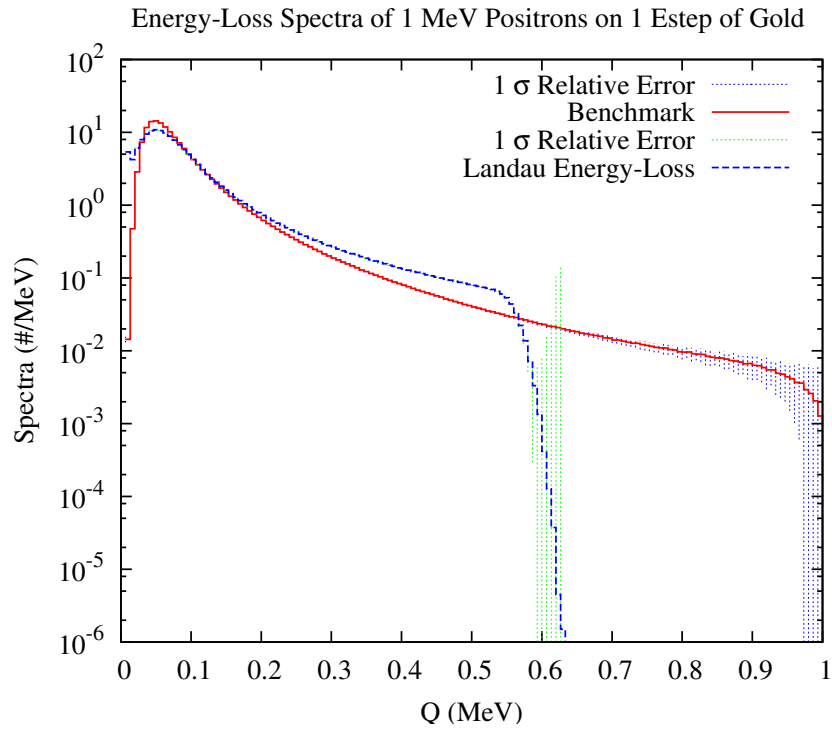


Figure 5.17: Energy-Loss Spectra of 1 MeV Positrons on $8.52 \times 10^{-3} \text{ cm}$ of Gold

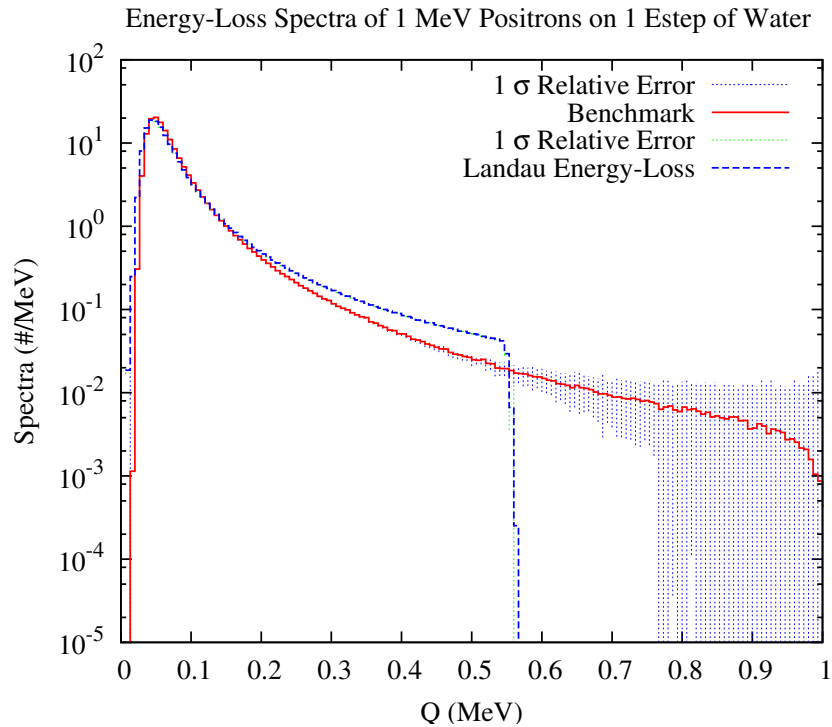


Figure 5.18: Energy-Loss Spectra of 1 MeV Positrons on $9.63 \times 10^{-2} \text{ cm}$ of Water

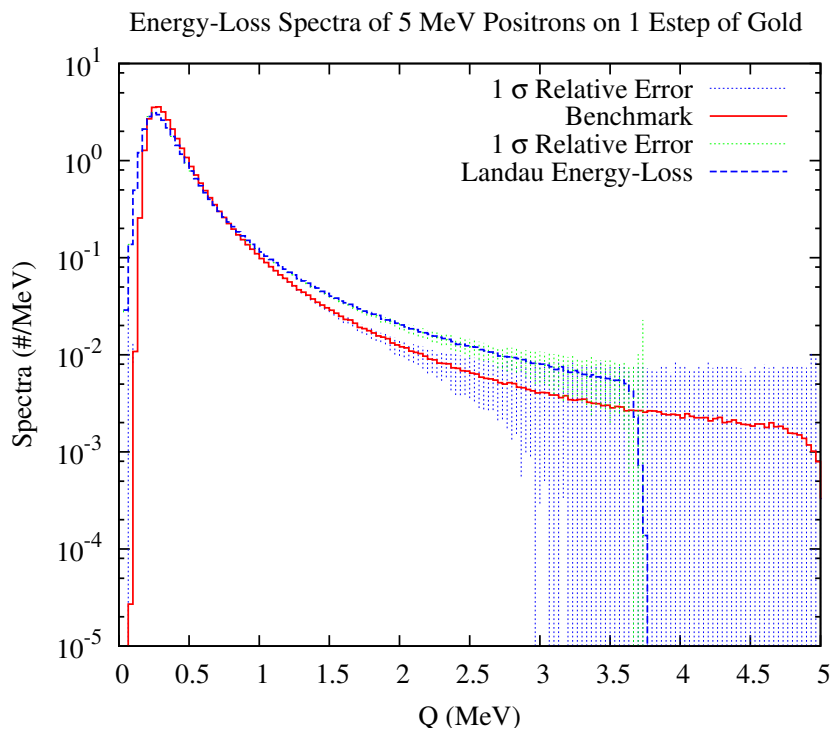


Figure 5.19: Energy-Loss Spectra of 5 MeV Positrons on $3.99 \times 10^{-2} cm$ of Gold

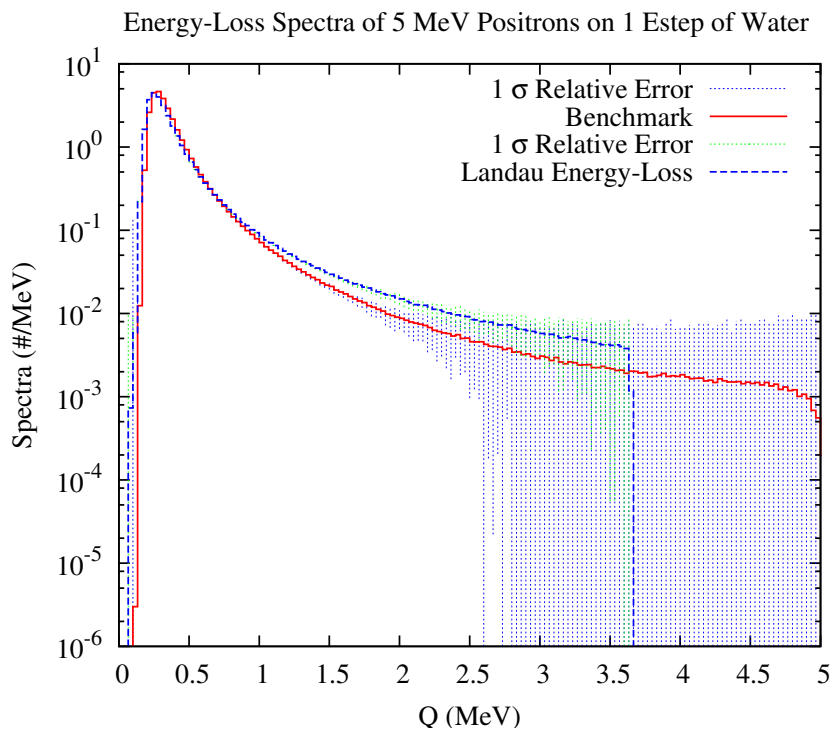


Figure 5.20: Energy-Loss Spectra of 5 MeV Positrons on $4.47 \times 10^{-1} cm$ of Water

Chapter 5. Implementation of the Landau Straggling Distribution

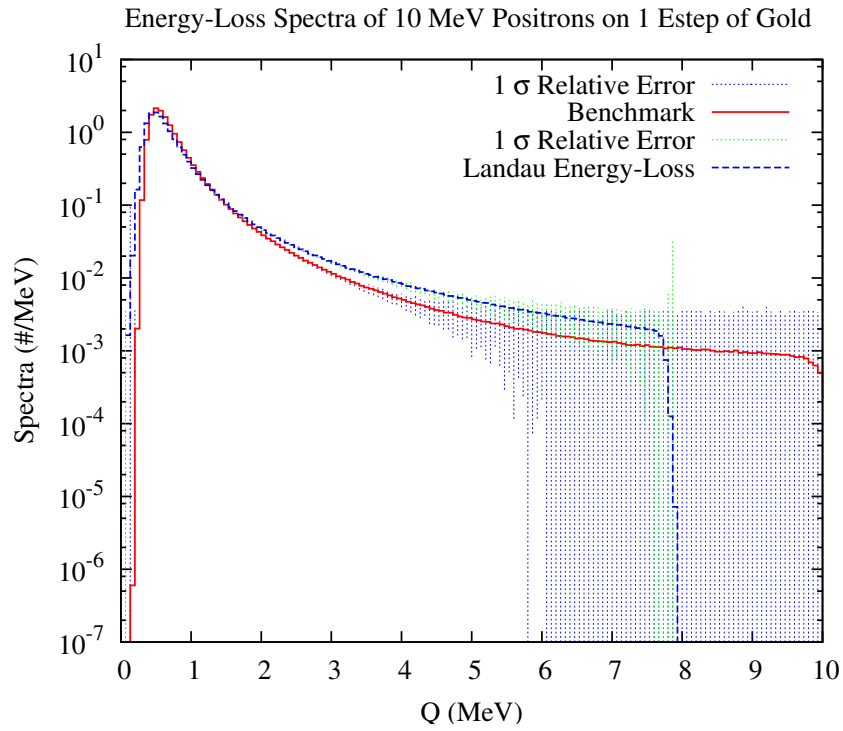


Figure 5.21: Energy-Loss Spectra of 10 MeV Positrons on $7.47 \times 10^{-2} cm$ of Gold

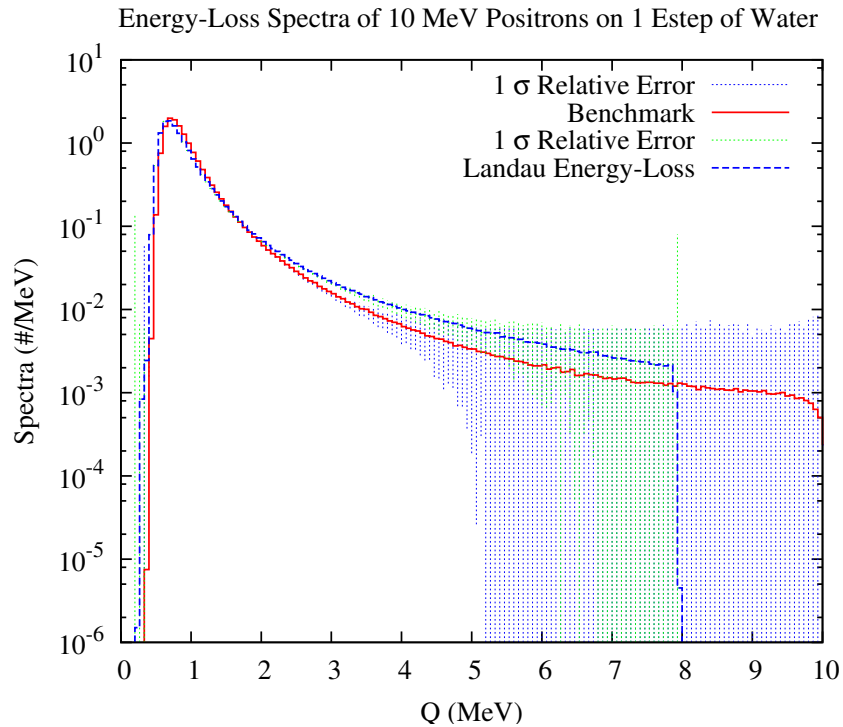


Figure 5.22: Energy-Loss Spectra of 10 MeV Positrons on $8.84 \times 10^{-1} cm$ of Water

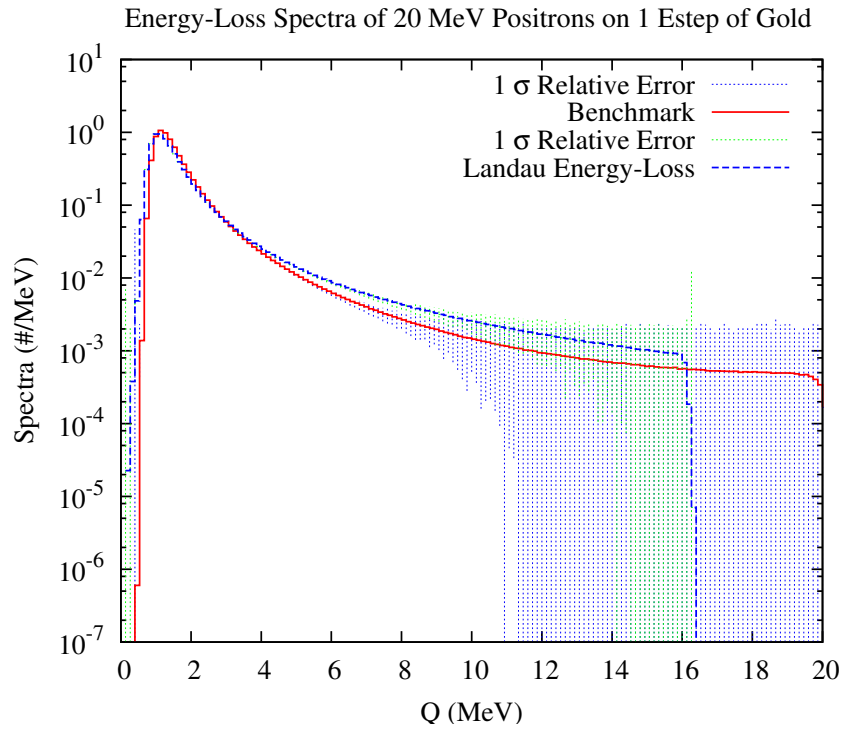


Figure 5.23: Energy-Loss Spectra of 20 MeV Positrons on $1.40 \times 10^{-1} \text{cm}$ of Gold

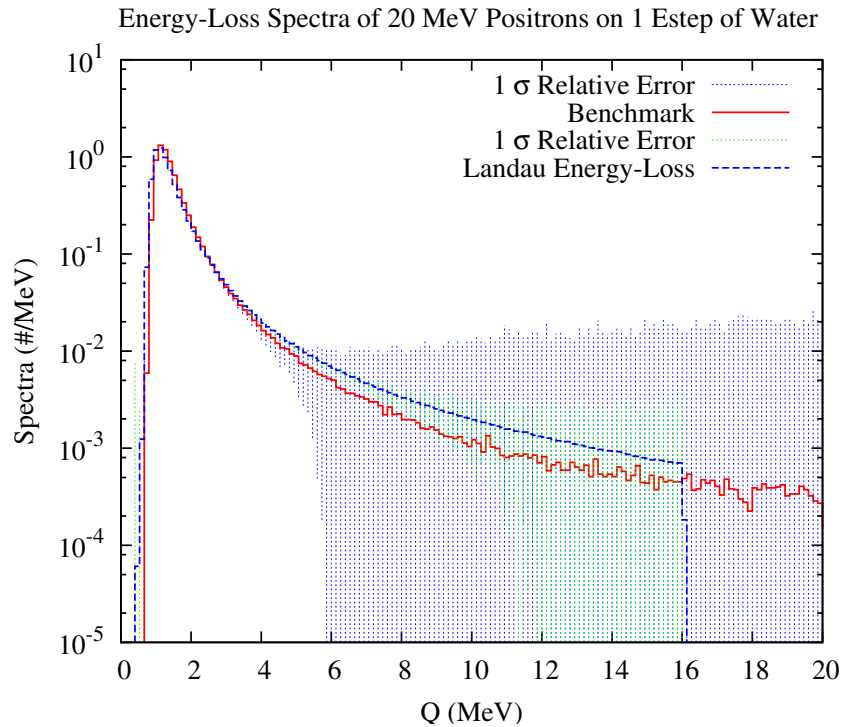


Figure 5.24: Energy-Loss Spectra of 20 MeV Positrons on 1.67cm of Water

Chapter 6

Lewis-type Theory for Moment-Preserving Energy Straggling

The investigation of moment-preserving models in an attempt to solve the transport equation has a long history. Lewis[15] first showed that exact representation of various moments of the spatial and angular distributions resulted in accurate models. In doing such, the small-angle approximations that accompany condensed history multiple-scattering theories are no longer necessary, allowing longer mean free paths and greater efficiency. Franke and Prinja[9] were able to show for energy-loss, low order moment-preservation results in a faster and accurate calculation of dose for electrons, yet artifacts of the discretization resulted in energy-loss spectra of thin targets.

In order to mitigate these artifacts, Harding[12] decomposed the analog cross section into a discrete piece and a continuous piece. By allowing more probable interactions to be represented by discrete moments of the cross section coupled with

less probable interactions represented by the exact analog cross section, these artifacts were removed while maintaining computational efficiency. By representing the less probable energy-losses by the continuous part essentially approximates the higher-order moments to greater accuracy, thus increasing the accuracy of moments and guarantying a more accurate solution.

Inherent in both of these methods is the preservation of specific physical aspects that accompany the cross section of the true analog problem. The accuracy of moment-preserving is directly related to the number of moments preserved. Both Franke and Harding[9, 12] have shown this relationship to be true. The Landau energy-loss distribution, by definition, is constructed to guarantee the mean energy-loss and therefore the first moment of the energy-loss is preserved. Work done by Blunck-Westphal[3] has contributed to the distribution by convoluting a Gaussian distribution about the mean capturing the correct variance about the mean, i.e. second moment. Landau is moment-preserving up to the second energy-loss moment[23]. In terms of the definition of energy-loss moments, it is not possible to quantifiably verify the second moment, nor is it possible to calculate the higher-order energy-loss moments. This calls for a different approach in describing the Landau differential cross section in such a manner that is easily compared to the analog solution. As a result, we will show there exists a direct relationship between the preservation of energy-loss moments and energy-flux moments, which will allow a quantifiable comparison of Landau moments to analog moments.

More specifically, work by Prinja [20] has proven that for thin layers or steps where the mean energy-loss is small compared to the incident energy of the particle, such that the energy-loss moments of the allowable energy range do not vary, then the number of energy-loss moments preserved through order N is identical to the number of energy-flux moments preserved through order N . These constraints are identical to the conditions of validity of the Landau[13] theory presented in Chapter

4, and will allow a measurable comparison of high-order moments.

The motivation now is to establish the conditions under which there exists a direct relationship between the energy-loss moments Q_n and the energy-flux moments I_n . We will begin by recalling the definitions of energy-loss and energy-flux moments:

$$Q_{e^{-},+,n} = \int_{Q_{min}}^{Q_{max}} Q^n \Sigma_{e^{-},+}(E, Q) dQ, \quad (6.1)$$

$$I_{e^{-},+,n}(s) = \int_{E_{min}}^{E_{max}} E^n \psi_{e^{-},+}(s, E) dE. \quad (6.2)$$

Prinja [20] has developed equations for the energy-flux moments by beginning with Equation 2.14, rearranging the incoming and outgoing energy terms and combining the in-scatter and out-scatter terms to yield:

$$\frac{dI_n(s)}{ds} = - \int \psi(s, E) dE \int (E^n - E'^n) \Sigma_e(E \rightarrow E'). \quad (6.3)$$

At this point it is convenient to write the integral over E' in terms of the energy transfer $Q = E - E'$ and introduce a binomial expansion:

$$E'^n = (E - Q)^n = \sum_{m=0}^n (-1)^m \binom{n}{m} Q^m E^{n-m}, \quad (6.4)$$

using the same method for E^n , rewriting $E^n - E'^n$ as a binomial expansion and substituting it into Equation 6.3 gives the following:

$$\frac{dI_n(s)}{ds} = \sum_{m=1}^n c_{nm} \int_0^\infty dE E^{n-m} Q_m(E) \psi(s, E), \quad (6.5)$$

$$c_{nm} = (-1)^m \binom{n}{m}, \quad n = 1, 2, \dots, N \quad (6.6)$$

$$I_n(0) = E_0^n, \quad n = 1, 2, \dots, N$$

Although Equation 6.5 has no value since the flux is unknown, this result does show there is an implicit relationship between the two types of moments. Next, we will

Chapter 6. Lewis-type Theory for Moment-Preserving Energy Straggling

proceed with a second transport equation which differs from the first by changing the differential cross section, and in turn the energy-loss moments. Hatted values will be used to denote the associated variables in the second transport equation yielding:

$$\frac{d\widehat{I}_n(s)}{ds} = \sum_{m=1}^n c_{nm} \int_0^\infty dE E^{n-m} \widehat{Q}_m(E) \widehat{\psi}(s, E), \quad (6.7)$$

$$\widehat{I}_n(0) = E_0^n, \quad n = 1, 2, \dots, N \quad (6.8)$$

giving a new set of energy-loss moments defined by:

$$\widehat{Q}_n(E) = \int_0^\infty Q^n \widehat{\Sigma}_e(E, Q) dQ \quad n = 1, 2, \dots, N \quad . \quad (6.9)$$

Now let the second transport equation be a pseudo-transport problem with identical energy-loss moments to the analog problem up to some fixed order N :

$$\widehat{Q}_n(E) = Q_n(E), \quad n = 1, 2, \dots, N \quad . \quad (6.10)$$

It is clear in the general definition of the energy-flux that $\psi(s, E)$ and $\widehat{\psi}(s, E)$ will differ regardless of any finite number of moments preserved and thus \widehat{I}_n and I_n will not match. Now a constraint is made on the energy-loss moments to hold for a fixed energy at E^* in the range $0 < E^* < E_0$:

$$\widehat{Q}_n(E^*) = Q_n(E^*), \quad n = 1, 2, \dots, N \quad . \quad (6.11)$$

Further more, the assumption is made that energy-loss moments do not differ from their corresponding values at $E = E^*$ over this energy range. Therefore we may write:

$$Q_n(E) = Q_n(E^*), \quad (6.12)$$

$$\widehat{Q}_n(E) = \widehat{Q}_n(E^*), \quad (6.13)$$

$$0 < E, \quad E^* \leq E_0, \quad n = 1, 2, \dots, N.$$

Chapter 6. Lewis-type Theory for Moment-Preserving Energy Straggling

Substituting Equations 6.12 and 6.13 into Equations 6.3 and 6.7 and expressing the integral in terms of the respective energy-flux moments yields:

$$\frac{dI_n(s)}{ds} = \sum_{m=1}^n c_{nm} Q_m(E^*) I_{n-m}(s); \quad I_n(0) = E_0^n, \quad n = 1, 2, \dots \quad (6.14)$$

$$\frac{d\widehat{I}_n(s)}{ds} = \sum_{m=1}^n c_{nm} \widehat{Q}_m(E^*) \widehat{I}_{n-m}(s); \quad \widehat{I}_n(0) = E_0^n, \quad n = 1, 2, \dots \quad (6.15)$$

$$I_0(s) = 1 = \widehat{I}_0(s). \quad (6.16)$$

Equations 6.14 and 6.15 are now linear systems of closed moment equations for $I_n(s)$ and $\widehat{I}_n(s)$ which can be solved for $n \geq 1$. For $1 \leq n \leq N$ when $\widehat{Q}_n(E^*) = Q_n(E^*)$, the equations and initial conditions are identical and their solutions are also identical, which means:

$$\widehat{I}_n(s) = I_n(s), \quad n = 1, 2, \dots, N \quad . \quad (6.17)$$

Finally, the differential energy transfer cross section corresponding to the pseudo-transport problem has the same energy-loss moments as the true analog differential energy transfer cross section through order N , and if these energy-loss moments do not vary over the allowable energy range, then the two transport problems will have identical energy-flux moments through order N . This condition will be met for thin layers or steps where the mean energy-loss is small, and E^* would then be equated to the initial energy E_0 . This is precisely the condition in which Landau's distribution is applied. Therefore Prinja[20] has proven this moment-equivalence result is true for any moment-preserving model within the constraints of Landau straggling theory. However, it is important to note that the converse can not be proven. That is to say that the number of energy-flux moments preserved through order N does not guarantee that the number of energy-loss moments through order N are preserved.

The Landau distribution is inherently first moment-preserving, and has been extended to capture the second moment by Blunck, et. al.[3], but by the definition of energy-loss moments there is no computational way of evaluating Landau's function.

Although experimental comparison of the mean and full-width-half-max give results for the first and second moment, there is still no way of determining higher moments. Through the above equivalence, we now have a way of quantifiably measuring the moments of Landau's function against the analog solution. More specifically, based on Prinja's result and the documentation[23, 13, 3] about Landau's second moment-preservation, we may show while the first two energy-loss moments are preserved so are the first two energy-flux moments. This would strongly suggest, yet not mathematically prove, that the number of energy-flux moments preserved suggest a similar equivalence to the number of energy-loss moments preserved.

This numerically observed accuracy of moment-preserving approximations of Landau energy straggling theory will facilitate the accuracy of a continuous model based on the the Landau energy-loss algorithm which will be discussed in detail in the next chapter.

6.1 Landau Energy-Flux Moments

Now that it has been shown under the constraints of Landau that equivalence among energy-loss moments is true for any moment-preserving model, the following tables provide evidence to this result. The data presented shows the first five energy-flux moments of the benchmark compared to moments given by the Landau distribution along with the percent error to the benchmark. The values in parentheses are the $RE_{1\sigma}$ associated with the energy-flux calculations.

There is a noticeable change in $RE_{1\sigma}$ for all moments. Once a particle has $E_0 > 1MeV$, it takes a higher amount of particle samples to obtain converged values. After $5MeV$ some statistics are not within measurable means for higher order moments as a result of insignificant samples and high run-times for the standard analog benchmark.

Chapter 6. Lewis-type Theory for Moment-Preserving Energy Straggling

As seen in the previous chapter, there exists a direct relationship between incident energy and accuracy. For electron and positron energies above $1MeV$ there is convergence to the energy-flux moments within 1%. While for energies at or below $1MeV$ the convergence of moments begins to decrease. The difference in percent error is lower for water than for gold. This result is also seen in the spectra found in Figures 5.5 and 5.17 where the distribution around the most probable energy-loss of the benchmark is more broad than that of higher energies. Convergence in the percent error for water and gold is found at energies higher than $1MeV$ and is also seen in the spectra where areas of most probable energy-loss are nearly exact. This change in accuracy is due to the conditions made by Landau where energy-losses for thin slabs are much smaller compared to the incident energy. The use of low Z materials allows for smaller energy transfers since the ionization energy for these materials are small. For example, the ionization energy for water is $1.3 \times 10^{-4}MeV$ while for gold the ionization energy is $7.9 \times 10^{-4}MeV$. A lower ionization energy extends the validity of the Landau distribution and therefore increases the accuracy of the energy-loss sampling at lower energies. Furthermore, the ETRAN code[21] has also mentioned that the handling of energy-loss straggling becomes less adequate at low energies in materials of high atomic number.

The comparison of energy-flux moments have quantifiably supported the accuracy of Landau's distribution in terms of the first two moments. For energies above $1MeV$ Landau is exact within 1% to the 5th order. Although at energies less than $1MeV$ the moments begin to differ, Landau still remains quite accurate for low Z materials. Landau has only been given credit for the second energy-loss moment[23], yet without a quantifiable measurement. The relationship between energy-loss moments and energy-flux moments can not be shown to be equivalent if compared in the latter, yet the equivalence of the number of energy-loss moments relative to energy-flux moments strongly suggests the number of energy-flux moments preserved may equate to the number of energy-loss moments preserved. Given this suggestion, it is highly

probable that Landau may be capturing higher order moments as well.

Energy-Loss Data of 200keV Electrons on Gold (1 Electron Step)			
Cross Section	Möller	Landau	% Error
I_1	0.18373(6.72E-6)	0.18322(4.7E-6)	0.0%
I_2	3.4208E-2(2.09E-6)	3.3793E-2(1.60E-7)	1.2%
I_3	6.4248E-3(5.12E-7)	6.2671E-3(4.15E-7)	2.5%
I_4	1.2141E-3(1.15E-7)	1.1676E-3(9.69E-8)	3.8%
I_5	1.2660E-4(2.48E-8)	2.1842E-4(2.15E-8)	72%

Table 6.1: Table of values from simulations running 10^7 particles on Gold

Energy-Loss Data of 200keV Electrons on Water (1 Electron Step)			
Cross Section	Möller	Landau	% Error
I_1	0.18317(6.03E-6)	0.18339(3.93E-6)	0.4%
I_2	3.3914E-2(1.87E-6)	3.3788E-2(1.32E-6)	0.4%
I_3	6.3239E-3(4.54E-7)	6.2487E-3(3.89E-7)	1.2%
I_4	1.1851E-3(1.01E-7)	1.1592E-3(7.81E-7)	2.2%
I_5	2.2292E-4(2.15E-8)	2.1562E-4(1.71E-8)	3.3%

Table 6.2: Table of values from simulations running 10^7 particles on Water

Energy- Loss Data of 500keV Electrons on Gold (1 Electron Step)			
Cross Section	Möller	Landau	% Error
I_1	0.45871(1.54E-6)	0.45838(1.14E-6)	0.1%
I_2	0.21280(1.20E-5)	0.21144(9.59E-6)	0.6%
I_3	9.9465E-2(7.38E-6)	9.8017E-2(6.13E-7)	1.5%
I_4	4.6741E-2(4.13E-6)	4.5625E-2(3.51E-7)	2.4%
I_5	2.2053E-2(2.21E-6)	2.1310E-2(1.94E-7)	3.4%

Table 6.3: Table of values from simulations running 10^7 particles on Gold

Energy-Loss Data of 500keV Electrons on Water (1 Electron Step)			
Cross Section	Möller	Landau	% Error
I_1	0.45088(1.50E-6)	0.45848(9.89E-6)	1.7%
I_2	0.20555(1.15E-5)	0.21119(8.18E-6)	2.7%
I_3	9.4395E-2(6.89E-6)	9.7632E-2(5.17E-7)	3.4%
I_4	4.3574E-2(3.78E-6)	4.5269E-2(2.95E-7)	3.7%
I_5	2.0193E-2(2.21E-6)	2.1041E-2(1.60E-7)	4.2%

Table 6.4: Table of values from simulations running 10^7 particles on Water

Energy-Loss Data of 1MeV Electrons on Gold (1 Electron Step)			
Cross Section	Möller	Landau	% Error
I_1	0.91730(2.87E-5)	0.91692(2.34E-5)	0.0%
I_2	0.84973(4.52E-5)	0.84621(2.82E-5)	0.4%
I_3	0.79239(5.53E-5)	0.78481(4.81E-5)	0.9%
I_4	0.74247(6.19E-5)	0.73067(5.49E-5)	1.5%
I_5	0.69822(6.62E-5)	0.68242(5.97E-5)	2.5%

Table 6.5: Table of values from simulations running 5×10^7 particles on Gold

Energy-Loss Data of 1MeV Electrons on Water (1 Electron Step)			
Cross Section	Möller	Landau	% Error
I_1	0.91675(1.16E-5)	0.91700(2.06E-5)	0.03%
I_2	0.84716(1.82E-5)	0.84512(3.33E-5)	0.2%
I_3	0.78713(2.21E-5)	0.78181(1.81E-5)	0.7%
I_4	0.73423(2.46E-5)	0.72537(2.10E-5)	1.2%
I_5	0.68691(2.63E-5)	0.67457(2.26E-5)	1.8%

Table 6.6: Table of values from simulations running 5×10^7 particles on Water

Energy-Loss Data of 5MeV Electrons on Gold (1 Electron Step)			
Cross Section	Möller	Landau	% Error
I_1	4.5869 (3.95E-5)	4.5850(3.90E-5)	0.0%
I_2	21.196 (3.12E-4)	21.175(3.00E-4)	0.1%
I_3	98.456 (1.91E-3)	98.250(1.82E-3)	0.2%
I_4	459.04 (1.07E-2)	457.42(1.02E-2)	0.3%
I_5	2146.4 (5.70E-2)	2135.1(5.44E-2)	0.5%

Table 6.7: Table of values from simulations running 10^8 particles on Gold

Energy-Loss Data of 5MeV Electrons on Water (1 Electron Step)			
Cross Section	Möller	Landau	% Error
I_1	4.5863 (3.61E-5)	4.5849(1.12E-4)	0.0%
I_2	21.164 (2.85E-4)	21.147(8.62E-4)	0.1%
I_3	98.091 (1.74E-3)	97.916(1.82E-3)	0.2%
I_4	456.06 (9.68E-3)	454.62(1.02E-2)	0.3%
I_5	2125.4 (5.14E-2)	2115.3(5.44E-2)	0.5%

Table 6.8: Table of values from simulations running 10^8 particles on Water

Energy-Loss Data of 10MeV Electrons on Gold (1 Electron Step)			
Cross Section	Möller	Landau	% Error
I_1	9.1738 (1.07E-4)	9.1701(1.09E-4)	0.0%
I_2	84.730 (1.69E-3)	84.695(1.67E-3)	0.0%
I_3	786.27 (2.07E-2)	785.75(2.01E-2)	0.1%
I_4	7321.6 (2.30E-1)	7312.7(2.22E-1)	0.1%

Table 6.9: Table of values from simulations running 5×10^7 particles on Gold

Energy-Loss Data of 10MeV Electrons on Water (1 Electron Step)			
Cross Section	Möller	Landau	% Error
I_1	9.1729 (2.19E-4)	9.1670(2.24E-4)	0.1%
I_2	84.624 (3.46E-3)	84.594(3.41E-3)	0.0%
I_3	783.81 (4.22E-2)	783.33(4.10E-2)	0.1%
I_4	7281.0 (4.99E-1)	7272.6(4.52E-1)	0.1%

Table 6.10: Table of values from simulations running 10^7 particles on Water

Energy-Loss Data of 20MeV Electrons on Gold (1 Electron Step)			
Cross Section	Möller	Landau	% Error
I_1	18.34 (4.59E-4)	18.34(4.83E-4)	0.00%
I_2	338.7 (1.44E-2)	338.7(1.45E-2)	0.00%
I_3	6281 (3.54E-1)	6281(3.49E-1)	0.00%

Table 6.11: Table of values from simulations running 10^7 particles on Gold

Energy-Loss Data of 20MeV Electrons on Water (1 Electron Step)			
Cross Section	Möller	Landau	% Error
I_1	18.345 (4.24E-4)	18.340(1.99E-4)	0.03%
I_2	338.36 (1.33E-2)	338.35(5.99E-2)	0.00%
I_3	6264.0(3.26E-1)	6264.4(1.43E-1)	0.00%

Table 6.12: Table of values from simulations running 10^7 particles on Water

Energy-Loss Data of 200keV Positrons on Gold (1 Electron Step)			
Cross Section	Bhabha	Landau	% Error
I_1	0.18601 (6.23E-6)	0.18308(5.11E-6)	1.6%
I_2	3.4990E-2(1.82E-6)	3.3779E-2(1.72E-7)	3.5%
I_3	6.6196E-3 (4.44E-7)	6.2724E-3(4.48E-7)	5.2%
I_4	1.2575E-3 (1.00E-7)	1.1709E-3(1.04E-7)	6.9%
I_5	2.3963E-4 (2.18E-8)	2.1960E-4(2.32E-8)	8.4%

Table 6.13: Table of values from simulations running 10^7 particles on Gold

Energy-Loss Data of 200keV Positrons on Water (1 Electron Step)			
Cross Section	Bhabha	Landau	% Error
I_1	0.18532(5.50E-6)	0.18596(4.62E-6)	0.3%
I_2	3.4646E-2(1.59E-6)	3.4792E-2(1.56E-7)	0.4%
I_3	6.5067E-3(3.86E-7)	6.5436E-3(4.14E-7)	0.6%
I_4	1.2259E-3(8.67E-7)	1.2358E-3(9.78E-8)	0.8%
I_5	2.3156E-4(1.87E-8)	2.3425E-4(2.19E-8)	1.2%

Table 6.14: Table of values from simulations running 10^7 particles on Water

Energy-Loss Data of 500keV Positrons on Gold (1 Electron Step)			
Cross Section	Bhabha	Landau	% Error
I_1	0.46583(1.29E-5)	0.45849(1.06E-5)	1.6%
I_2	0.21869(9.77E-6)	0.21135(8.84E-5)	3.4%
I_3	0.10312(6.01E-6)	9.7843E-2(5.60E-6)	5.1%
I_4	4.8781E-2(3.42E-6)	4.5451E-2(3.20E-6)	6.8%
I_5	2.3135E-2(1.87E-6)	2.1173E-2(1.73E-6)	8.5%

Table 6.15: Table of values from simulations running 10^7 particles on Gold

Energy-Loss Data of 500keV Positrons on Water (1 Electron Step)			
Cross Section	Bhabha	Landau	% Error
I_1	0.45799 (1.25E-5)	(1.25E-5)	1.6%
I_2	0.21134 (9.25E-6)	(1.72E-5)	3.2%
I_3	9.7931E-2 (5.59E-6)	E-2 (6.70E-6)	4.7%
I_4	4.5521E-2 (3.13E-6)	E-2 (3.87E-6)	6.0%
I_5	2.1211E-2 (1.68E-6)	E-2(2.12E-6)	7.1%

Table 6.16: Table of values from simulations running 10^7 particles on Water

Energy-Loss Data of 1MeV Positrons on Gold (1 Electron Step)			
Cross Section	Bhabha	Landau	% Error
I_1	0.9169 (8.45E-7)	0.9169 (8.04E-7)	0.0%
I_2	0.8478 (1.24E-6)	0.8471 (1.31E-6)	0.1%
I_3	0.7876 (1.50E-6)	0.7872 (1.65E-6)	0.1%
I_4	0.7343 (1.69E-6)	0.7348 (1.89E-6)	0.1%
I_5	0.6864 (1.82E-6)	0.6885 (2.06E-6)	0.3%

Table 6.17: Table of values from simulations running 10^8 particles on Gold

Energy-Loss Data of 1MeV Positrons on Water (1 Electron Step)			
Cross Section	Bhabha	Landau	% Error
I_1	0.92776 (9.85E-6)	0.92796 (9.23E-6)	0.0%
I_2	0.86560 (1.46E-5)	0.86537 (1.51E-5)	0.0%
I_3	0.81015 (1.78E-5)	0.81000 (1.91E-5)	0.0%
I_4	0.76000 (2.01E-5)	0.76034 (2.19E-5)	0.0%
I_5	0.71428 (2.18E-5)	0.71539 (2.38E-5)	0.2%

Table 6.18: Table of values from simulations running 5×10^7 particles on Water

Energy-Loss Data of 5MeV Positrons on Gold (1 Electron Step)			
Cross Section	Bhabha	Landau	% Error
I_1	4.587 (1.26E-4)	4.585 (1.30E-4)	0.0%
I_2	21.20 (9.03E-4)	21.19 (1.00E-3)	0.0%
I_3	98.40 (5.37E-3)	98.44 (6.09E-3)	0.0%
I_4	457.8 (2.98E-2)	459.1 (3.40E-2)	0.3%
I_5	2134 (1.59E-1)	2147 (1.82E-1)	0.6%

Table 6.19: Table of values from simulations running 10^7 particles on Gold

Energy-Loss Data of 5MeV Positrons on Water (1 Electron Step)			
Cross Section	Bhabha	Landau	% Error
I_1	4.6207(1.10E-4)	4.6191 (1.12E-4)	0.0%
I_2	21.473(7.89E-4)	21.462 (8.70E-4)	0.1%
I_3	100.07(4.72E-3)	100.11 (5.30E-3)	0.0%
I_4	467.32(2.62E-2)	468.21 (2.96E-2)	0.2%
I_5	2185.8(1.41E-1)	2194.4 (1.58E-1)	0.4%

Table 6.20: Table of values from simulations running 10^7 particles on Water

Energy-Loss Data of 10MeV Positrons on Gold (1 Electron Step)			
Cross Section	Bhabha	Landau	% Error
I_1	9.175 (2.48E-4)	9.169 (2.45E-4)	0.1%
I_2	84.79 (3.50E-3)	84.69 (3.73E-3)	0.1%
I_3	786.4 (4.15E-2)	785.7 (4.49E-2)	0.1%
I_4	7312 (4.59E-1)	7312 (4.98E-1)	0.0%

Table 6.21: Table of values from simulations running 10^7 particles on Gold

Energy-Loss Data of 10MeV Positrons on Water (1 Electron Step)			
Cross Section	Bhabha	Landau	% Error
I_1	9.0168 (2.45E-4)	9.0117 (2.53E-4)	0.1%
I_2	81.906 (3.40E-3)	81.852 (3.77E-3)	0.1%
I_3	746.69 (3.95E-2)	747.08 (4.46E-2)	0.1%
I_4	6824.3 (4.30E-1)	6842.1 (4.86E-1)	0.0%

Table 6.22: Table of values from simulations running 10^7 particles on Water

Energy-Loss Data of 20MeV Positrons on Gold (1 Electron Step)			
Cross Section	Bhabha	Landau	% Error
I_1	18.35 (1.53E-4)	18.34 (1.53E-4)	0.1%
I_2	339.0 (4.29E-3)	338.7 (4.61E-3)	0.1%
I_3	6283 (1.01E-1)	6281 (1.10E-1)	0.0%

Table 6.23: Table of values from simulations running 10^7 particles on Gold

Energy-Loss Data of 20MeV Positrons on Water (1 Electron Step)			
Cross Section	Bhabha	Landau	% Error
I_1	18.447(1.35E-4)	18.441 (1.99E-4)	0.0%
I_2	342.12(3.84E-3)	342.07 (6.03E-3)	0.0%
I_3	6361.9(9.11E-1)	6367.8 (1.45E-1)	0.1%

Table 6.24: Table of values from simulations running 10^7 particles on Water

Chapter 7

Landau Pseudo-Transport(LPT) Model

We now present a moment-preserving single-event positron/electron transport formulation. It has been shown that Landau's energy-loss distribution matches the energy-flux moments of our "exact" analog model suggesting an equivalent moment-preserving cross section. In order to connect Landau with the transport problem in question, we first begin by defining Landau as a differential cross section by recalling the definition of an energy-loss cross section:

$$\Sigma(E' \rightarrow E) = \Sigma(E')P(E' \rightarrow E,), \quad \int P(E' \rightarrow E,)dE = 1 \quad (7.1)$$

where $\Sigma(E')$ is the total cross section in cm^{-1} and P is the probability of an energy-loss from E' to E . Therefore a "Landau" cross section Σ_L can be defined by:

$$\Sigma_L(E' \rightarrow E) = \Sigma_L(E')f(E' \rightarrow E), \quad (7.2)$$

The function $f(E' \rightarrow E)$ is Landau's function and has been formulated such that $\int fdE = 1$. Energy-losses sampled from this function are based on the step-size input by the user. In other words, Landau samples the probability of an energy-loss

Chapter 7. Landau Pseudo-Transport(LPT) Model

per given distance traveled by the particle. This is the exact definition of the total cross section and now:

$$\Sigma_L(E') = \frac{1}{\lambda_L} \quad , \quad \lambda_L = s(E'), \quad (7.3)$$

where λ_L is the mean free path(MFP) equal to an energy-dependent step-size. More specifically, the step-size is equal to the distance traveled for a particle with an initial energy E' suffering an energy-loss equal to 8.3% (Section 5.1). Our pseudo-transport equation becomes:

$$\frac{\partial \psi(s, E)}{\partial s} = \int_{E_{min}}^{E_{max}} \Sigma_L(E_0) [\psi(s, E') - \psi(s, E)] dE' \quad (7.4)$$

$$\psi(0, E) = \delta(E - E_0). \quad (7.5)$$

We now have a moment-preserving cross section that is both smooth and continuous and can easily be solved through single-event Monte Carlo. We will further refer to this model as the Landau pseudo-transport(LPT) model. The formation of the Landau single-event transport will follow the same sequence as discussed in Chapter 3. The sampling of a distance to collision will be substituted by the relative Landau step-size. As a result, a particle will no longer be moved an arbitrary distance specified by the user, rather an exponential distribution of the mean free path(MFP), but in our case the step-size, will be sampled moving the particle, on average, the distance of the step-size. Once the distance to collision has been sampled, the energy transfer suffered within this collision will then be sampled from the Landau energy-loss distribution based on the incident energy and step-size used in the distance to collision sampling. The implementations above should provide a continuous transport model of energy-loss straggling speeding up the transport of positrons and electrons by allowing longer MFP's and smoother energy-loss distributions. A more detailed description is provided as well as energy-loss spectra and energy deposition comparisons to the benchmark.

7.0.1 Distance to Collision

The “random walk” sequence outlined in Chapter 3 will be followed. The step-size chosen will be based on the accepted value of $k = 8$ (Chapter 5) for the major step and a substep value chosen by the user. The following equations show the manner in which the distance to collision will be sampled:

$$\text{step} = [E * (1 - 2^{-\frac{1}{8}})]/\text{substeps} \quad (7.6)$$

$$\lambda_L = \text{step} \quad (7.7)$$

$$P(s)_{coll} ds = e^{-s/\lambda_L} \frac{1}{\lambda_L} ds \quad (7.8)$$

$$C(s) = \int_0^s P(s')_{coll} ds' \quad (7.9)$$

$$s = -\lambda_L \log(\xi_1). \quad (7.10)$$

Throughout the transport the step-size is verified to meet the constraints in Equation 4.36. If at any point throughout the “random walk” the step falls below the Landau constraint, the step is then changed to the smallest allowable step-size based on allowable values of ξ/I given by the ETRAN code[21]. Throughout, the MFP of the true differential cross section is computed and compared to the current step-size. If the step-size falls below the true MFP then the code will switch to the actual analog differential cross section since there will no longer be an advantage using Landau.

7.0.2 Energy-Loss

Next, a straggling value is randomly chosen from the Landau distribution described in Chapter 4. This distribution is solely based on the step-size computed above (**step**), the incident energy (**energy**), and the relative stopping power computed by the first moment of the respective differential cross section (**qs_csda**). The Landau

energy-loss routine `strag_landau`[23], Section 4.2.4, will sample an energy-loss as follows:

$$Q = (\text{qs_csda} + \text{strag_landau}(\text{energy}, \text{step}, \text{qs_csda})) * \text{step}. \quad (7.11)$$

This will continue until the particle has reached a boundary or the particle has lost all of it's energy.

The following sections will provide distributions of energy-loss spectra and dose for gold and water. In this section we will discuss the effect of changing MFP's in the Landau single-event model and leave the detailed discussion of comparison to the benchmark for the next chapter. Due to the decrease in accuracy of Landau found in Chapter 6, gold and water will be evaluated at energies $E \geq 1\text{MeV}$.

7.1 Energy-Loss Spectra

Different substeps have been chosen in order to show how the LPT model varies with step-size. Substeps are chosen to be 1, 5, 10, and 20. The constraint set by Landau where the energy-losses must be sufficiently larger than the incident energy, is seen to have an effect on the step-size at $E_0 = 1\text{MeV}$. In Table 7.1 the largest number of substeps for 1MeV electrons and positrons on water and gold is 14. Looking at Table 7.1 and Table 7.5, with increasing substeps the MFP is nearly as short as the analog MFP. While MFP's are energy dependent, at some point during the transport the step-size becomes smaller than the analog, at that point the cross sections switch to the analog cross section. This can be seen in the tail of 10 and 14 substeps for 1MeV positrons on gold. Efficiency is lost by the Landau distribution once the MFP is close to the benchmark MFP, a comparison of CPU time shows this. For 1MeV positrons on gold, the benchmark calculation is faster than Landau while the MFP of Landau is 10^{-4}cm greater than the benchmark. As incident energies increase, this is

Chapter 7. Landau Pseudo-Transport(LPT) Model

no longer an issue. While MFP's are greater than that of the benchmark, significant speed-ups arise in CPU time.

There is a direct connection between the number of substeps and runtime. For increasing substeps, the MFP is reduced causing more collisions and increasing the runtime of the simulation. For electrons in gold, there is a linear relationship between the number of substeps, number of collisions and runtime. Table 7.3 shows that for 1 substep there is an average of 1 collision with a CPU time of $6.4min$, while for 10 substeps there is an average of 10 collisions with a CPU time close to $60min$. This relationship does not exist in water. Table 7.2 and Table 7.3 show that $1MeV$ electrons suffer 5 times more collisions in 1 Estep of water versus 1 Estep of gold.

A distinct artifact that the LPT model produces, is relative to the λ_{cut} value discussed in Chapter 5. Chapter 5 showed there was an increase of this drop-off point with increasing energy for the Landau distribution, Figures 7.1 and 7.3 verify this characteristic. Despite the artifact inherent in the Landau distribution, the energy-loss spectra are closely matched for electrons.

Positrons show a similar artifact. The Bhabha cross section does not have an indistinguishability issue and therefore a drop-off of $E_0/2$ does not occur, yet there still exist a cutoff in the Landau distribution which is seen in Figure 7.5 and Figure 7.6.

There is a clear relationship between the distribution and the number of substeps. For a single substep, most of the particles are not colliding within the slab. As a result, the energy-loss is not computed for those particles. Looking at Figure 7.2 it may appear using 1 substep has a better $RE_{1\sigma}$ than higher substeps but this is due to an insignificant number of particles being sampled in these energy bins. As the substeps increase the distribution becomes more defined, higher energy-losses become more probable and more energy bins receive significant particle samples. This is seen in all energy-loss spectra computed.

Chapter 7. Landau Pseudo-Transport(LPT) Model

Tables 7.1 and 7.2 show an increase of mean energy-loss and most probable energy-loss with increasing substeps. For $1MeV$ electrons on water, the mean energy-loss changes by less than 1% from 1 substep to 14 while for $10MeV$ electrons the mean energy-loss is identical from 5 substep to 20, yet for both energies the most probable energy-loss is always $0MeV$ for 1 substep and by 5 substeps the value has converged. This relationship can be seen in Figures 7.1 and 7.3. As the substeps are increased, the distribution about the most probable becomes more peaked.

The energy-loss spectra for gold and water show overall convergence to the benchmark solution around the area of most probable energy-losses. There is a significant difference in MFP's for gold and water when compared to their benchmark's. In Tables 7.2 and 7.3 Gold's MFP at 20 substeps is 5 times longer than its benchmark where water at 20 substeps is 26 times longer. By increasing the substeps to 40 for water, the MFP is 13 times larger than the benchmark and the spectra for 40 substeps moves closer to the benchmark. This difference in MFP's and spectra show there exists a direct connection with step-size and number of collisions associated with that step-size.

It is clear that particle energies greater than $1MeV$ have smaller changes in mean energy-loss with respect to substeps yet most probable energy-losses remain dependent. Also, the energy-loss distribution is more defined for greater substeps. This is caused by the reduction of MFP's, reducing the estimation of the straggling over a given step-size, increasing the collisions within the simulated material and allowing for significant sampling at higher energy-losses. This implies that the pseudo-transport algorithm is highly dependent on step-size. Longer step-sizes reduce the number of energy-loss sampling within a given slab while transporting the particle further within the medium. Small step-sizes increase the number of energy-loss sampling within the slab while transporting the particle a shorter distance.

Chapter 7. Landau Pseudo-Transport(LPT) Model

LPT Energy-Loss Data of 1MeV Electrons on Water					
Substeps	1	5	10	14	Benchmark
Mean Energy-Loss (<i>cm</i>)	8.33E-2	8.33E-2	8.34E-2	8.35E-2	8.33E-3
Most Probale Eloss (<i>cm</i>)	0.00	4.67E-2	5.33E-2	5.33E-2	4.67E-2
MFP(<i>cm</i>)	4.64E-2	1.83E-3	9.14E-3	6.54E-3	1.41E-3
Collisions	2.07	5.27	10.54	14.74	68.2
Fraction Uncollided	0.14	0.01	0.00	0.00	0.00
Runtime (<i>min</i>)	13.0	29.7	54.4	74.1	116.8

Table 7.1: Table of values from 10^8 samples on $9.6 \times 10^{-2}cm$ of Water.

LPT Energy-Loss Data of 10MeV Electrons on Water						
Substeps	1	5	10	20	40	Benchmark
Mean Energy-Loss (<i>cm</i>)	1.057	1.057	1.057	1.057	1.057	8.271E-1
Most Probale Eloss (<i>cm</i>)	0.0	6.67E-1	7.33E-1	7.33E-1	7.33E-1	5.33E-1
MFP(<i>cm</i>)	4.17E-1	1.66E-1	8.35E-2	4.17E-2	2.08E-2	1.25E-4
Collisions	2.71	6.78	13.56	27.10	54.19	551.3
Fraction Uncollided	0.08	0.00	0.00	0.00	0.00	0.00
Runtime (<i>min</i>)	3.3	7.4	13.5	26.4	51.0	421.8

Table 7.2: Table of values from 10^7 samples on $1.13cm$ of Water.

LPT Energy-Loss Data of 10MeV Electrons on Gold					
Substeps	1	5	10	20	Benchmark
Mean Energy-Loss (<i>cm</i>)	8.261E-1	8.265E-1	8.293E-1	8.380E-1	8.262E-1
Most Probale Eloss (<i>cm</i>)	0.00	4.67E-1	4.67E-1	5.33E-1	4.67E-1
MFP(<i>cm</i>)	7.33E-1	1.43E-2	7.15E-3	3.57E-3	6.57E-4
Collisions	1.05	5.23	10.45	20.9	113.7
Fraction Uncollided	0.37	0.01	0.00	0.00	0.00
Runtime (<i>min</i>)	6.4	29.2	53.2	101.3	439.0

Table 7.3: Table of values from 5×10^7 samples on $7.5 \times 10^{-2}cm$ of Gold.

Chapter 7. Landau Pseudo-Transport(LPT) Model

LPT Energy-Loss Data of 1MeV Positrons on Water					
Substeps	1	5	10	14	Benchmark
Mean Energy-Loss (<i>cm</i>)	7.221E-2	7.223E-2	7.251E-2	7.330E-2	7.223E-2
Most Probale Eloss (<i>cm</i>)	0.00	0.00	4.0E-1	4.0E-1	4.67E-1
MFP(<i>cm</i>)	2.71E-2	2.12E-2	1.06E-2	5.31E-3	1.41E-3
Collisions	3.55	4.5	9.07	18.1	68.1
Fraction Uncollided	0.04	0.01	0.00	0.00	0.00
Runtime (<i>min</i>)	20.0	25.6	46.3	87.1	263.2

Table 7.4: Table of values from 10^8 samples on $9.6 \times 10^{-2}cm$ of Water.

LPT Energy-Loss Data of 1MeV Positrons on Gold					
Substeps	1	5	10	14	Benchmark
Mean Energy-Loss (<i>cm</i>)	8.576E-2	8.657E-2	8.973E-2	9.153E-2	8.313E-2
Most Probale Eloss (<i>cm</i>)	0.00	3.0E-2	4.67E-1	4.67E-1	4.67E-2
MFP(<i>cm</i>)	2.41E-3	1.93E-3	9.63E-4	6.48E-4	5.84E-4
Collisions	4.21	5.27	10.5	15.7	17.44
Fraction Uncollided	0.02	0.00	0.00	0.00	0.00
Runtime (<i>min</i>)	47.8	58.0	108.1	150.9	142.1

Table 7.5: Table of values from 10^8 samples on $1.0 \times 10^{-2}cm$ of Gold.

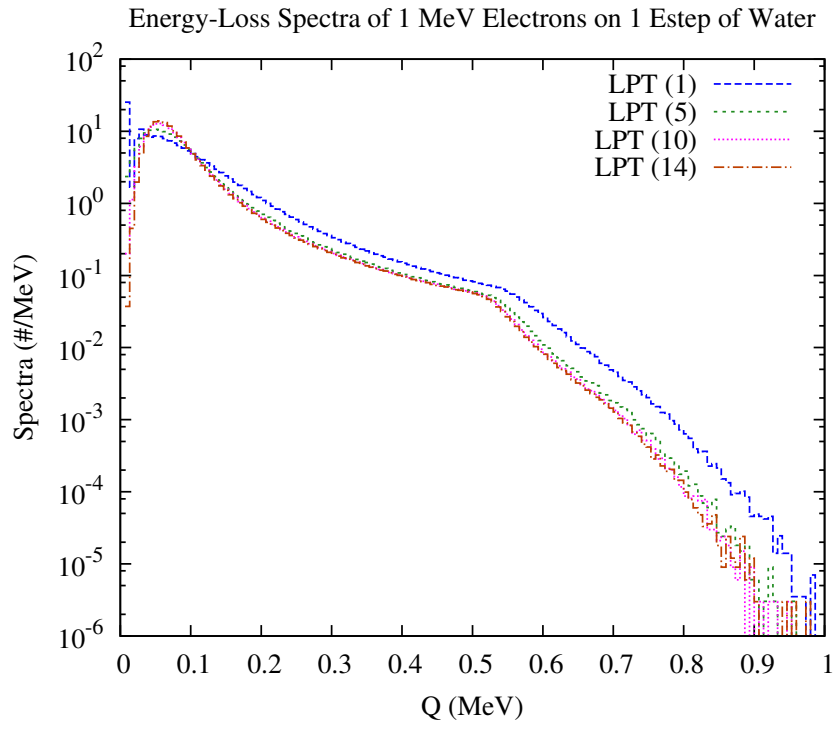


Figure 7.1: Energy-Loss Spectra of 1 MeV Electrons on $9.6 \times 10^{-2} cm$ of Water

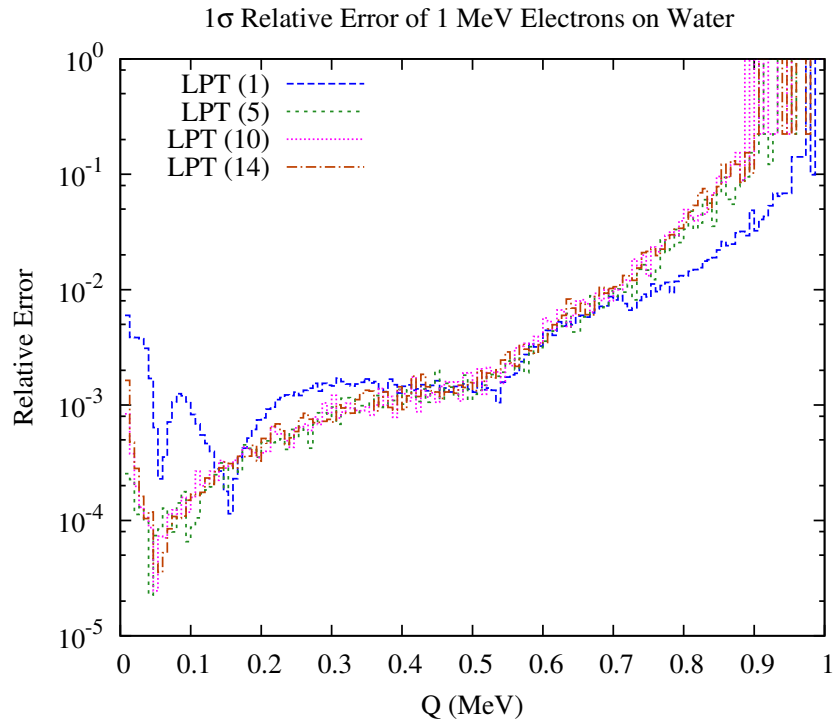


Figure 7.2: Relative Error of 1 MeV Electrons on $9.6 \times 10^{-2} cm$ of Water

Chapter 7. Landau Pseudo-Transport(LPT) Model

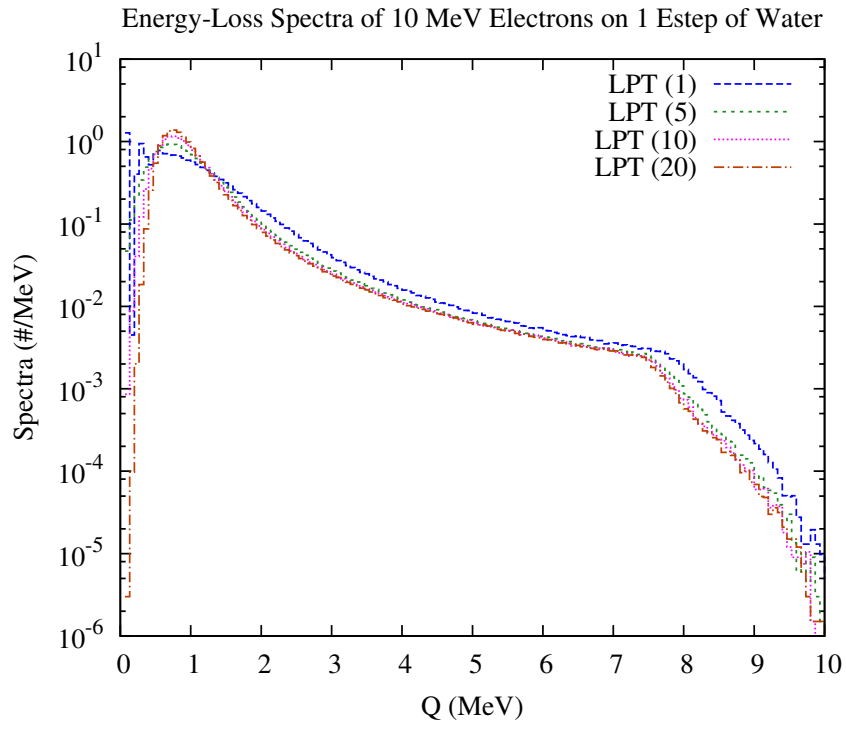


Figure 7.3: Energy-Loss Spectra of 10 *MeV* Electrons on 1.31*cm* of Water

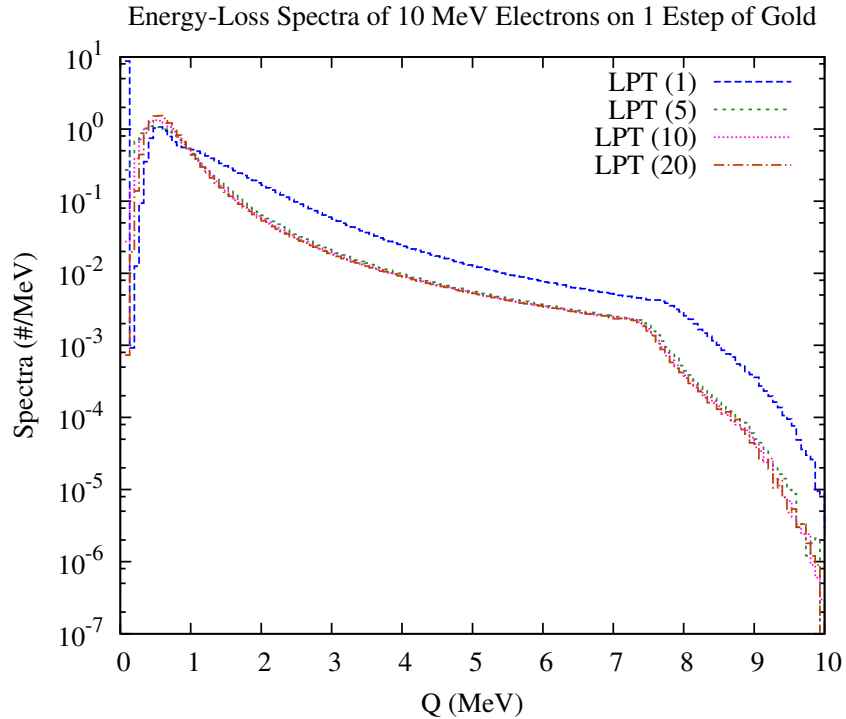


Figure 7.4: Energy-Loss Spectra of 10 *MeV* Electrons on 7.5×10^{-2} *cm* of Gold

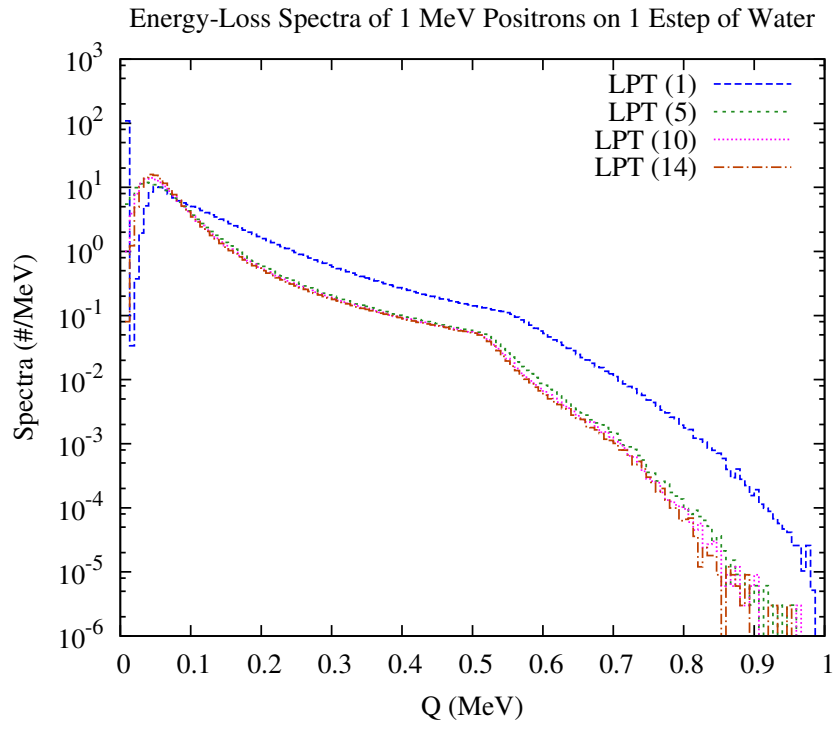


Figure 7.5: Energy-Loss Spectra of 1 MeV Positrons on $9.6 \times 10^{-2} cm$ of Water

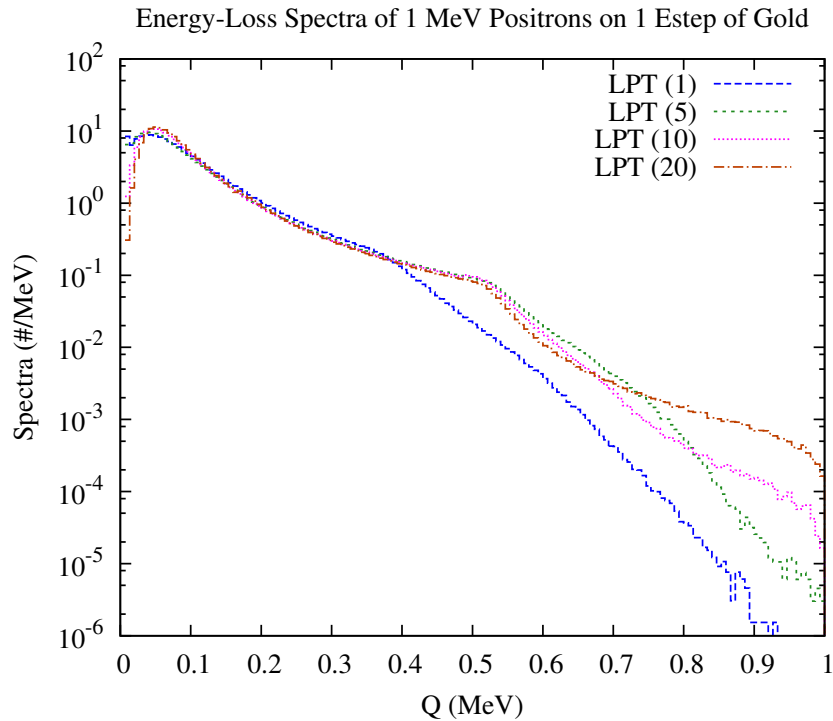


Figure 7.6: Energy-Loss Spectra of 1 MeV Positrons on $8.52 \times 10^{-3} cm$ of Gold

7.2 Energy Deposition

Energy-loss spectra of thin slabs has proved a dependence on step-size for LPT model of charged particles. An investigation of energy deposition is made to show how this dependence effects the dose of the material.

Figures 7.7 and 7.9 show a difference in energy deposition for $1MeV$ electrons. For water, a difference in substeps does not change the energy deposited in the first $0.5cm$ of the slab. Once the electron has passed this point an increase of energy deposition is seen relative to the number of substeps. For gold, the magnitude of substeps determines the magnitude of energy deposited within the slab. Higher substeps deposit more energy than those of lower substeps. The depth of the electrons for substeps greater than 1 substep does not change significantly. The use of 10 substeps increases the dose by almost 10% while reducing the depth of the particle by almost 15%. The cause of this difference in materials is due to the constraints set by the Landau routine. The use of low Z materials allows for smaller substeps since the ionization energy for these materials is smaller. A lower ionization energy extends the validity of the Landau distribution and therefore increases the accuracy of the energy-loss sampling.

Figures 7.11 and 7.13 show a decrease in material dependence for higher energy electrons. Again for water, up to a depth of about $5cm$ a single substep provides the same energy deposition as all the other substeps. After this point there is a reduction in energy deposition with an increase of penetration for a single substep. As the substeps increase, the energy deposition also increases while the distance traveled by the particle is reduced. Although the length of this slab is sufficiently large enough to guarantee a complete energy-loss of a $20MeV$ electron, there is still a small fraction of electrons that penetrate through the slab. For gold, there is no longer a change in the magnitude of energy deposited for a change in substeps.

Chapter 7. Landau Pseudo-Transport(LPT) Model

Figure 7.13 shows this.

The relative errors presented in Figures 7.8, and 7.10 are evidence of the biasing produced by the substeps. For a single substep, a reduction in energy deposited produces a higher relative error since the particle is allowed to move further within the slab thus increasing the spread of energy deposited. Substeps greater than 1 reduce this spreading, causing a more concentrated deposition, decreasing the relative errors.

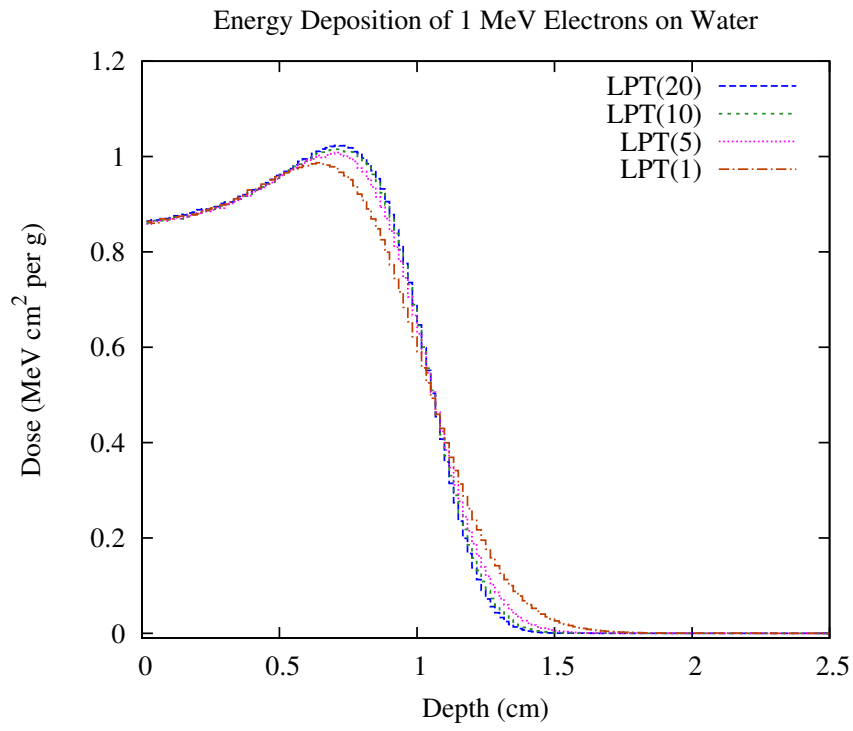


Figure 7.7: Energy Deposition of 1 *MeV* Electrons on 2.5cm of Water

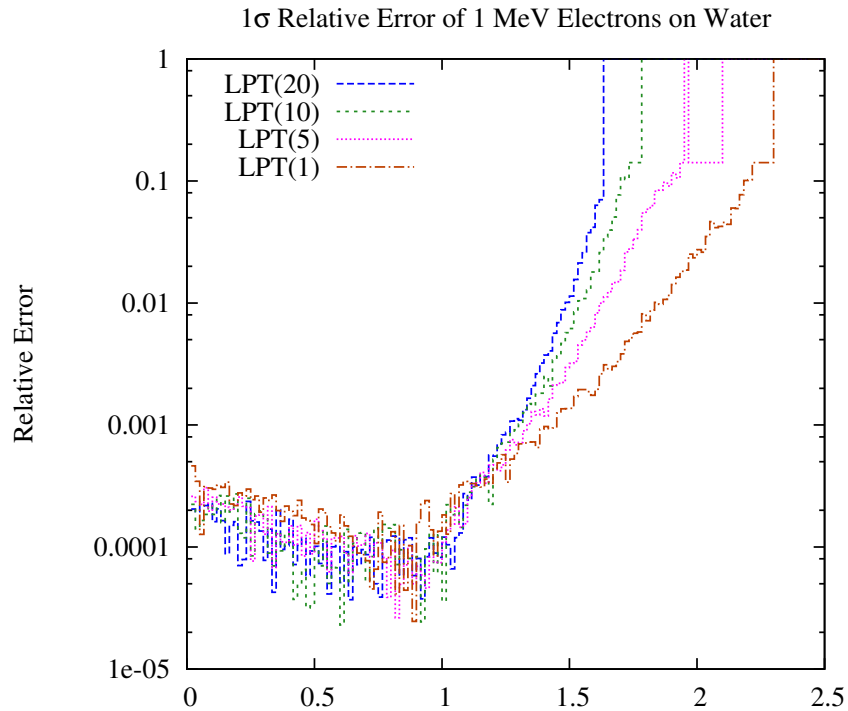


Figure 7.8: Relative Error of 1 *MeV* Electrons on 2.5cm of Water

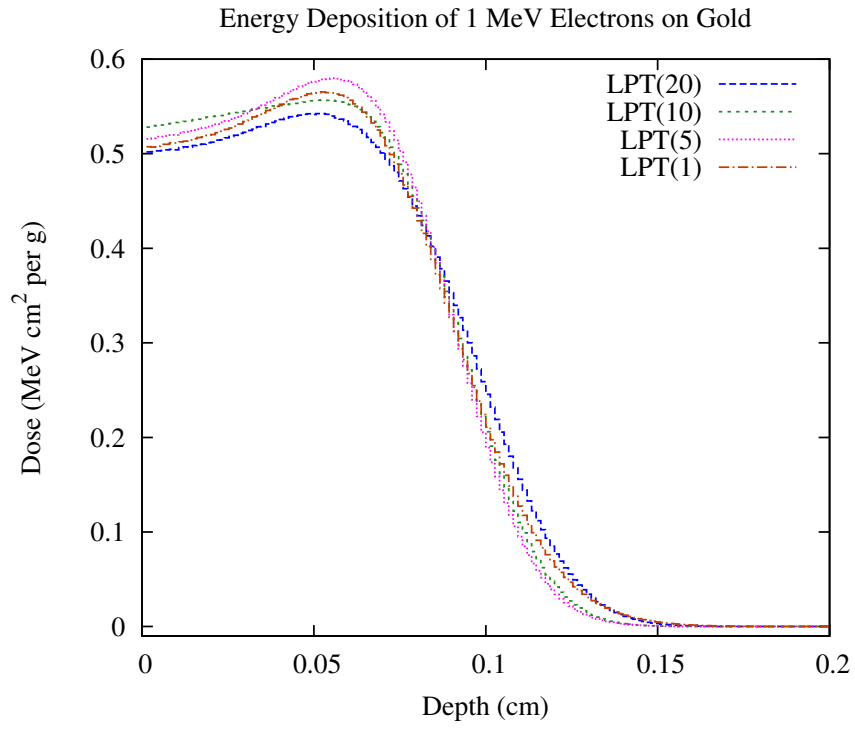


Figure 7.9: Energy Deposition of 1 *MeV* Electrons on 0.2cm of Gold

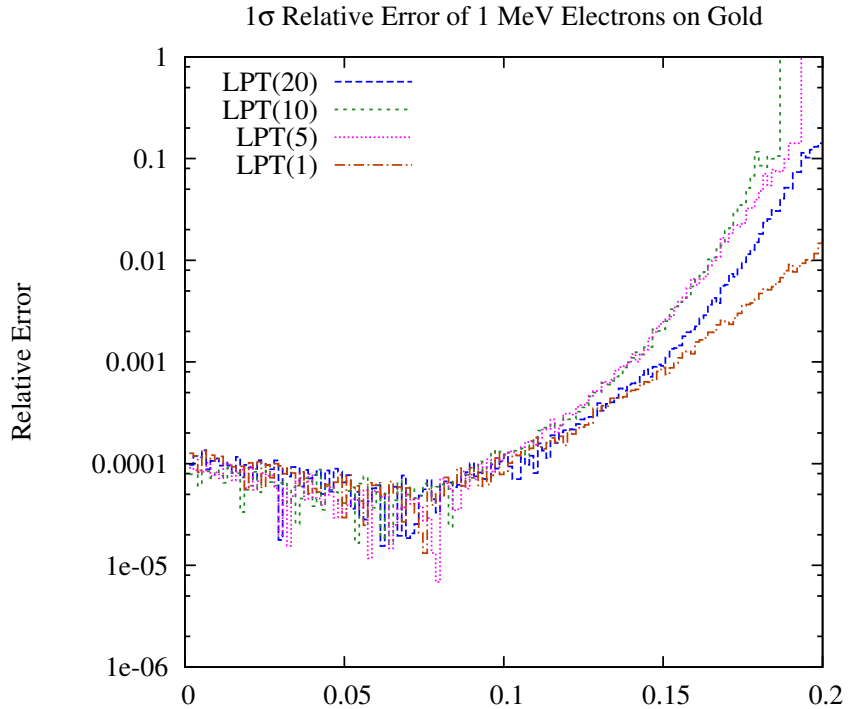


Figure 7.10: Relative Error of 1 *MeV* Electrons on 0.2cm of Gold

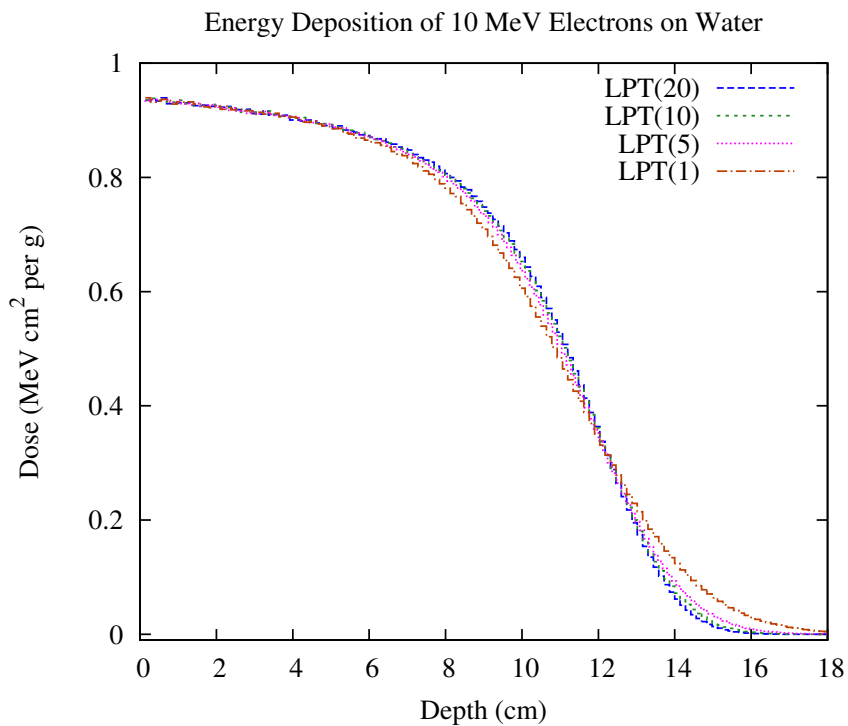


Figure 7.11: Energy Deposition of 10 MeV Electrons on 18cm of Water

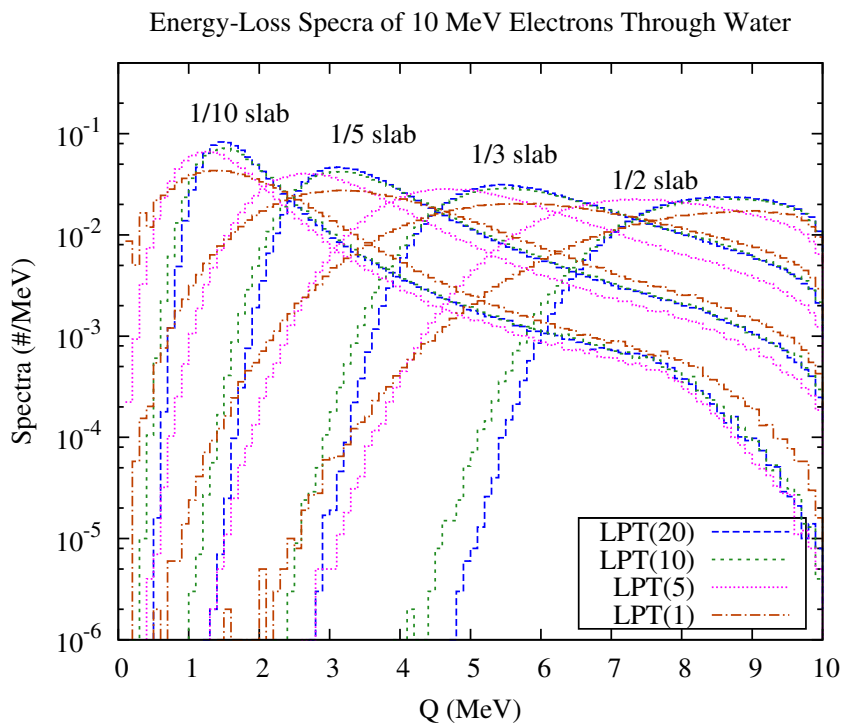


Figure 7.12: Energy Deposition of 10 MeV Electrons through 18cm of Water

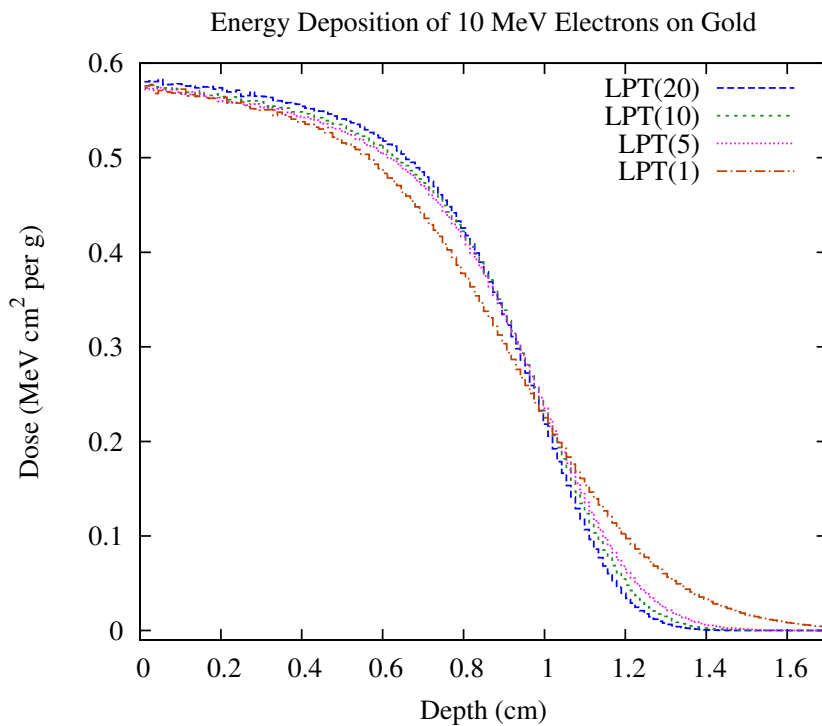


Figure 7.13: Energy Deposition of 10 MeV Electrons on 1.7cm of Gold

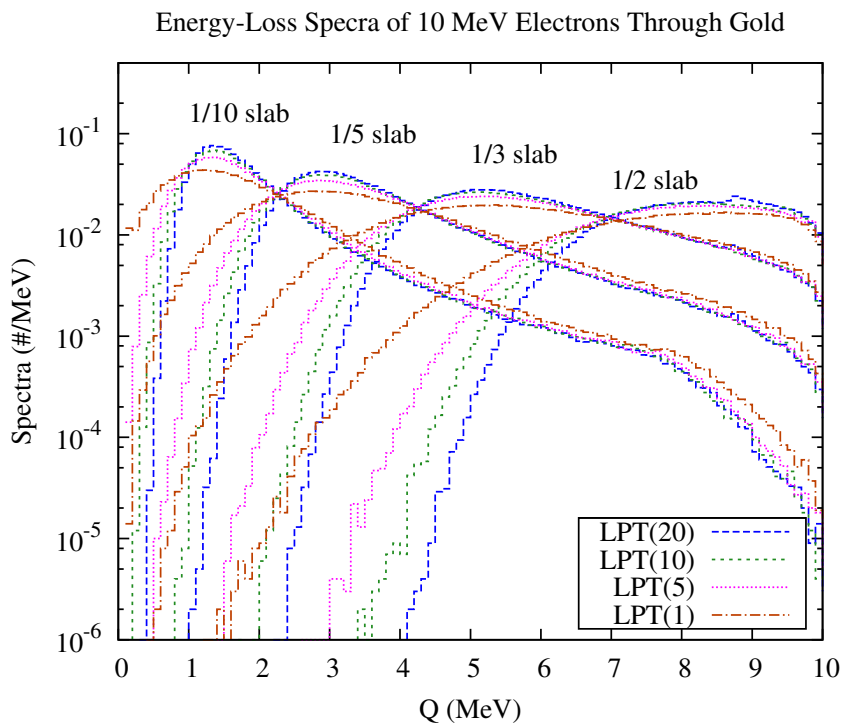


Figure 7.14: Energy-loss of 10 MeV Electrons through 1.7cm of Gold

Chapter 8

Results and Comparisons to the Benchmark

Having examined energy-loss spectra and energy deposition of particles incident on varying widths of gold and water, results show a strong dependence on step-size. Convergence in the distribution, runtime and mean energy-losses are heavily dependent on the number of substeps chosen. Also, there is a strong relationship concerning the number of actual collisions within a step-size versus the number of collisions allowed within the MFP of the LPT model. These relationships were further solidified when particles were transported through thicker slabs and energy-loss spectra within these thicker targets showed a decreasing spread of energy-losses with increasing substeps.

In order to find the optimal step-size, simulations were ran with different substeps and compared against the benchmark. It has already been discussed that energies around $1MeV$ show inaccurate results, while higher energies begin to agree. Simulations for $1MeV$ and $10MeV$ particles are presented to show where the LPT model did not work as well as where it did. Relevant data will also be compared against the benchmark to explain these results.

8.1 Energy-Loss Spectra

Here we make comparisons of energy-loss spectra obtained using the analog models that were developed in Chapter 3 against the LPT model described in Chapter 7. Figures 8.1 and 8.2 are comparisons of the benchmark using the Möller and Bhabha differential energy-loss cross sections against the Landau pseudo-differential cross section. These particles have energies of $1MeV$ and are incident on $9.6 \times 10^{-2}cm$ of water. From the figures, it is evident that the spectra do not match exactly. While the areas of most probable energy-loss are closely matched, after $0.5MeV$ the tails of the distributions differ significantly. This is caused by the impossibility of energy-losses associated with the λ_{cut} value inherent in the Landau distribution. The mismatch in the tail of energy-loss spectra is common in all figures, yet Figures 8.2-8.8 show that with increasing energy, the spectra under the area of most probable energy-loss is nearly exact.

As mentioned previously, run-times for the LPT model are very efficient. Table 8.1 shows the run-times and speed-up(over the benchmark) for the simulations in figures. In order to show the difference in choosing substeps, 1 substep is also included. The speed-up for a single substep is high. With increasing energy the speed-up becomes larger. Even with many substeps taken, the speed-up of the LPT model is at least 2 times better.

The spectra also shows that there is a more accurate computation for low Z materials. Water does not only match the spectra better around the most probable energy-loss but the energy-flux moments are better preserved when compared to gold. Table 8.2 shows an increasing convergence with increasing energy. The differences in the moments when compared to the benchmark are more accurate for low Z . Despite these results, there is still not an accurate spectra for energy-loss. The inability to capture the higher moments correlates to a less accurate representation

Chapter 8. Results and Comparisons to the Benchmark

of the analog problem. The next section will show how the LPT model compares with the benchmark in thicker slabs.

Run-times, Particles on Water and Gold				
Cross Section (substeps)	e^-		e^+	
	runtime(<i>min</i>)	speed-up	runtime(<i>min</i>)	speed-up
1MeV Particles on 2.5cm of Water				
Benchmark	116.76	1.00	263.17	1.00
LPT(1)	12.77	9.14	20.38	12.9
LPT(14)	74.75	1.56	87.61	3.00
10MeV Particles on 10cm of Water				
Benchmark	546.83	1.00	527.56	1.00
LPT(1)	3.29	166.21	5.51	95.75
LPT(20)	26.38	20.38	23.73	22.23
1MeV Particles on $8.52 \times 10^{-3}cm$ of Gold				
Benchmark	27.11	1.00	142.16	1.00
LPT(1)	11.77	2.30	48.30	2.94
LPT(14)	70.05	0.39	150.88	0.94
10MeV Particles on $7.5 \times 10^{-2}cm$ of Gold				
Benchmark	438.96	1.00	409.90	1.00
LPT(1)	6.38	68.80	19.91	20.59
LPT(20)	101.96	4.31	88.51	4.63

Table 8.1: Runtime Comparisons for Spectra Simulations of the LPT Model Against the Benchmark, for Electrons and Positrons.

Energy-flux Moments, Particles on Water and Gold						
Moments	e^-			e^+		
	Benchmark	LPT(substeps)	% Error	Benchmark	LPT(substeps)	% Error
1MeV Particles on 2.5cm of Water						
I_1	0.91675	0.91647(14)	0.0	0.92776	0.92670(14)	0.1
I_2	0.84716	0.84473	0.3	0.86560	0.86340	0.3
I_3	0.78713	0.78195	0.7	0.81015	0.80765	0.3
I_4	0.73423	0.72625	1.1	0.76000	0.75787	0.3
I_5	0.68691	0.67634	1.5	0.71428	0.71294	0.2
10MeV Particles on 10cm of Water						
I_1	8.9420	8.9430(20)	0.0	9.0168	9.0169(20)	0.0
I_2	80.570	80.657	0.1	81.906	81.981	0.0
I_3	729.77	731.32	0.2	746.69	749.28	0.3
I_4	6635.4	6656.0	0.3	6824.3	6873.5	0.7
1MeV Particles on $8.52 \times 10^{-3}cm$ of Gold						
I_1	0.91729	0.91685(14)	0.0	0.91687	0.90846(14)	0.9
I_2	0.84971	0.84197	0.1	0.84781	0.83202	1.9
I_3	0.79237	0.78028	1.5	0.78764	0.76654	2.7
I_4	0.74245	0.72626	2.2	0.73426	0.70950	3.4
I_5	0.69820	0.67831	2.8	0.68639	0.65916	4.0
10MeV Particles on $7.5 \times 10^{-2}cm$ of Gold						
I_1	9.1738	9.1619(20)	0.1	9.2422	9.2254(20)	0.2
I_2	84.730	84.576	0.2	85.986	85.742	0.3
I_3	786.27	784.46	0.2	802.60	800.65	0.2
I_4	7321.6	7300.7	0.3	7508.7	7501.2	0.1

Table 8.2: Energy-flux Moments Comparisons for Simulations of the LPT Model Against the Benchmark, for Electrons and Positrons on Gold and Water.

Chapter 8. Results and Comparisons to the Benchmark

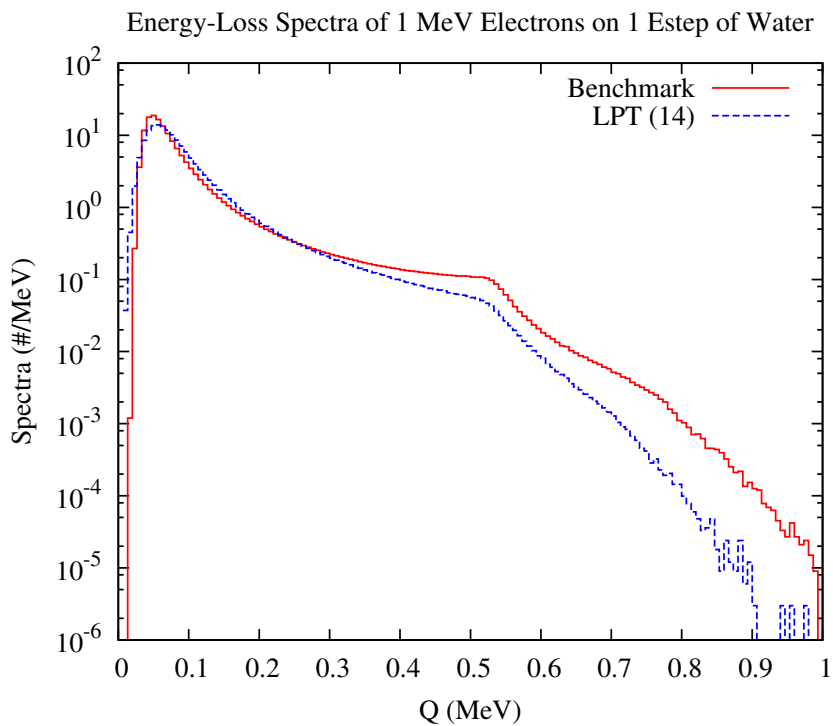


Figure 8.1: Energy-loss Spectra of 1 MeV Electrons on $9.6 \times 10^{-2} cm$ of Water

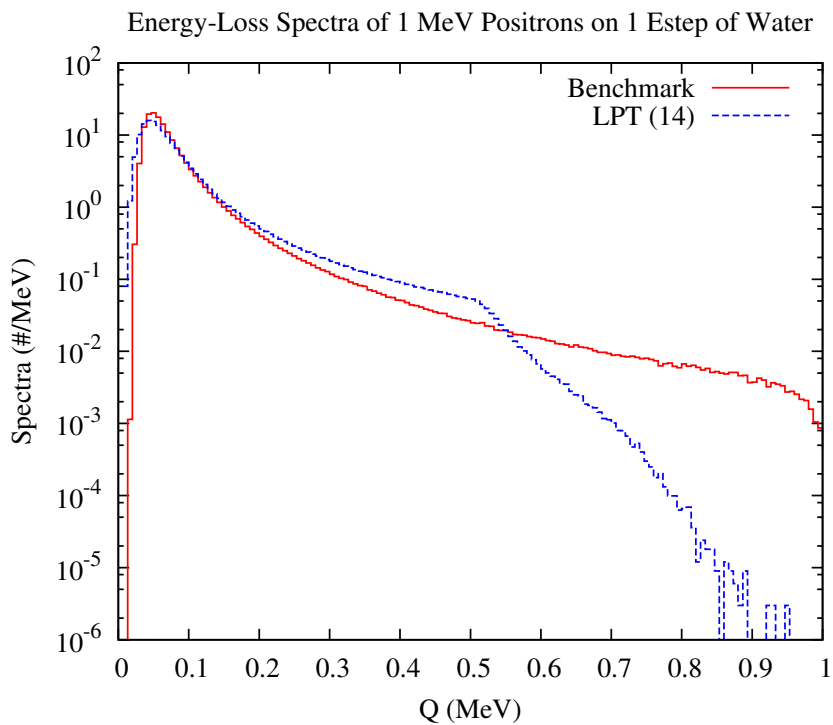


Figure 8.2: Energy-loss Spectra of 1 MeV Positrons on $9.6 \times 10^{-2} cm$ of Water

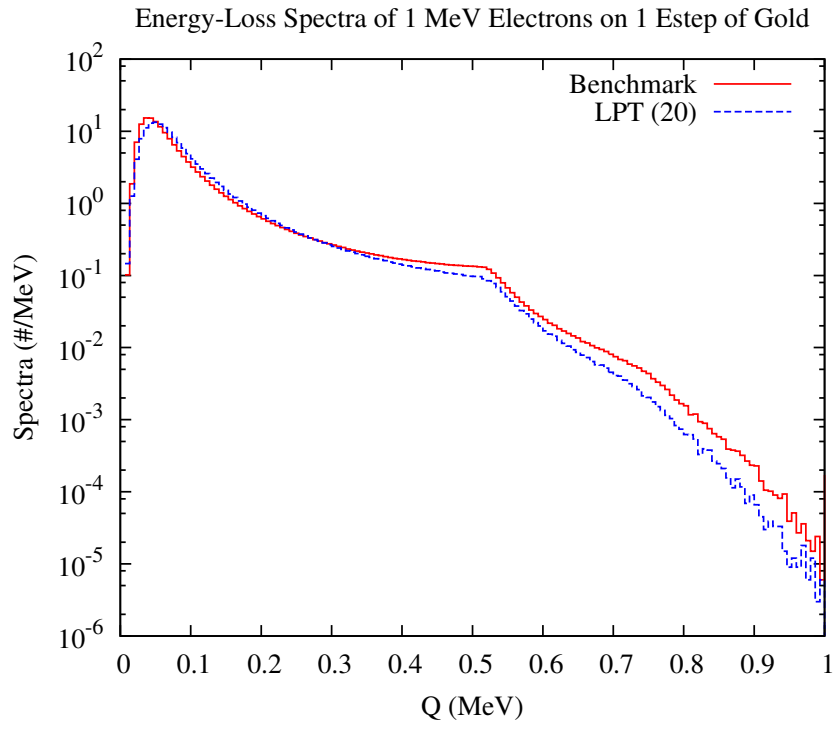


Figure 8.3: Energy-loss Spectra of 1 MeV Electrons on $8.52 \times 10^{-3} \text{ cm}$ of Gold

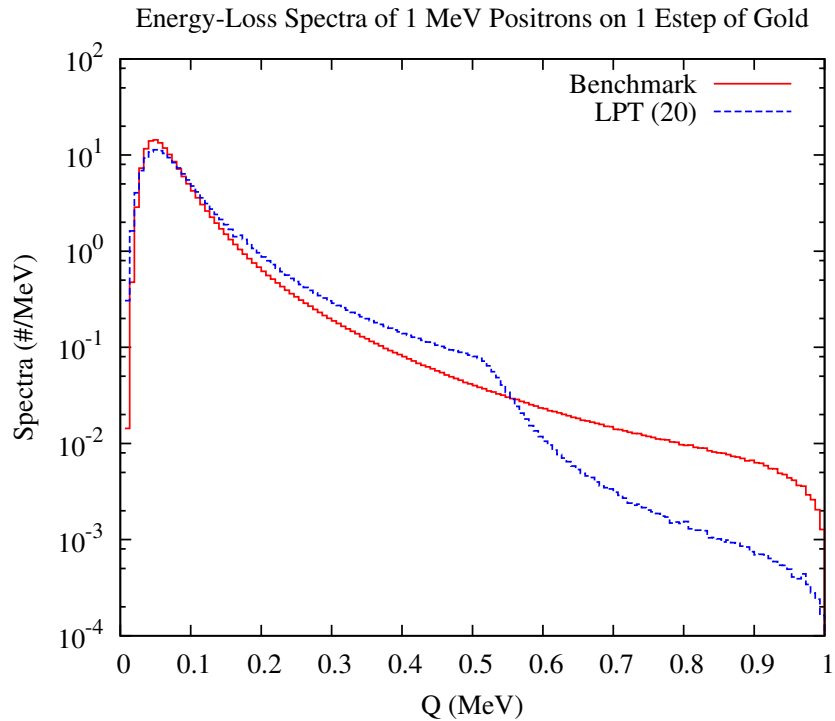


Figure 8.4: Energy-loss Spectra of 1 MeV Positrons on $8.52 \times 10^{-3} \text{ cm}$ of Gold

Chapter 8. Results and Comparisons to the Benchmark

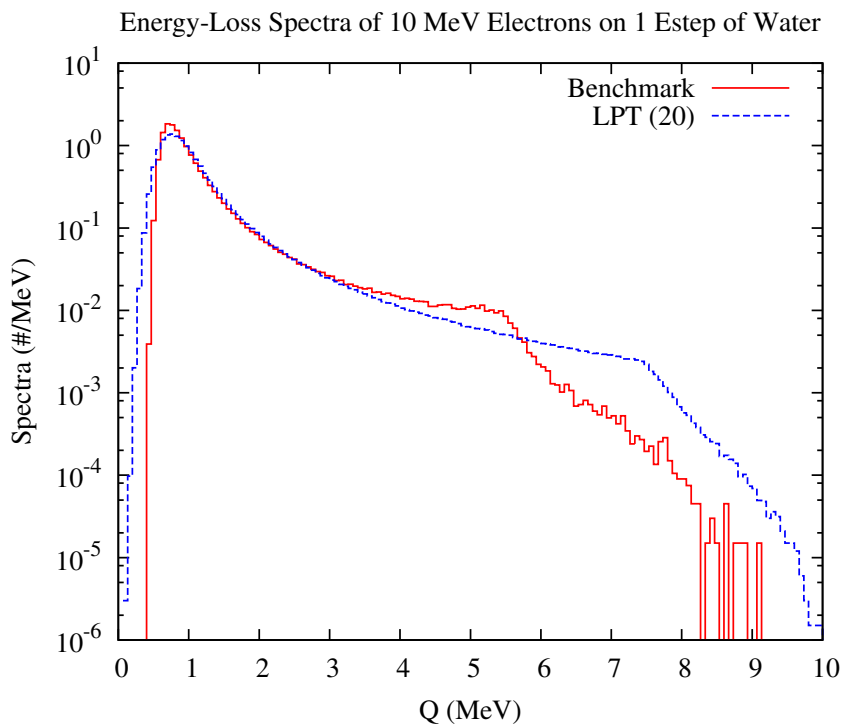


Figure 8.5: Energy-loss Spectra of 10 MeV Electrons on 1.31 cm of Water

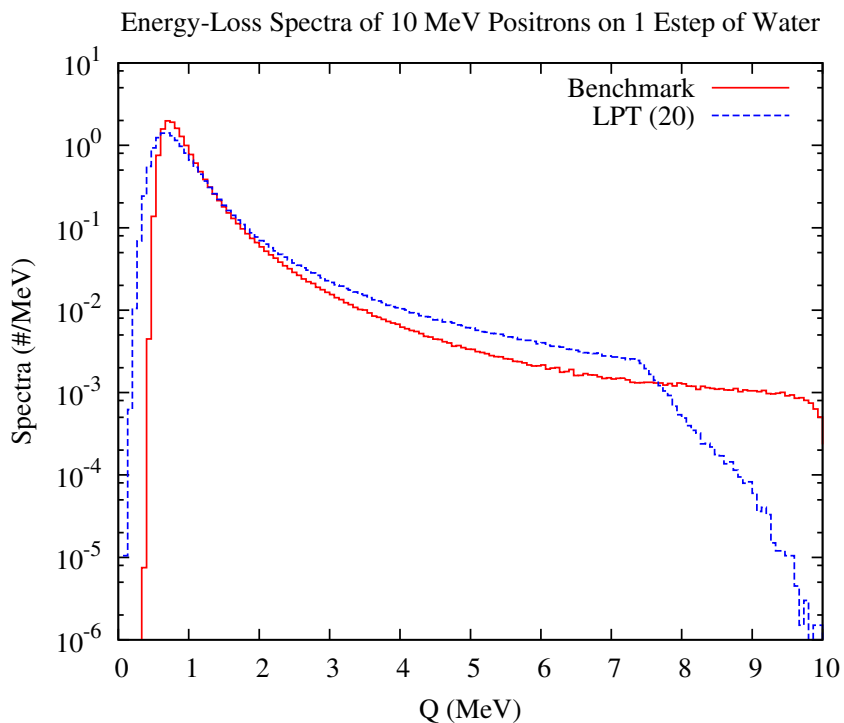


Figure 8.6: Energy-loss of 10 MeV Positrons on 1.31 cm of Water

Chapter 8. Results and Comparisons to the Benchmark

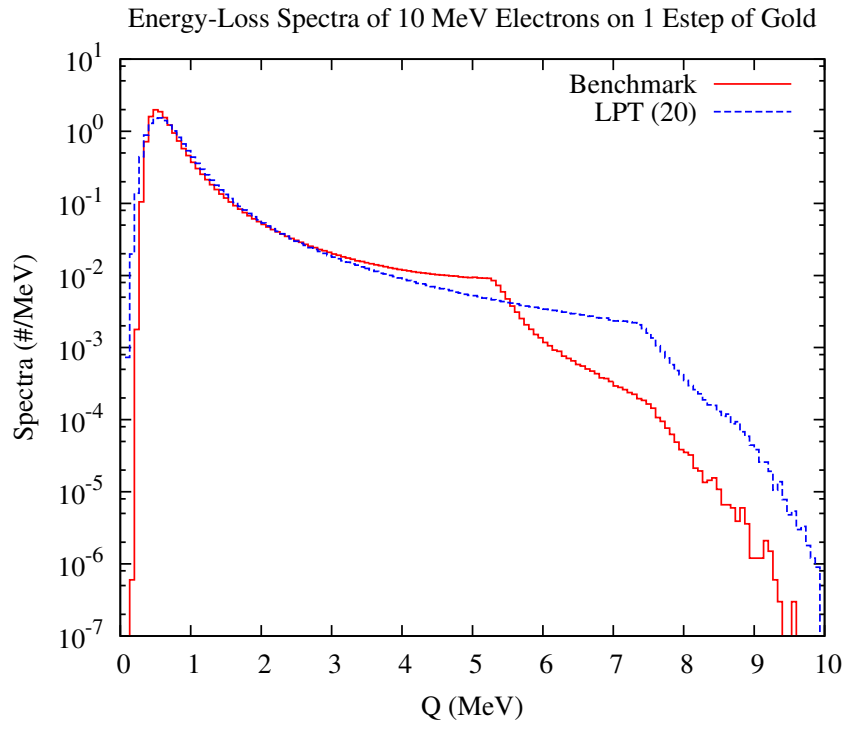


Figure 8.7: Energy-loss Spectra of 10 *MeV* Electrons on $7.5 \times 10^{-2}cm$ of Gold

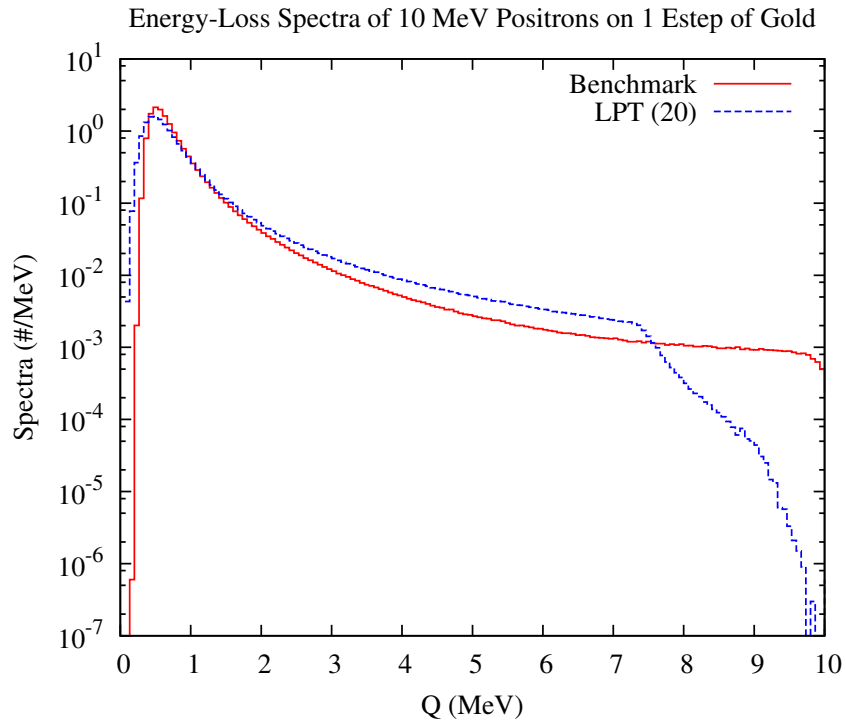


Figure 8.8: Energy-loss Spectra of 10 *MeV* Positrons on $7.5 \times 10^{-2}cm$ of Gold

8.2 Dose

As mentioned previously, there is a direct relationship between the MFP and the energy deposited. With long MFP's more energy is distributed throughout the material, while small MFP's increase the deposition and decrease the penetration of the particle. It has already been shown that $1MeV$ particles on gold did not produce accurate results in thin slabs, therefore it will not be included in this discussion.

Figures 8.9 and 8.10 model $1MeV$ electrons and positrons and are compared against the benchmark. These particles are incident on $2.5cm$ of water. Each of these simulations saw the best results at 1 substep. Although the energy-loss spectra and energy-flux moments showed a low count of accuracy, the distribution comes close to matching the benchmark. Positrons show a very large increase of energy deposited as the particle begins to slow down. Run-times for these simulations show a decrease in run-time by at least a factor of 2. The efficiency gained for dose deposition profiles can be seen in Table 8.3.

Figures 8.11 and 8.12 model the energy deposition and the energy-loss spectra for $10MeV$ electrons through $18cm$ of water. With only 5 substeps the dose profile is nearly exact. The speed-up of the LPT model is a factor of more than 6. Figure 8.12 gives an interesting insight. This figure shows that, although the energy-loss distribution does not match the energy-losses experienced by the benchmark, the dose profile still remains accurate. The figure does show, although the magnitudes do not match, that the LPT model matches the peak of the benchmark. If the MFP's were made smaller these peaks would begin to converge to the benchmark but 5 substeps provided a very accurate result with the best speed-up, seeking more substeps would not be worth the extra time.

Run-times, Particles on Water and Gold				
Cross Section (substeps)	e^-		e^+	
	runtime(<i>min</i>)	speed-up	runtime(<i>min</i>)	speed-up
1MeV Particles on 2.5cm of Water				
Benchmark	73.16	1.00	49.26	1.00
LPT(1)	11.24	6.5	29.97	2.28
10MeV Particles on 18cm of Water				
Benchmark	237.26	1.00	586.61	1.00
LPT(5)	34.91	6.80	34.28	17.11
10MeV Particles on 1.8cm of Gold				
Benchmark	72.93	1.00	141.51	1.00
LPT(5)	24.42	2.99	25.00	5.66

Table 8.3: Run-time Comparisons for Simulations of the LPT Model Against the Benchmark, for Electrons and Positrons on Water and Gold.

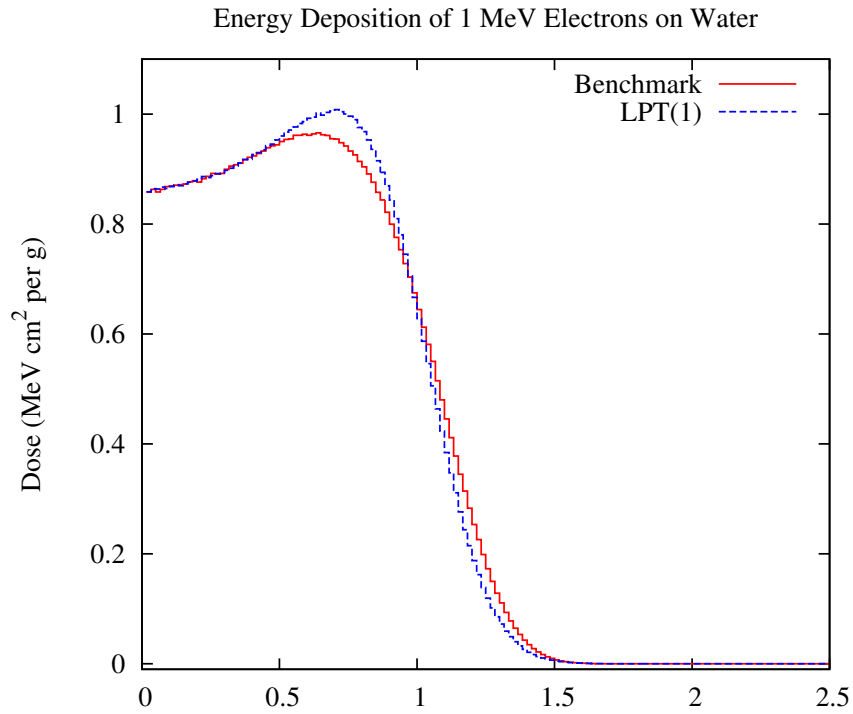


Figure 8.9: Energy Deposition of 1 MeV Electrons on 2.5 cm of Water

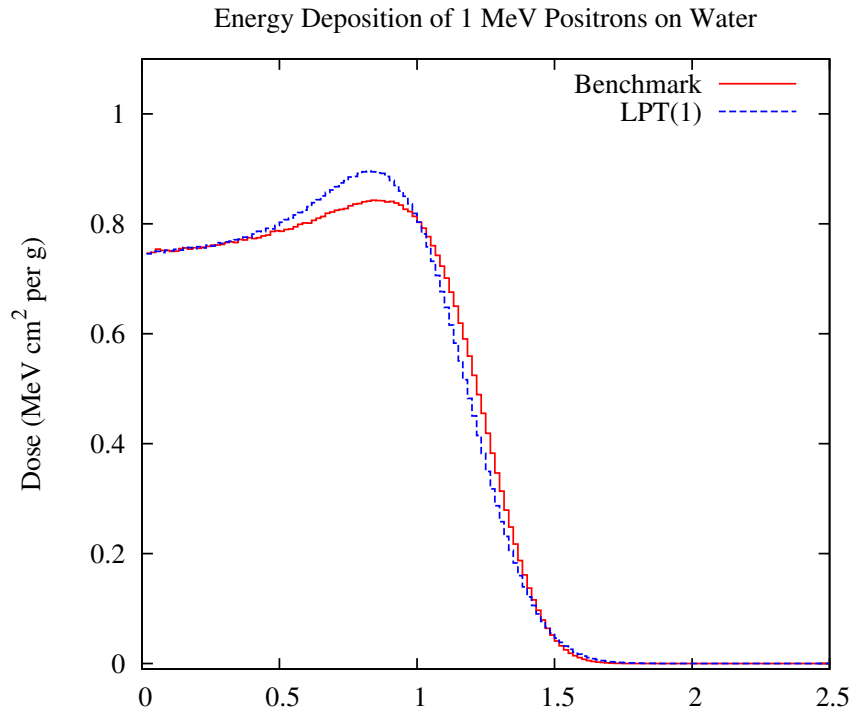


Figure 8.10: Energy Deposition of 1 MeV Positrons on 2.5 cm of Water

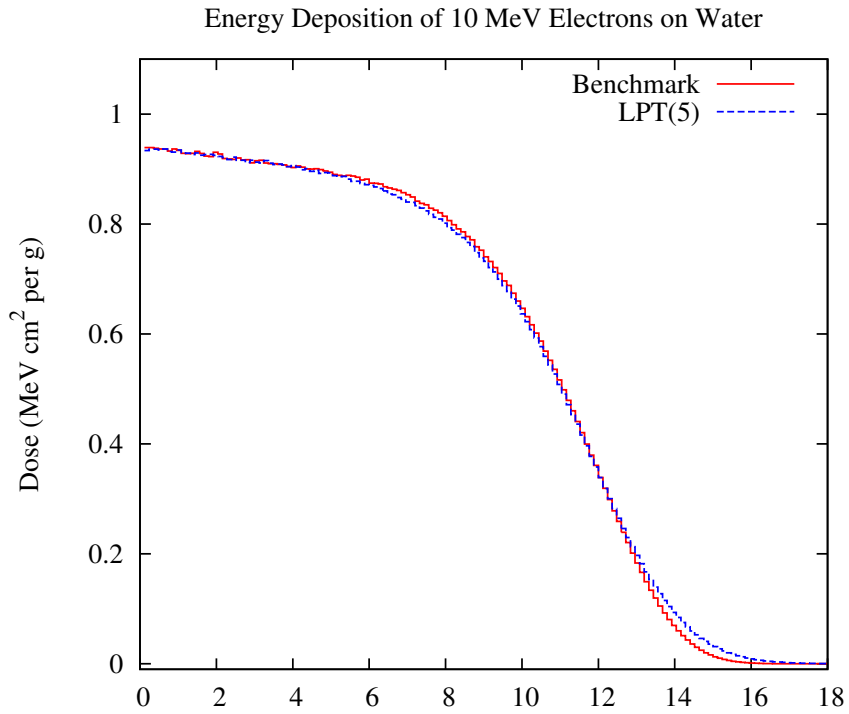


Figure 8.11: Energy Deposition of 10^6 10MeV Electrons on 18cm of Water

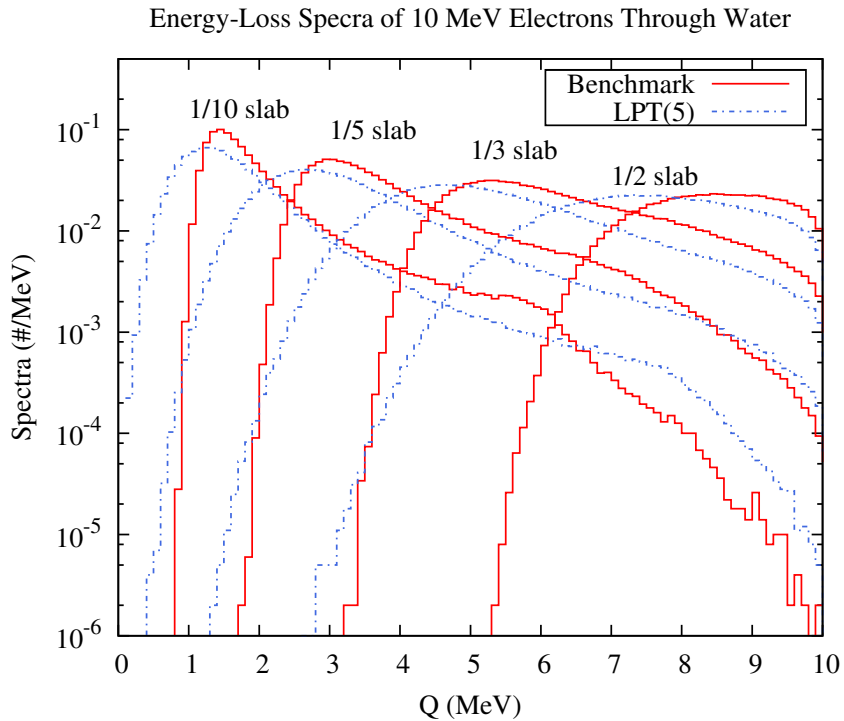


Figure 8.12: Energy-loss Spectra of 10^6 10MeV Electrons Through 18cm of Water

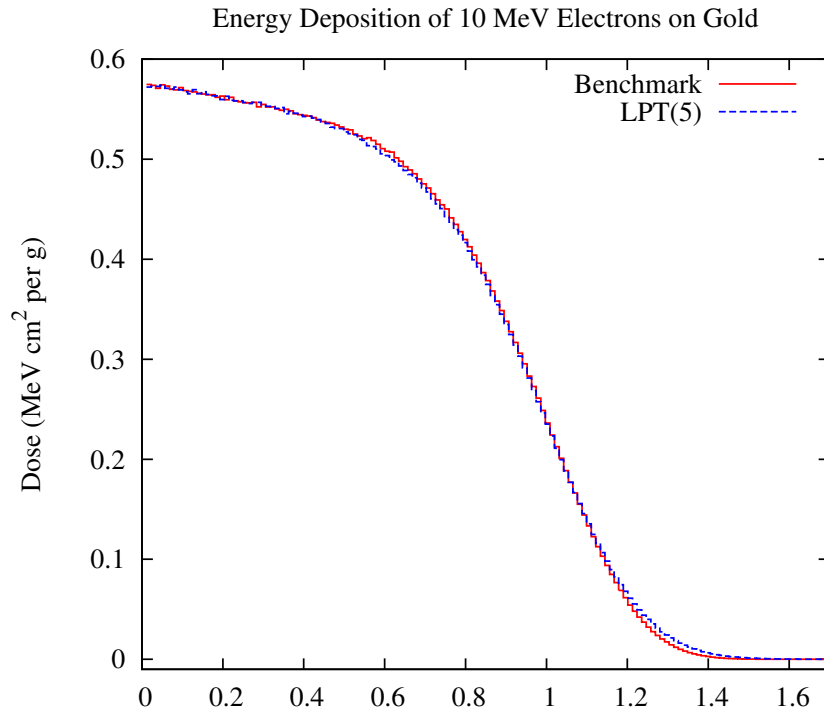


Figure 8.13: Energy Deposition of 10^6 10MeV Electrons on 1.7cm of Gold

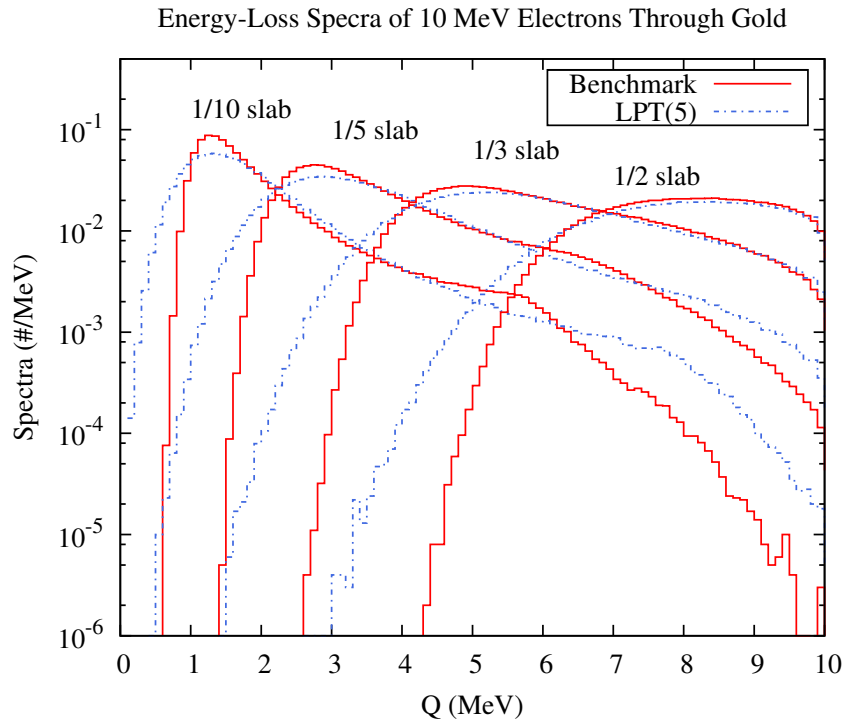


Figure 8.14: Energy-loss Spectra of 10^6 10MeV Electrons Through 1.7cm of Gold

Chapter 9

Conclusion

The primary objective of this thesis was to develop and demonstrate a computationally efficient moment-preserving single-event Monte Carlo method for electron and positron energy-loss straggling. We have explicitly shown through detailed simulation that electrons and positrons pose a unique problem for analog transport, in that, energy-loss distributions are highly peaked about low energy-losses, but have significant contributions from infrequent large energy-losses. We have shown that these large energy transfers lead to significant tails in the differential energy-loss cross sections which in turn result in long tails in energy-loss spectra and broadened dose profiles. Because of these deficiencies, analog energy-loss straggling simulations are highly inefficient. In this thesis we have introduced a Lewis-like moment-preserving theory which strongly suggested the accuracy of Landau's energy-loss distribution against the analog cross sections. As a result, we were able to define a pseudo-differential cross section which is more smooth than the analog and has a longer mean free path, resulting in a more efficient single-event transport of electrons and positrons. This pseudo-transport model was thoroughly tested and compared against the analog.

Chapter 9. Conclusion

We have generalized Lewis Theory to show that for thin layers, that it is possible to equate number of moments of the energy-loss preserved with the number of energy-flux moments preserved. This suggested, without formal proof, a relationship between the number of preserved energy-flux moments equating to the number of energy-loss moments preserved. Before this connection was made between the two types of moments, it was not possible to quantifiably measure how many moments the Landau distribution captured and to what accuracy. Landau has been customarily given credit for two moments, we have quantitatively shown this result in terms of energy-flux moments. It was shown that while the first two energy-loss and energy-flux moments were preserved, Landau captures higher order moments of the energy-flux. This suggested that Landau may also capture higher energy-loss moments. The ability to calculate the accuracy of Landau's distribution provided the development of a pseudo-transport model(LPT). We were able to redefine the differential cross section with a pseudo-differential cross section based on the Landau energy-loss distribution. The reason this is considered a pseudo-differential cross section is because there is no true physics involved in the redefined cross section, Landau is simply a distribution of variance about a mean value. The advantages gained by using the LPT model is allowing longer mean free paths, decreasing computational run-time and allowing for a true single-event transport process.

Thorough examination of the LPT model has indicated a strong dependence on the choice of step-size. For longer step-sizes where the greatest gain in run-time is possible, particles are allowed to move further and as a result increase the distribution of energy. Shorter step-sizes produce less distributed energy-losses and more peaked spectra but at the cost of run-time. In cases where the step-size is close to the analog mean free path, run-time becomes longer and the LPT model is no longer useful. Due to these conditions on step-size, there does exist a step-size that provides both an accurate result with the greatest gain in computational time. We have shown specific cases where these conditions have been met.

Chapter 9. Conclusion

Having successfully implemented the LPT model, we have shown that despite artifacts that arise in the energy-loss spectra for thin slabs, significant speed-ups accompanied by accuracy in relation to the analog solution has been obtained. It was shown for thin slabs that Landau inherently does not allow for energy-losses equating to energies above a specific cutoff value meant to preserve the average energy-loss within a given step. This cutoff value produces an artificial cutoff in the energy-loss spectra resulting in differences in the spectra for high energy-losses. As a result, it is impossible to match energy-loss spectra without manipulating the Landau distribution itself. Despite this artifact, comparison of thick material simulations have been shown to be as accurate as the analog solution. Energy deposition profiles have been matched while computational times have been significantly decreased.

The analog models that are used in this thesis have been rigorously studied and are well described by the Möller and Bhabha cross sections. Despite the fact that we only described a model for hard inelastic collisions with atomic electrons and positrons, the use of a moment-preserving pseudo-transport model demonstrates a high achievement in accuracy and efficiency. This moment-preserving model also demonstrates that the preservation of relatively low-order moments are essential to the approximation of analog distributions. In addition, the simplicity of this model stands in contrast to the complexity of the widely used condensed history model.

Further work can be done on optimizing the step-sizes in the LPT model. It was shown that specific step-sizes produced the best results, yet without some form of material or energy dependence. Since the step-size is energy dependent, it suggests that there must be a way to fine-tune the step-size in such a manner that the fastest and most accurate results will arise. Implementing either a conditional step-size or an adaptive step-size could guarantee the longest step-size with little accuracy lost in the simulation. More specifically, the step-sizes for an electron step is relative to the number of collisions for the particle to lose half of its initial energy. Changing

Chapter 9. Conclusion

this parameter as the particle moves through a material would be worth while since the number of collisions suffered through a material is not a linear process.

Along with step-size optimization, changing the LPT algorithm could contribute to further development. The LPT model currently samples an energy-loss relative to the mean free path, initial energy of the particle and the respective mean energy-loss within that path. It would be advantageous to examine the effects of sampling an energy-loss relative to the actual distance traveled by the particle. While it has been shown that step-sizes close to the analog mean free path produce inefficient results, this is only in terms of the distance traveled by the particle. Changing the distance in the energy-loss sampling could provide more accurate results.

A more thorough evaluation of the Landau distribution itself could also mitigate errors found in the LPT model. Sampling from the Landau distribution uses pre-computed arrays from the evaluation of $1MeV$ electrons on gold[4]. Recomputing these arrays for different energies or materials could remove the dependence on the cutoff value used in sampling from the distribution.

Lastly, implementing a hybrid method accompanying the LPT model could mitigate the artifacts that were produced by the Landau distribution in thin slabs. By coupling discrete energy-losses for highly probable interactions and using the LPT continuous model to deal with less probable interactions would potentially remove the large differences in the tail of energy-loss spectra.

References

- [1] M. J. Berger. *Monte Carlo Calculation of the Penetration and Diffusion of Fast Charged Particles*, volume 1. Academic Press, 1963.
- [2] H. Bhabha. The scattering of positrons by electrons with exchange on dirac's theory of the positron. *Proceedings of the Royal Society*, A154, 1936.
- [3] O. Blunck and S. Leisegang. Zum energieverlust schneller elektronen in d unnen schichten. *Z. Physik*, 128, 1950.
- [4] W. Boörsch-Supan. On the evalutaion of the function $\varphi(\lambda) = \frac{1}{2\pi i} \int_{-i\infty+\sigma}^{+i\infty+\sigma} e^{u \ln u + \lambda u} du$ for real values of λ . *Journal of Research of the National Bureau of Standards*, 65B(4), October-December 1961.
- [5] F. B. Brown. Fundamentals of monte carlo particle transport. Lecture Notes LA-UR-05-4983, Los Alamos National Laboratory.
- [6] F. B. Brown and Y. Nagaya. The mcnp5 random number generator. Transactions of the american nuclear society, Los Alamos National Laboratory, November 2002.
- [7] V. Chech and V. Ermilova. The ionization-loss distribution at very small absorber thickness. *Nucl.Instr.Meth.*, 136, 1976.
- [8] R. Evans. *The Atomic Nucleus*. Krieger Publishing Company, 1982.
- [9] B. C. Fanke and A. K. Prinja. Monte carlo electron dose calculations using discrete scattering angles and discrete energy losses. *Nuclear Science and Engineering*, 149, 2005.
- [10] S. Goudsmit and J. Saunderson. Multiple scattering of electrons. *Physical Review*, 57, 1940.

References

- [11] J. A. Halbleib, R. Kensek, T. Mehlhorn, G. Valdez, S. Seltzer, and M. Berger. Its version 3.0: The integrated tiger series of coupled electron/photon monte carlo transport codes, March 1992.
- [12] L. T. Harding. Monte carlo simulations of electron and positron energy-loss straggling. Master's thesis, University of New Mexico, 2006.
- [13] L. Landau. On the energy loss of fast particles by ionization. *Journal of Physics*, 8:201–205, 1944.
- [14] E. E. Lewis and W. F. M. Jr. *Computational Methods of Neutron Transport*. American Nuclear Society, 1993.
- [15] H. W. Lewis. Multiple scattering in an infinite medium. *Phys. Rev.*, 78:526–529, Jun 1950.
- [16] G. Moliere. Theorie der streuung schneller gelandener teilchen i: Einzelstreuung am abgeschirmten coulomb-feld. *Z. Naturforsch*, 2a, 1947.
- [17] C. Möller. Zur theorie des durchgang schneller elektronen durch materie. *Ann. Phys.*, 14, 1932.
- [18] J. Morel. On the validity of the extended transport correction for low energy electron transport. *Nuclear Science and Engineering*, 71, 1979.
- [19] A. Prinja, V. Klein, and H. Hughes. Moment-based effective transport equations for energy straggling. *Trans. Am. Nucl. Soc.*, 86, 2002.
- [20] A. K. Prinja. A theoretical result for moment-preserving approximations to the landau/vavilov straggling model. In *International Conference on Mathematics and Computational Methods & Reactor Physics*. American Nuclear Society, May 2009.
- [21] S. M. Seltzer. Electron-photon monte carlo calculations: The etran code. *Appl. Radiat. Isot.*, 42(10), 1991.
- [22] D. Sloan. *New Multigroup Monte Carlo Scattering Algorithm Suitable for Neutral and Charged-Particle Boltzmann and Fokker-Plank Calculations*. PhD thesis, University of New Mexico, 1983.
- [23] X.-. M. C. Team. Mcnp - a general purpose monte carlo n-particle transport code, version 5. Technical report, Los Alamos National Laboratory, 2003.
- [24] D. Tolar and E. Larsen. The moment condensed history algorithm for monte carlo electron transport. *American Nuclear Society International Meeting on Mathematical Methods for Nuclear Applications*, September 2001.

References

- [25] J. E. Turner. *Atoms, Radiation, and Radiation Protection*. Wiley-VCH, 3rd edition, 2007.